Energy scale non-linearity and event reconstruction for the Neutrino Mass Ordering measurement of the JUNO experiment

Von der Fakultät für Mathematik, Informatik und Naturwissenschaften der RWTH Aachen University zur Erlangung des akademischen Grades eines Doktors der Naturwissenschaften genehmigte Dissertation

vorgelegt von

Philipp René Kampmann

aus Oberhausen

Berichter: Univ.-Prof. Dr. Livia Ludhova
Univ.-Prof. Dr. rer. nat. Christopher Wiebusch

Tag der mündlichen Prüfung: 18.11.2020

Abstract

The JUNO experiment is a next-generation neutrino experiment under construction in vicinity of the Pearl River Delta in Southern China. It is expected to start data-taking in 2022 and aims to address the determination of the Neutrino Mass Ordering with 3-4 σ sensitivity in about 6 years as its main goal. For that, it will measure the oscillated energy spectrum of electron anti-neutrinos from two nuclear power plants at a baseline of about 53 km with a required energy resolution of 3% at 1 MeV and a sub-percent uncertainty on the energy scale. In order to reach these requirements, the JUNO detector consists of a large 20 kton liquid scintillator detector, which is instrumented with a dense PMT array consisting of about 18,000 large 20"-PMT's and 25,000 small 3"-PMT's. Besides this main goal it aims to address a large variety of important topics in neutrino and astroparticle physics. The first part of this thesis gives an overview over the current status of neutrino physics and shows why the determination of the Neutrino Mass Ordering is a key to explore a large area of physics topics. Moreover, it gives an overview of the JUNO experiment: the detector design and its calibration, the simulation framework, and the various physics goals of the JUNO experiment.

Besides the detector design, a meticulous data analysis is needed to ensure, that the JUNO experiment can meet the requirements on the precision and accuracy on the reconstructed energy. Such analysis methods are presented in the second part of this thesis. Here, a model is presented, which can be used to describe the non-linear light response of positrons in the liquid scintillator. Based on the non-linearity model of electrons, an algorithm is introduced to calculate the more complex non-linearity model of gammas and combine both eventually to the non-linearity model of positrons. As the amount of detected light for a constant energy varies with the position of the energy deposition in the detector, the energy resolution of JUNO is impacted by the uncertainty of the reconstructed light emission vertex. The vertex reconstruction finds the light emission vertex by minimizing a likelihood function, which contains the information on the times and charges of the PMT hits. It is shown, that the uncertainty on the reconstructed vertex is especially small at the outer parts of the volume, where the effect on the energy resolution is the largest. Additionally to the improvement of the energy resolution, it is shown how the vertex reconstruction can be used to reconstruct the direction of an electron anti-neutrino flux from a point-source. Another important effect, which leads to biases on the reconstructed energy on JUNO is the pile-up of signal events with ^{14}C decays. The organic scintillator contains large amounts of natural, radioactive ^{14}C. These ^{14}C decays are able to timely coincide with measured signal events to cause a smearing of the measured energy spectrum. To reduce the impact of these ^{14}C decays, two analysis methods are presented. A clusterization algorithm identifies different energy depositions in the PMT hit time distribution. This algorithm is optimized on the sensitivity of JUNO to determine the Neutrino Mass Ordering. For event coincidences, which can not be separated in time, the vertex reconstruction is used to perform a likelihood test to identify these.

Zusammenfassung

Das JUNO-Experiment ist ein Neutrino-Experiment der nächsten Generation, das in der Nähe des Perlflussdeltas in Südchina gebaut wird. Es wird erwartet, dass die Datenerfassung, die hauptsächlich darauf abzielt, die Neutrinomassenanordnung mit 3-4 σ Sensitivität in etwa 6 Jahren Datennahme zu bestimmen, in 2022 beginnt. Dazu wird es das oszillierte Energiespektrum der Elektron-Antineutrinos aus zwei Kernkraftwerken in einer Distanz von etwa 53 km mit einer nötigen Energieauflösung von 3% bei 1 MeV und einer subprozentigen Unsicherheit auf die Energieskala messen. Um diese Anforderungen zu erreichen, besteht der JUNO-Detektor aus einem großen 20 kt Flüssigszintillator-Detektor, der mit einem dichten PMT-Array bestehend aus etwa 18.000 großen 20"-PMT's und 25.000 kleinen 3"-PMT's instrumentiert ist. Neben dem Hauptziel plant JUNO eine große Vielfalt von wichtigen Themen der Neutrino- und Astroteilchenphysik zu behandeln. Der erste Teil dieser Arbeit gibt einen Überblick über den aktuellen Stand der Neutrinophysik und zeigt, warum die Bestimmung der Neutrinomassenanordnung ist ein Schlüssel zur Erforschung eines großen Bereichs physikalischer Themen ist. Darüber hinaus gibt sie einen Überblick über das JUNO-Experiment: die Konstruktion des Detektors und seine Kalibrierung, das Simulationsframework und die verschiedenen physikalischen Ziele des JUNO-Experiments.

Neben dem Detektordesign ist eine akribische Datenanalyse notwendig, um sicherzustellen, dass das JUNO-Experiment die Anforderungen an die Präzision und Genauigkeit der rekonstruierten Energie erreichen kann. Solche Analysemethoden werden im zweiten Teil dieser Doktorarbeit vorgestellt. Hier wird ein Modell vorgestellt, das zur Beschreibung der nichtlinearen Lichtproduktion von Positronen im Flüssigszintillator benutzt werden kann. Basierend auf dem Nichtlinearitätsmodell der Elektronen wird ein Algorithmus eingeführt, der das komplexere Nichtlinearitätsmodell von Gammas berechnet und beide kombiniert, um schließlich das Nichtlinearitätsmodell von Positronen zu erhalten. Die Energieaufösung von JUNO wird durch die Unsicherheit auf die rekonstruierten Lichtemissionsvertizes beeinflusst. Da sich die Menge des detektierten Lichts sich für eine konstante Energie mit der Position der Lichtemission im Detektor ändert, wird die Energieauflösung von JUNO direkt durch die Unsicherheit auf die rekonstruierten Lichtemissionsvertizes beeinflusst Die Vertexrekonstruktion findet den Lichtemissionsvertex durch Minimierung einer Likelihood-Funktion, die die Informationen über die Zeiten und Ladungen der PMT-Treffer enthält. Es wird gezeigt, dass die Unsicherheit auf dem rekonstruierten Vertex ist an den äußeren Teilen de Volumens besonders gering, wo die Auswirkung auf die Energieauflösung am größten ist. Zusštzlich zur Verbesserung der Energieauflösung wird gezeigt, wie die Vertexrekonstruktion genutzt werden kann die Richtung eines Elektron-Antineutrinoflusses einer Punktquelle rekonstruiert werden kann. Ein weiterer wichtiger Effekt, der dazu führt zu Verzerrungen auf die rekonstruierte Energie auf JUNO ist die Anhäufung von Signalereignissen mit ^{14}C-Zerfällen. Der organische Szintillator enthält große Mengen an natürlichem, radioaktiven ^{14}C. Diese ^{14}C-Zerfälle sind in der Lage, mit gemessenen Signalereignissen zeitlich zusammenzufallen und eine Verschmierung der gemessenen Energie zu verursachen. Um den Einfluss dieser ^{14}C-Zerfälle zu reduzieren, werden zwei Analysemethoden vorgestellt. Ein Clustering-Algorithmus identifiziert unterschiedliche Energiedepositionen in der Zeitverteilung der PMT-Treffer. Dieser Algorithmus ist optimiert auf die Sensitivität von JUNO zur Bestimmung der Neutrinomassenanordnung. Für Ereigniskoinzidenzen, die sich zeitlich nicht trennen lassen, wird die Vertex-Rekonstruktion dazu verwendet, einen Likelihood-Test durchzuführen, um diese zu identifizieren.

Contents

Chapter 1

Introduction

Part I of this thesis gives an overview on the current status of neutrino physics and describes the JUNO experiment, which aims to measure the Neutrino Mass Ordering, which is in the focus of this thesis. Neutrinos were postulated in 1930 to explain the measured continuous energy spectrum and the conservation of angular momentum of β decays [1]. The first measurement of the neutrino was finally performed many years after their postulation in 1956 by the Cowan-Reines Neutrino Experiment [2], which proved the neutrino theory and that neutrinos are detectable. In the 1960s, the Homestake experiment [3] measured a puzzling deficit in the flux of neutrinos emitted from the Sun to the predictions from the *Standard Solar Model* [4], known then as the *Solar Neutrino Problem* [5]. This discrepancy was explained with possible transitions of the three known weak interaction flavors of the neutrinos into each other, the *neutrino oscillations*, which were named after the usually observable oscillatory structure of these transitions in the energy over baseline ratio [6]. The flavor transitions of neutrinos were confirmed by the Super-Kamiokande experiment with atmospheric neutrinos and the Sudbury Neutrino Observatory (SNO) with the measurement of neutrinos from the Sun [7–10]. The theory of neutrino oscillations requires the neutrinos to carry mass, contrary to their postulation and their description in the *Standard Model of Particle Physics*. Although, after the confirmation of neutrino oscillations many experiments were performed to measure neutrino oscillations with high precision, there are still many open questions in the field of neutrino physics and neutrino oscillations. Chapter 2 reviews the current state of neutrino research. While Sec. 2.1 describes the neutrino oscillation formalism, Sec. 2.2 gives an overview over the large variety of neutrino sources, and Sec. 2.3 introduces the current status and open question in neutrino physics.

One open question is the *Neutrino Mass Ordering*, the question which of the three neutrino masses is the heaviest. The determination of the Neutrino Mass Ordering plays a key role in neutrino physics as it aids in the search for the nature of the neutrino masses and possible leptonic CP-violations, as well as measurements related to astroparticle physics and cosmology. The JUNO experiment aims to address the determination of the Neutrino Mass Ordering with about 3-4 σ significance in 6 years as its main goal with the measurement of vacuum neutrino oscillations [11]. This approach by JUNO is currently unique and complementary to the determination of the Neutrino Mass Ordering with the measurement of the matter effect on neutrino oscillations, planned by many other experiments using either beam neutrinos [12, 13] or atmospheric neutrinos [14–17]. To reach that goal, the JUNO experiment uses a 20 kton

liquid scintillator detector to measure the electron anti-neutrino flux from two nuclear power plants in a distance of about 53 km. This liquid scintillation volume is observed by about 18,000 large 20"-PMT's and about 25,000 small 3"-PMT's to reach an unprecedented energy resolution of about 3% at 1 MeV visible energy. Besides an excellent energy resolution, a high accuracy below 1% of the energy scale is needed to resolve the Neutrino Mass Ordering, as it is measured through the measurement of a fast oscillatory structure in the spectrum of reactor electron anti-neutrinos. The JUNO experiment is currently under construction in vicinity of the Pearl River Delta in South China and expected to start data-taking in 2022. Chapter 3 reviews the JUNO experiment: the detector systems, the detection of particles and its calibration, as well as the simulation software. Beyond the determination of the Neutrino Mass Ordering, the JUNO experiment has a broad physics programme, which addresses various topics in neutrino physics, as well as astroparticle physics, and particle physics, described in Sec. 3.6.

The determination of the Neutrino Mass Ordering, which drives the detector design of JUNO, has strict requirements on the accuracy and precision of the reconstruction of the reactor electron anti-neutrino energies. Part II of this thesis introduces analysis methods to improve this accuracy and precision, developed as part of this thesis. As the light production of the liquid scintillator is not fully linear to the amount of deposited ionization energy and dependent on the particle type, a model to describe the energy non-linearity for electrons, gammas, and positrons is introduced in Chapter 4. Based on a simple non-linearity model of electrons, this chapter provides the conversion to the more complex non-linearity models of gammas and positrons. Here, a fast and simple algorithm is developed to calculate the secondary electron spectrum of an initial gamma. It is used to eventually obtain the non-linearity model of positrons, which is needed for the appropriate description of the positron spectrum, which stems from reactions of reactor electron anti-neutrinos in the JUNO detector.

The energy resolution of JUNO is mainly defined by the collected photon statistics. Besides that, the energy resolution is also influenced by the dark count noise of the PMT's and the vertex reconstruction. Due to the detector properties of JUNO, for a constant energy, the amount of detected light depends on the light emission point. The vertex reconstruction is needed to correct the reconstructed energy for this non-uniform light detection. A high uncertainty on the reconstructed vertex directly translates to a high uncertainty of the reconstructed energy. Chapter 5 introduces a vertex reconstruction algorithm, which uses the times and charges of the PMT hits to find a best estimate for the light emission point under the use of a likelihood function. This vertex reconstruction shows expecially good results in the outer parts of the detector, where a high gradient in the vertex dependence of the light response causes a large uncertainty on the energy. The effect and improvement of this vertex reconstruction on the energy reconstruction is evaluated as well as the possibility to reconstruct the direction of an electron anti-neutrino flux, which depends largely on the vertex reconstruction.

Another effect, which introduces a bias on the reconstructed energy is the pile-up of signal events with ^{14}C decays, which occur naturally in large amounts in the organic liquid scintillator. Chapter 6 introduces methods to identify pile-up events to reduce the impact of such ^{14}C decays on the measured energy spectrum. A simple way to identify a second energy deposition is introduced via the clusterization algorithm, which identifies different energy deposition due to the accumulation of PMT hits in the PMT hit time distribution. Besides the identification of ^{14}C pile-up events, the clusterization algorithm provides a general tool to separate different

energy depositions in the same event and allows other reconstruction algorithms to reconstruct each energy deposition separately. For this purpose, this algorithm is implemented in the analysis software of the JUNO experiment [18, 19]. The optimization of the clusterization algorithm on the sensitivity of JUNO to determine the Neutrino Mass Ordering using the GNA tool [20, 21] is shown. As the clusterization algorithm is not able to separate different energy depositions, which overlap in the PMT hit time distribution, the likelihood value of the vertex reconstruction from Chapter 5 is used to tag overlapping pile-up events.

Part I

Neutrino Physics in JUNO

Chapter 2

Neutrino Physics

Neutrinos are massive, spin-$\frac{1}{2}$, electrically neutral, leptons with very small mass [22] . The *Standard Model of Particle Physics* (SM) contains 3 different generations of neutrinos. These are named after their charged lepton counterparts as electron-neutrino (ν_e), muon-neutrino (ν_μ), and tau-neutrino (ν_τ) as well as the electron anti-neutrino ($\bar{\nu}_e$), the muon anti-neutrino ($\bar{\nu}_\mu$), and the tau anti-neutrino ($\bar{\nu}_\tau$). Different to the other particles of the SM, neutrinos take only part in interactions of the *weak force*. Compared to the *electromagnetic force* and the *strong force*, the weak force yields very small interaction cross sections. These let neutrino beams surpass long distances (e.g. through Earth [23]) with only small attenuation. While these small cross sections make neutrinos special in probing the inner structure of the Sun [24] or Earth [25], they also lead to difficulties in their detection.

The existence of neutrinos was first postulated by W. Pauli in 1930, who used the idea of the neutrino to rescue the energy and angular momentum conservation in β-decays [1]. Due to the challenges in detecting the neutrino, the first measurement of the neutrino[1] was published in 1956 by the Cowan-Reines Neutrino Experiment [2]. The Homestake experiment later published puzzling results [3]. It measured a large discrepancy to the predicted solar neutrino flux from the *Standard Solar Model* [4] and the SM. This discrepancy is known as the *Solar Neutrino Problem* [5]. It was solved in 2001 by the publication of the Sudbury Neutrino Observatory (SNO), which explained the deficit of ^{8}B-neutrinos from the Sun via neutrino flavor changes [7, 8]. These results were published after the Super-Kamiokande experiment saw neutrino flavor changes in a wide energy range of atmospheric neutrinos [9]. These neutrino flavor changes were explained by the idea of so-called *neutrino oscillations*, which was first formulated by B. Pontecorvo in 1957 [6] and prove that neutrinos carry mass. The discovery of neutrino oscillations was awarded with the Nobel Prize in 2015 [10].

2.1 Neutrino Oscillations

While for the charged leptons the mass eigenstates are also flavor eigenstates of the weak interaction, the neutrino flavor eigenstates are a superposition of the neutrino mass eigenstates. The flavor eigenstates can be defined by the leptonic W-decay. A neutrino of a certain flavor

[1] the electron anti-neutrino ($\bar{\nu}_e$)

is therefore created in a W-decay alongside an anti-lepton of the same flavor. Therefore, the β^--decay produces, besides the electron, an anti-neutrino with electron-flavor. Following this definition, the neutrino flavor states are orthogonal. If the neutrino flavor would be measured immediately after its creation via the creation of a charged lepton, it is assumed that this charged lepton must be of the same flavor as the initial neutrino. However, as mentioned before, it was measured that the flavor can differ from its initial state after traveling over a distance. As the probability of these flavor changes has an oscillatory character, it is commonly referred to as *neutrino oscillations*.

The flavor changes and their oscillatory character follow directly from the initial statement, that the neutrino mass eigenstates do not coincide with the neutrino lepton flavor states, but are a superposition:

$$|\nu_\alpha\rangle = \sum_i U^*_{\alpha i} |\nu_i\rangle. \tag{2.1}$$

Here the flavor state $|\nu_\alpha\rangle$ is expressed as a superposition of the mass eigenstates $|\nu_i\rangle$. In the following, Greek subscripts will be used for flavor eigenstates, while Latin subscripts are used to denote mass eigenstates. The coefficients $U^*_{\alpha i}$ are the complex conjugated elements of the leptonic mixing matrix. This matrix is usually called the *Pontecorvo-Maki-Nakagawa-Sakata matrix* (PMNS matrix) [22]. It is analogous to the *Cabibbo-Kobayashi-Maskawa matrix*, which is used to describe quark mixing. The leptonic mixing has found to be much stronger than the mixing of the quark flavors. As the flavor eigenstates are orthogonal, the mass eigenstates are also orthogonal. This means that the full PMNS matrix must be an unitary matrix, although the full PMNS matrix may not be a 3×3-matrix (see Sec. 2.3.6). The 3×3 sub-matrix of the known 3 generations is then not required to be unitary, if there are more neutrino mass and flavor states. In the 3×3 form, the PMNS matrix is given by [22]:

$$U_{PMNS} = \begin{pmatrix} U_{e1} & U_{e2} & U_{e3} \\ U_{\mu 1} & U_{\mu 2} & U_{\mu 3} \\ U_{\tau 1} & U_{\tau 2} & U_{\tau 3} \end{pmatrix} \tag{2.2}$$

$$= \begin{pmatrix} 1 & 0 & 0 \\ 0 & c_{23} & s_{23} \\ 0 & -s_{23} & c_{23} \end{pmatrix} \times \begin{pmatrix} c_{13} & 0 & s_{13}e^{-i\delta} \\ 0 & 1 & 0 \\ -s_{13}e^{i\delta} & 0 & c_{13} \end{pmatrix} \times \begin{pmatrix} c_{12} & s_{12} & 0 \\ -s_{12} & c_{12} & 0 \\ 0 & 0 & 1 \end{pmatrix} \times \begin{pmatrix} e^{i\alpha_1/2} & 0 & 0 \\ 0 & e^{i\alpha_2/2} & 0 \\ 0 & 0 & 1 \end{pmatrix}. \tag{2.3}$$

For readability $s_{ij} \equiv \sin(\theta_{ij})$ and $c_{ij} \equiv \cos(\theta_{ij})$ are used. Besides the complex phases, the PMNS matrix can be seen as a combination of three real rotational matrices with the rotation angles θ_{12}, θ_{13}, and θ_{23}. The complex phases δ, α_1 and α_2 describe the possible CP-violating phases in the PMNS matrix, while the phases α_1 and α_2 are called the *Majorana phases* and only occur if the neutrinos are Majorana fermions. These Majorana phases do not impact the probability of measuring a neutrino flavor change and can therefore be ignored in this context.

To calculate the probability of measuring a neutrino which was created as flavor α and energy E as flavor state β at the distance L the amplitude

$$P_{\alpha\to\beta}(L) = |\langle \nu_\beta(L) | \nu_\alpha(0) \rangle|^2 \tag{2.4}$$

needs to be calculated. As the flavor eigenstates are no eigenstates of the Hamilton operator, the propagation should be formulated in mass eigenstates. Using the assumption, that

the neutrino travels as a plane wave through vacuum, the solution of the time dependent Schrödinger Equation can be used:

$$e^{i(p_j L - Et)} \approx e^{i\left(\left(E - \frac{m_j^2}{2E}\right)L - Et\right)} = e^{iE(L-t)} \cdot e^{im_j^2 \frac{L}{2E}}, \tag{2.5}$$

with t being the time and E the energy of the neutrino, using $c = \hbar = 1$. Here, the momentum was Taylor-expanded in linear order in m/E as the neutrino masses were measured to be very small compared to their typical energies in neutrino experiments. This leads to

$$|\nu_\alpha(L)\rangle \approx \sum_j U_{\alpha j}^* |\nu_j\rangle e^{im_j^2 \frac{L}{2E}}. \tag{2.6}$$

The global phase $e^{iE(L-t)}$ was omitted here, as a propagation with the speed of light was assumed. This can be inserted into Eq. 2.4 giving the probability for flavor changes:

$$P_{\alpha\to\beta}(L) = |\sum_j U_{\alpha j}^* U_{\beta j}^* e^{-i\frac{m_j^2}{2E}L}|^2. \tag{2.7}$$

For $\alpha = \beta$, Eq. 2.7 is called usually *survival probability*, which is measured in *disappearance* experiments. Accordingly, for $\alpha \neq \beta$, Eq. 2.7 is usually called *appearance probability*. However, it should be noted that the total neutrino flux is not changed due to neutrino oscillations, but the effective flavor composition.

After multiplying out this equation, expressions in the form of

$$e^{i(m_k^2 - m_j^2)L/2E} \tag{2.8}$$

occur. These show the periodic behavior with L/E and are the reason behind the name *neutrino oscillations*. Moreover, the oscillation frequencies of these terms are proportional to $\Delta m_{kj}^2 \equiv m_k^2 - m_j^2$. It is directly visible from these so-called *mass splittings*, that neutrino oscillations can only occur if neutrinos have masses. The mixing angles of the PMNS matrix can be seen as amplitudes of the oscillations.

A comprehensive reference for further reading can be found in [26].

Due to the large difference of the mass splittings (see Sec. 2.3), the three-flavor model oscillations can often be approximated by the two-flavor model. In the two-flavor model, neutrino oscillation probabilities can be described with one mixing angle and one mass splitting:

$$P(\nu_\alpha \to \nu_\beta, \alpha = \beta) = 1 - \sin^2 2\theta \sin^2 \frac{\Delta m^2 L}{4E} \text{ and} \tag{2.9}$$

$$P(\nu_\alpha \to \nu_\beta, \alpha \neq \beta) = \sin^2 2\theta \sin^2 \frac{\Delta m^2 L}{4E}. \tag{2.10}$$

This thesis focuses on the measurement of initial electron anti-neutrinos at energies of a few MeV. As neutrinos of these energies can not produce muons or tauons in interactions in the detector, only the probability of electron anti-neutrino disappearance is relevant. In the three-flavor model, this probability can be written as:

$$\begin{aligned} P(\bar{\nu}_e \to \bar{\nu}_e) = 1 &- \sin^2 2\theta_{12} \cos^4 \theta_{13} \sin^2 \frac{\Delta m_{21}^2 L}{4E} \\ &- \sin^2 2\theta_{13} \left[\cos^2 \theta_{12} \sin^2 \frac{\Delta m_{31}^2 L}{4E} + \sin^2 \theta_{12} \frac{\Delta m_{32}^2 L}{4E}\right]. \end{aligned} \tag{2.11}$$

2.1.1 Decoherence of mass eigenstates

When using the time-dependent solution of the Schrödinger equation for the propagation of the mass eigenstates, the assumption of a plane wave was used. A plane wave has an infinitely precise momentum, leading to an infinite intrinsic uncertainty on the location. There are approaches to overcome this assumption, mostly favoring the *wave packet* approach [27, 28]. It describes the neutrino mass eigenstates as wave packets with a finite widths and due to the different neutrino masses also with different propagation velocities. In conclusion, the neutrino mass eigenstates loose their coherence at high values of L/E, otherwise the plane wave assumption is valid. If the coherence is lost, the oscillatory behavior, which is caused by the interference of the mass eigenstates, would vanish. However, if the experimental baseline is much smaller than the coherence length of the neutrino, the plane-wave assumption yields the same results as the wave packet approach. The width of a neutrino mass eigenstate was never measured precisely and is usually estimated from the neutrino creation process. The DAYA BAY experiment published an experimental upper limit on the relative intrinsic momentum dispersion (σ_{rel}) of reactor anti-neutrinos [29] of

$$\sigma_{\text{rel}} < 0.20 \text{ at } 95\% \text{ C.L.} \tag{2.12}$$

A large intrinsic momentum dispersion would impact the later discussed measurement of the *Neutrino Mass Ordering* by the JUNO experiment due to such decoherence effects [30]. In the following, the term *neutrino oscillations* will be used as a generic term to describe neutrino flavor conversions, even if the coherence is lost and the oscillatory behavior vanishes.

2.1.2 Matter effects in neutrino oscillations

In the process of traversing dense matter, neutrinos undergo coherent forward scattering, which must be taken into account when calculating neutrino oscillation probabilities [31, 32]. This effect is called the *Mikheyev-Smirnov-Wolfenstein* (MSW) effect. While all three neutrino flavors undergo neutral current interactions, only the electron flavor is affected by charged current interactions. In Eq. 2.5 the Hamilton operator in vacuum was used. This Hamilton operator needs to be modified to take the coherent forward scattering into account. In the two-flavor electron neutrino (dis-)appearance formula (Eq. 2.9 and 2.10), the effective mixing angle in matter changes to

$$\sin^2 2\theta_m = \frac{\sin^2 2\theta}{(w - \sin^2 2\theta)^2 + \sin^2 2\theta} \tag{2.13}$$

with

$$w = -\sqrt{2} G_F N_e E / \Delta m^2. \tag{2.14}$$

Here G_F is the Fermi-constant and N_e the electron density of the traversed matter. One can directly see in Eq. 2.14, that the MSW effect is highly dependent on the energy of the neutrinos as on the absolute value and the sign of the mass splitting. In the two-flavor model, the resonance character is directly visible for $w = \sin^2 2\theta$. If E and N_e take on certain values, maximal mixing can be reached. For anti-neutrinos, the MSW effect is reversed.

2.2 Overview of neutrino sources

Neutrinos can be measured at all energy scales. This section should give an overview over the many origins of neutrinos, their creation mechanisms and their implication for the current research, while the next section reviews the exploration of these sources regarding neutrino oscillations.

Cosmic neutrino background At lowest energy scales, neutrinos exist as the cosmic neutrino background [33]. Like the cosmic microwave background, the neutrinos forming the cosmic neutrino background decoupled from matter at a very early stage of the universe shortly after the Big Bang. The energy of these neutrinos can be estimated to be about 10^{-4} eV. Due to the challenges of measuring neutrinos at such low energies, the existence of the cosmic neutrino background was not confirmed experimentally so far.

Solar neutrinos Another source for neutrinos of much higher energy is the Sun as predicted in the *Standard Solar Model* (SSM) [34, 35]. These *solar* neutrinos are produced as electron neutrinos in nuclear fusion reactions in the core of the Sun. By far most abundant are neutrinos from the *proton-proton* (pp) reaction, which have an endpoint energy of 0.42 MeV. The measured solar neutrino spectrum ends at 14.6 MeV, which is reached by the neutrinos from the ^{8}B-decay. The measurement of solar neutrinos of several energies allows to improve the current understanding of solar models. Solar neutrinos are reaching Earth with a high flux of about 7×10^{10} particles/cm^2/s. Moreover, solar neutrinos are highly affected by the MSW effect through their propagation through the dense solar matter. This makes solar neutrinos also valuable for the measurement of neutrino oscillations in matter, especially for the measurement of θ_{12} and the sign of Δm^2_{21}.

Geo-neutrinos As Earth contains high amounts of radioactive isotopes, many neutrinos are created in β-decays in Earth [25, 36]. These are electron anti-neutrinos from the decays of ^{238}U, ^{232}Th and ^{40}K as well as electron neutrinos from the electron capture of ^{40}K. Most abundant geo-neutrinos from ^{238}U-decays have an endpoint energy of 3.26 MeV and geo-neutrinos from ^{232}Th-decays have a maximal energy of 2.25 MeV. The measurement of geo-neutrinos allows to test Earth-formation models, the radiogenic contribution to the heat production inside Earth, as well as the distribution of these radioactive isotopes.

Supernova burst neutrinos Another astrophysical source of neutrinos are these emitted during a *Super-Nova* (SN) [37, 38]. A SN in the Milky Way would release many neutrinos in a short burst on a time-scale of seconds. Depending on the SN model, neutrinos and anti-neutrinos can be measured at Earth in a clear time profile during the SN evolution. Approximately 10^{57} neutrinos are released in an average SN in a broad energy range with an average energy of about 12 MeV [39]. Due to the high numbers of neutrinos and the short time, the rate of neutrinos reaching Earth could be very high, depending on the distance of the SN. The measurement of SN neutrinos have several applications. Neutrinos from a SN explosion arrive earlier than its light. While optical telescopes can only observe a small portion of the sky at each time, neutrino detectors are not directed towards a specific area. This makes

SN neutrinos ideal to serve as an early warning for the optical measurement of a SN [40]. These measurements including the SN neutrinos would improve the current knowledge on the SN processes itself. Moreover, supernova burst neutrinos play an important role in the measurement of the MSW effect and the determination of the later described neutrino mass ordering. So far, only in the supernova event SN1987A, supernova burst neutrinos could be measured in several experiments [41–43].

Diffuse supernova neutrino background As a consequence of the last paragraph, besides the neutrino emission from a nearby supernova, it is also expected to have a *Diffuse Supernova Neutrino Background* (DSNB), which origins in many far-distant supernovae spread over the universe [44, 45]. In contrast to the previously described supernova burst neutrinos, the DSNB is a constant source of neutrinos. The measurement of the DSNB would improve our current knowledge on astrophysics, as the DSNB neutrino rate depends on the star formation rate, stellar masses, and the amount of *dark supernovae*.

Radioactive sources As neutrinos are emitted from radioactive isotopes, these can be enriched to form a strong source of electron neutrinos and anti-neutrinos. The endpoint of the emitted (anti-)neutrinos can reach from 18.6 keV (Tritium, β^--decay) to several MeV. Radioactive sources are used in the search for the *Neutrinoless Double-Beta decay* ($0\nu\beta\beta$-decay) in the search for the Majorana nature of neutrino masses. Moreover, neutrino sources can be used in the determination of the absolute neutrino mass [46] and in the search for a possible fourth neutrino generation [47].

Reactor neutrinos Nuclear power plants are used to create electric energy through controlled fission of radioactive material. These fission processes also emit electron anti-neutrinos as by-product. Due to the high demand on electric energy, nuclear power plants are built large and emit very large numbers of about 10^{20} $\bar{\nu}_e$/s. The electron anti-neutrinos are emitted via the fission of the reactor fuel isotopes ^{235}U, ^{239}Pu, ^{238}U, and ^{241}Pu [48, 49]. The relative abundances of these isotopes are depending on the nuclear reactor type and the burn-up status of the reactor core, which influences the measurable $\bar{\nu}_e$-spectrum. Electron anti-neutrinos are produced in a decreasing energy spectrum up to an energy of about 10 MeV, which is calculated in [48, 49], known as the *Huber+Mueller* model. This prediction of the reactor spectrum was measured to have imprecisions. It was reported in [50], that the measured anti-neutrino flux from reactors is about 6% less than the predicted flux by the Huber+Mueller model. This phenomenon is called the *Reactor Antineutrino Anomaly*. Moreover an excess of anti-neutrinos was observed at around 5 MeV [51, 52]. This excess was measured to be correlated with the reactor power, which hints for an imprecision in the spectrum prediction [53]. After reactor anti-neutrinos led to the neutrino discovery [2], they were used in the measurement of oscillation parameters in electron anti-neutrino disappearance experiments. Present and planned neutrino experiments use reactor anti-neutrinos in the determination of the sign of Δm^2_{32} and Δm^2_{31}, as well as in the search for a possible fourth neutrino generation. As this fourth neutrino generation is expected to show its major neutrino oscillation effects at very small baselines, the corresponding detectors are placed usually in the reactor buildings itself. Apart from its applications in neutrino physics, reactor anti-neutrinos are often discussed for monitoring of nuclear reactors due to the possible dangers in radioactive waste management,

nuclear weapon production, and reactor accidents [54].

Beam neutrinos It is possible to artificially produce beams of neutrinos in proton accelerating facilities [55]. The protons from the accelerator are stopped with a fixed target to produce mainly charged pions and kaons. These particles are focused in a magnetic focusing horn before they decay in a tunnel into muons and muon neutrinos. The further decay of the muons produces electrons, muon neutrinos, and electron neutrinos. Neutrinos as well as anti-neutrinos are created in such a beam facility. Other beam components beside neutrinos are absorbed in the rock or a beam absorber after the decay tunnel, such that only neutrinos propagate to the detector. As the main component, muon (anti-)neutrinos are produced in the beam production with typical energies up to 10 GeV. Depending on the polarity of the focusing horn, either neutrinos or anti-neutrinos can be majorly produced. The focus on the measurement of neutrino beams is to improve the understanding of neutrino oscillation physics. This includes the measurement of the CP-violating phase δ.

Atmospheric Neutrinos Similar to the production of beam neutrinos, neutrinos are produced in the atmosphere as a product of air showers [22]. Also here the neutrinos are mainly produced via the decay of kaons, pions, and muons, which are produced as secondary particles in an air shower. These neutrinos are called *atmospheric neutrinos*. While charged particles originating in an air shower can only be observed in the vicinity of the detector, the atmospheric neutrino flux from the whole atmosphere contributes to the flux at a specific position on Earth. As atmospheric neutrinos are created from cosmic rays, their energy spectrum is very broad, but typically in the ∼GeV range. Also atmospheric neutrinos are used to measure neutrino oscillation parameters and led to their discovery in the Super-Kamiokande experiment [56]. As they travel large paths through Earth, they are affected by the MSW effect, which makes it possible to determine the signs of Δm^2_{32} and Δm^2_{31} with the measurement of atmospheric neutrinos. Outside of neutrino oscillation physics, atmospheric neutrinos find applications in measuring Earth's structure and in astroparticle physics [57, 58]

Ultra-high energy neutrinos Highest energies are reached by neutrinos, which arrive at Earth as ultra-high energy cosmic rays [59, 60]. These neutrinos could be measured from high TeV-energies to several PeV. Neutrinos at such energies arrive at Earth with a very low flux. This makes it necessary to use very large target masses. These are realized by the instrumentation of large volumes, such as the Antarctic ice in the Ice Cube experiment [59, 60] or the water of the Mediterranean Sea in the KM3NeT telescopes [61]. Ultra-high energy neutrinos are not used in neutrino oscillation physics. They are used in astroparticle physics, especially due to their directional information, which is lost in charged primary cosmic rays.

2.3 Current status and open questions in neutrino physics

2.3.1 Neutrino oscillation parameters

Summarizing Sec. 2.1, neutrino oscillations can be described using the parameters from the PMNS matrix and the neutrino mass splittings. In the case of 3 neutrinos, there are two

independent mass splittings. Including the parameters from the PMNS matrix, which are 3 mixing angles and the CP-violating phase, these are 6 parameters to be measured.

The values in Table 2.1 were taken from [62]. They are representing the current knowledge on these parameters. The neutrino mass states are numbered with descending electron neutrino content. This defines ν_1 to be the neutrino with the highest electron flavor content and ν_3 the neutrino with the least electron flavor content.

Currently it is not known which of these neutrinos is the heaviest. The problem is commonly referred to as the *Neutrino Mass Ordering* (MO) problem. While the sign of Δm^2_{21} is measured to be positive, the sign of Δm^2_{32} and Δm^2_{31} depends on the MO. The two possibilities of the MO are usually named the *Normal Ordering* (NO), in which ν_3 is the heaviest neutrino, and the *Inverted Ordering* (IO), in which ν_3 is the lightest neutrino. In Table 2.1 the value Δm^2_{3l} stands for the mass splitting with the larger absolute value, Δm^2_{31} for NO and Δm^2_{32} for IO. Reference [62] was not able to reproduce the results from the Super-Kamiokande collaboration using atmospheric neutrinos using publicly available data. As this table is used here for illustrative purposes, the conservative values, excluding the Super-Kamiokande data from atmospheric neutrinos, are presented.

Table 2.1: The neutrino oscillation parameters from the global analysis in [62]. The mass splitting Δm^2_{3l} stands for mass splitting with the larger absolute value regarding the MO.

Parameter	NO (best-fit)	IO ($\Delta\chi^2 = 6.2$)
$\sin^2\theta_{12}$	$0.310^{+0.013}_{-0.012}$	$0.310^{+0.013}_{-0.012}$
$\sin^2\theta_{23}$	$0.558^{+0.020}_{-0.033}$	$0.563^{+0.019}_{-0.026}$
$\sin^2\theta_{13}$	$0.02241^{+0.00066}_{-0.00065}$	$0.02261^{+0.00067}_{-0.00064}$
$\delta_{CP}/^\circ$	222^{+38}_{-28}	285^{+24}_{-26}
$\Delta m^2_{21}/10^{-5}\,\mathrm{eV}$	$7.39^{+0.21}_{-0.20}$	$7.39^{+0.21}_{-0.20}$
$\Delta m^2_{3l}/10^{-3}\,\mathrm{eV}eV$	$2.523^{+0.032}_{-0.030}$	$-2.509^{+0.032}_{-0.030}$

One can clearly see the large difference between the small mass splitting Δm^2_{21} to the large mass splittings Δm^2_{32} and Δm^2_{31}. This allows many experiments to use the two-flavor neutrino oscillation probabilities (Eq. 2.9 and 2.10) as good approximation of the three-flavor formalism. In this scheme Δm^2_{21} and θ_{12} are often referred to as the *solar* parameters, as they were important for the measurement of electron neutrino disappearance of solar neutrinos. Major contributions to the mixing angle were made by the Super-Kamiokande experiment [9] and the SNO experiment [8], but also by the reactor neutrino experiment KamLAND [63], which measured also precisely the mass splitting in the channel using electron anti-neutrinos from surrounding reactors. KamLAND measures the electron anti-neutrino flux from many surrounding Japanese NPP with a large baseline of typically 180 km, which makes it sensitive for this oscillation channel.

The parameters Δm^2_{32} and θ_{23} are often called *atmospheric* parameters, as they were observed by Super-Kamiokande in the measurement of atmospheric neutrinos. These parameters are important for the muon neutrino disappearance probability. This oscillation channel is also measured by the beam neutrino experiments NOνA [12], T2K [64], and MINOS [65,

66]. As it can be seen in the two-flavor model, the neutrino oscillation probability depends in leading order on $\sin^2 2\theta$, which is measured to be close to 1 in the case of θ_{23} (compare Table 2.1). This leaves a large parameter space for $\sin^2\theta_{23}$, as a deviation from 1 is possible for either $\sin^2\theta_{23} < 0.5$ or $\sin^2\theta_{23} > 0.5$, which is known as the θ_{23}-*octant degeneracy*. The global analysis in [62] slightly prefers a value of $\sin^2\theta_{23} > 0.5$, but is not able to exclude $\sin^2\theta_{23} < 0.5$ significantly, which leaves the determination of the octant as an open question in neutrino physics.

The smallest mixing angle θ_{13} was measured precisely and proven to be non-zero by the experiments Daya Bay [67], Double Chooz [68], and RENO [69]. These experiments measure the electron anti-neutrino disappearance at baselines of about 1-2 km at about the minimum of the expected Δm^2_{31}-oscillation. Further measurements of this mixing angle are performed by the mentioned beam experiments using electron neutrino and anti-neutrino appearance. However, the precision of the θ_{13}-measurement in beam experiments is limited by the unknown θ_{23}-octant degeneracy.

2.3.2 Absolute neutrino mass scale

As the measurement of neutrino oscillations only allows to measure mass splittings, the absolute values can not be measured in the effect of neutrino oscillations. A direct approach to measure the neutrino masses is the measurement of the endpoint of the β-spectrum. This was done in the past in the Mainz neutrino-mass search [70] and the Troitsk experiment [71] with the β^--decay of Tritium. Currently, the running KATRIN experiment gives the best upper limit on the neutrino mass using the endpoint of the Tritium spectrum of $\langle m\rangle_e = \sqrt{\sum_i m_i^2 |U_{ei}|} < 1.1\,\text{eV}$ at 90% C.L [46]. During its full lifetime, the KATRIN experiment has a sensitivity of $\langle m\rangle_e = 0.2\,\text{eV}$. Similarly,the Project 8 experiment [72] aims to measure the β-spectrum of Tritium via *Cyclotron Radiation Emission Spectroscopy* (CRES) to reach a sensitivity of about 40 meV. Another direct measurement of the neutrino mass is the HOLMES experiment [73], which uses the electron capture reaction of ^{163}Ho.

A different approach to measure the neutrino mass is the measurement of the $0\nu\beta\beta$-decay [74]. These decays are only possible, if the neutrino is a *Majorana* particle, instead of a *Dirac* particle (see Sec. 2.3.3). The measurement of $0\nu\beta\beta$-decays would be sensitive to $m_{ee} = \sum_i m_i U_{ei}^2$. This mass depends on the Majorana phase α_1 in the PMNS-matrix. From their lower limit on the half-life of $T_{1/2}^{0\nu\beta\beta} > 10.7 \cdot 10^{25}\,yr$ of the $0\nu\beta\beta$-decay of ^{136}Xe, the KamLAND-Zen collaboration derived the currently most stringent upper limit of $|m_{ee}| < (61 - 160)\,\text{meV}$ [75].

Under certain model assumptions the sum of the neutrino masses can be retrieved from cosmology, especially from the measurements of the cosmic microwave background and large scale structures. The analysis of the data from the Planck satellite yields the current strongest upper limit of $\sum_i m_i < 0.23\,\text{eV}$ at 95% C.L. [76].

2.3.3 Nature of neutrino masses

As neutrinos are electrically neutral, they are allowed to be Majorana particles, which is represented by the existence of a Majorana mass. Contrary to a Dirac mass, a Majorana mass does not conserve the lepton number. Thus, a Majorana mass has the consequence, that

the neutrino mass eigenstates are their own anti-particles, even if also an Dirac mass of the neutrino mass eigenstates are present. As neutrinos are produced at ultra-relativistic energies, the difference between a Dirac and a Majorana neutrino vanishes, as the weak interaction violates parity. As a consequence of this parity violation, only neutrinos with left-handed helicity and anti-neutrinos with right-handed helicity are allowed to interact. Even if the neutrino is the same particle as its anti-neutrino, they would be distinguished by their helicity at sufficiently high energies, making it impossible to measure the Majorana nature of the neutrino mass.

The currently favored approach to address this question is the measurement of the $0\nu\beta\beta$-decay [77] as mentioned before. These decays would directly violate the lepton number and would not be allowed for neutrinos with pure Dirac masses. Contrary to the continuous energy spectrum of the electrons from $2\nu\beta\beta$-decays, $0\nu\beta\beta$-decays emit mono-energetic electrons at $E = Q_{decay}/2$, which makes both decays distinguishable. While the $2\nu\beta\beta$-decay was already measured with typical half-lifes of $T_{1/2} \approx 10^{19} - 10^{24}$, the current lower limits for the $0\nu\beta\beta$-decay half-life are about $T_{1/2} > 10^{26}$. The search for $0\nu\beta\beta$-decays is a highly active field with many current and future experiments contributing [77]. Among these, there are plans existing to use the JUNO detector, which will be described in Chapter 3, for the search for the $0\nu\beta\beta$-decay [78].

As it can be seen in Fig. 2.1, the allowed region for $0\nu\beta\beta$-decays depends on the MO of the neutrinos.

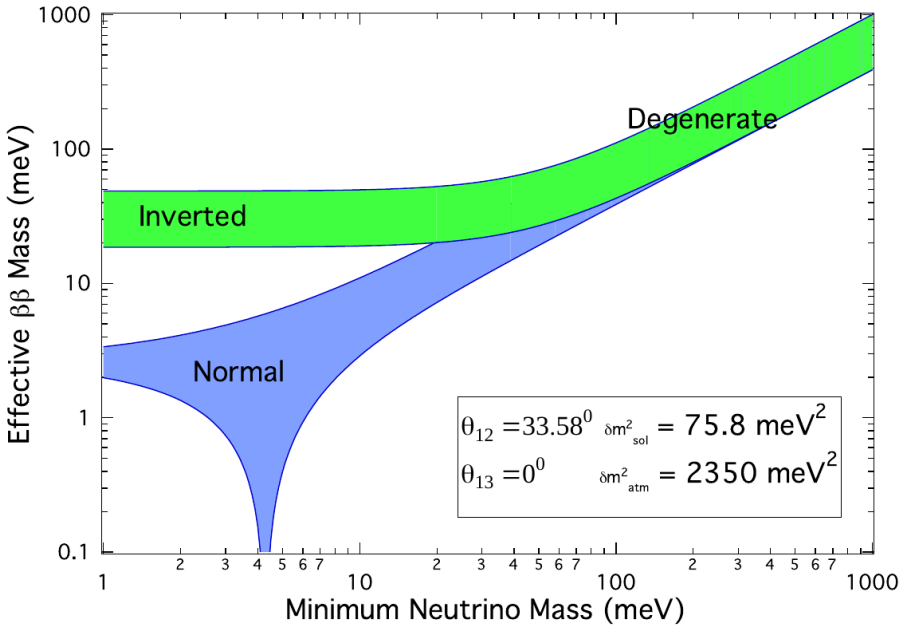

Figure 2.1: The allowed region for the $0\nu\beta\beta$-decay calculated with the shown parameters from [79]. The label *Effective ββ Mass* denotes m_{ee} and the label *Minimum Neutrino Mass* denotes the mass of the lightest neutrino. The green band shows the allowed region in the case of IO and the blue band shows the allowed region in he case of NO. For low values for the lightest neutrino mass, the allowed parameter spaces for the different MO are fully separated.

2.3.4 Leptonic CP-violation

The formalism of neutrino oscillations allows CP-violations through the phase δ in the PMNS matrix (Eq. 2.3).

The asymmetry of leptonic CP-violation $\mathcal{A}_{\alpha\beta} \equiv P(\nu_\alpha \to \nu_\beta) - P(\bar{\nu}_\alpha \to \bar{\nu}_\beta)$ is given by:

$$\mathcal{A}_{\alpha\beta} = 2 \sin 2\theta_{12} \cos\theta_{13} \sin 2\theta_{13} \sin 2\theta_{23} \sin\delta \sum_{\gamma} \epsilon_{\alpha\beta\gamma} \sin\frac{\Delta m^2_{21} L}{4E} \sin\frac{\Delta m^2_{31} L}{4E} \sin\frac{\Delta m^2_{32} L}{4E}, \tag{2.15}$$

with α, β, and γ describing the lepton flavors e, μ, and τ. It can be seen directly, that all mixing angles need to be non-zero for CP-violating processes to occur. The smallest mixing angle in the three-flavor model θ_{13} was confirmed to be non-zero in 2012 by the Daya Bay experiment [80]. For values of δ of 0 and 180°, there would be no leptonic CP-violation. This phase is being measured by neutrino beam experiments as the beams can change their mode from a neutrino mode to an anti-neutrino mode. Using the data from these experiments, the global analysis in [62] is not able to exclude CP-conservation. As it can be seen in Table 2.1, the measured value of δ strongly depends on the assumed MO. The current best-fit value is compatible with maximal CP-violation at $\delta = 270°$. This global analysis does not contain recently published results from the T2K experiment, which could exclude the non-existence of leptonic CP-violation with 97% confidence level for both, NO and IO [81].

The existence of CP-violating processes could explain the matter-antimatter imbalance in the universe. While the discovered CP-violation in quark mixing is too small to explain the matter-antimatter imbalance, the leptonic CP-violation could explain it, if it is measured to be large enough. One explanation would be the so-called *Leptogenesis* mechanism like it is described in [82], which is implied by leptonic CP-violation under the assumption of non-zero Majorana masses.

2.3.5 Neutrino Mass Ordering

One of the major problems in neutrino physics is the unknown MO, as introduced earlier in this section. Figure 2.2 illustrates the mass spectrum of the neutrinos in the three-flavor model. The MO can be measured in beam experiments with measuring the electron (anti-)neutrino appearance from initial muon (anti-)neutrinos. In this kind of experiments the MO is measured through the MSW effect. For NO, the electron neutrino appearance is enhanced and the electron anti-neutrino appearance is suppressed, while for IO the electron neutrino appearance is suppressed and the electron anti-neutrino appearance is enhanced. By measuring this asymmetry, the false MO can be rejected. Moreover, a phase shift to the oscillation pattern is introduced by the matter effect, which depends on the MO. This measurement channel is used by the NOνA experiment [12] and the planned DUNE-experiment [13]. Another similar approach is the measurement of oscillation probabilities from atmospheric neutrinos. In atmospheric neutrino experiments many baselines, typically represented by the zenith angle, as well as many energies are measured. The oscillation probabilities change in these experiments depending on the zenith angle and the energy due to the different MO. Also here the cause of these differences is the MSW effect. The measurement of the MO via atmospheric neutrinos is planned by the INO experiment [14], the PINGU experiment [15], the ORCA experiment [16], and the Hyper-Kamiokande experiment [17].

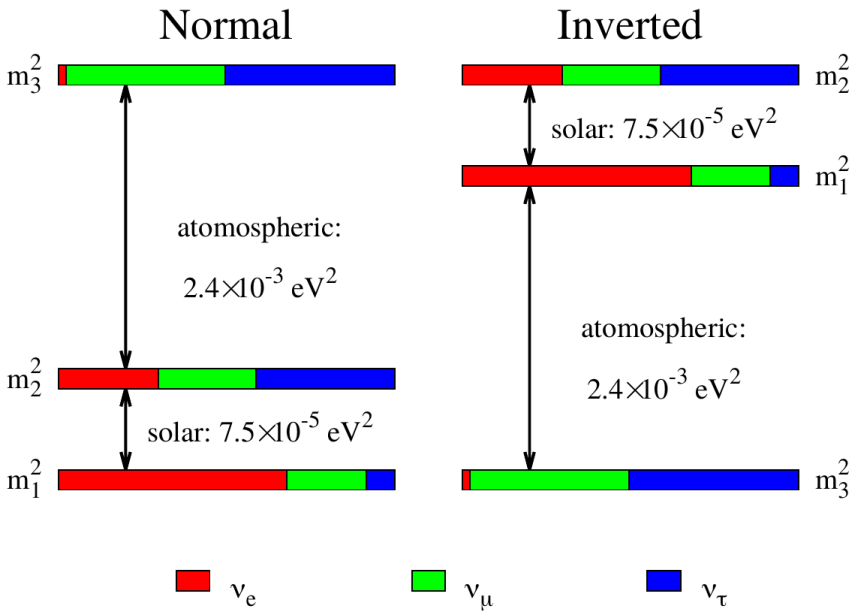

Figure 2.2: The two possible neutrino mass ordering schemes. The colors red (ν_e), green (ν_μ), and blue (ν_τ) illustrate the flavor composition of the mass eigenstates with the colored area being proportional to $|U_{\alpha i}|^2$. The size of the mass splittings is not drawn to scale. Taken from [11].

Complementary to measuring the MO by the MSW effect, it is possible to measure the MO directly from the vacuum electron (anti-)neutrino disappearance probability. The planned JUNO experiment [11], which will be described in detail in Ch. 3, and the proposed RENO-50 experiment [83] intend to measure the MO using reactor neutrinos. Figure 2.3 shows this vacuum oscillation probability (Eq. 2.11) with the well visible difference between the MO. The green area shows the expected measured spectrum of the JUNO experiment under the assumption of no oscillations. It is well visible, that the baseline of JUNO was optimized for the measurement of MO. The proposal of the RENO-50 experiment foresees a similar baseline and expects the same energy spectrum.

In the global analysis in [62], the IO can be excluded with $\Delta\chi^2 = 6.2$ without the atmospheric neutrino measurement by SK. With the atmospheric neutrino measurement by SK, this global analysis can exclude the IO with $\Delta\chi^2 = 10.4$, which is a strong hint towards NO.

The determination of the MO would be of great importance in the field of neutrino physics. As it can be seen in Fig. 2.1, the measurement of the MO confines the parameter space in the search for the $0\nu\beta\beta$-decay. Moreover, the MO is an important parameter in neutrino oscillation physics. Especially in the search for leptonic CP-violations, the MO takes a crucial role as the wrong assumption on the MO would lead to a wrong value of δ. As the MSW effect depends on the MO and reverses its effect for neutrinos and anti-neutrinos, the knowledge of the MO is crucial in the correction for the MSW effect. In models to explain the neutrino masses, mixing and its origin, the MO is of imminent importance. Also in astroparticle physics as well as in cosmology, the MO is a key parameter [11].

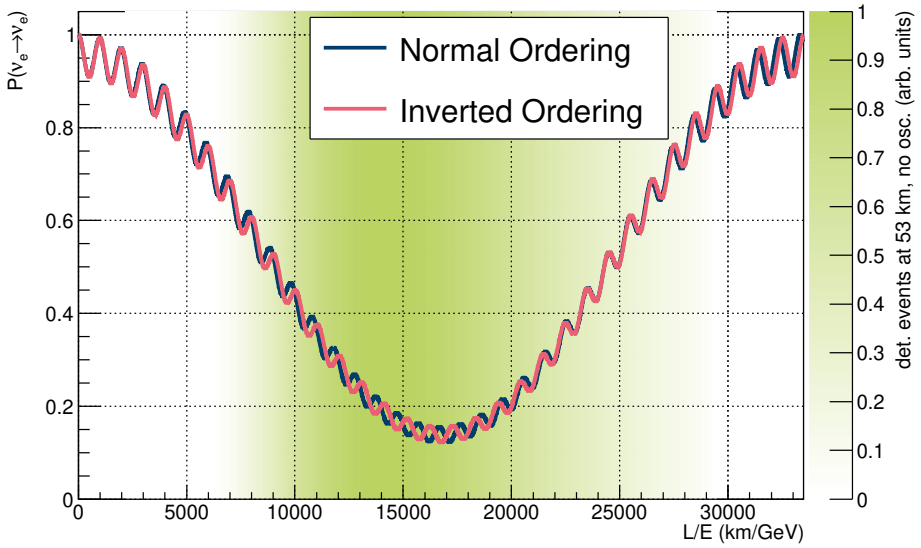

Figure 2.3: The measured L/E pattern for the neutrino mass ordering measurement using reactor neutrinos. The blue curve shows the vacuum electron neutrino disappearance (Eq. 2.11) for NO and the red curve shows it for IO using the values from Table 2.1. The green area shows the expected reactor anti-neutrino spectrum in a distance of 53 km. The expected spectrum was calculated using the Huber+Mueller model [48, 49] with the detection cross-section of the *Inverse Beta-Decay* (IBD) [84], which will be used in the JUNO experiment. It is visible, that this maximum of the spectrum lies near the maximal expected difference between the MO as the baseline of 53 km of the JUNO experiment was optimized to be maximally sensitive to the MO.

2.3.6 Sterile neutrinos

Measurements of the decay width of the Z-boson have shown the existence of three light neutrino flavors with $m_\nu < m_Z/2$ [85]. However, several experiments have found evident excesses and deficits from their expected neutrino rates, summarized in [86, 87]. One way to solve these deviations would be the introduction of a fourth neutrino mass eigenstate $|\nu_4\rangle$. The corresponding fourth flavor state $|\nu_s\rangle$ would be introduced then without introducing a fourth charged lepton making the neutrino flavor state inert under the weak force. This yields the name *Sterile Neutrino*. On the other hand, the flavor states participating in weak interactions are usually called *active* neutrinos. The mass eigenstate $|\nu_4\rangle$ would still participate in lepton mixing, thus leading to different appearance and disappearance probabilities in the neutrino oscillation formalism. Different to the three-flavor formalism, the oscillation pattern in L/E would not only occur in the charged-current interactions, but also in the neutral-current interactions of the weak force.

Sterile neutrinos are used to explain several measured event excesses and deficits in neutrino physics. For reactor anti-neutrinos these are the reactor anti-neutrino anomaly [50] and the reactor anti-neutrino excess around 5 MeV [51, 52]. As this excess is found to correlate with the reactor power, it is unlikely to be explained with sterile neutrinos.

Moreover, the LSND experiment [88] reported an significant excess of electron anti-neutrinos in an almost pure muon anti-neutrino beam. This excess can be interpreted as a higher electron anti-neutrino appearance probability. The MiniBooNE experiment [89] confirmed this excess significantly in electron neutrinos and electron anti-neutrinos, which is compatible with the results from the LSND experiment.

In the radio-chemical experiments GALLEX [90, 91] and SAGE [92], the cross-section for neutrino captures was measured to be lower than theoretically predicted. These experiments used the neutrino capture on ^{71}Ga to produce ^{71}Ge to measure the flux from solar neutrinos. This lower cross section is visible in the event rates in the calibration with radioactive sources, which is lower than expected. Also here, a possible explanation of the low event rates could be the disappearance of electron neutrinos at very low baselines, which is not expected in the three-flavor model.

To explain these effects, it is expected, that ν_4 has a rather high mass, such that $\Delta m^2_{4i} \approx 1\,\mathrm{eV}^2$ for $i \in \{1, 2, 3\}$. Also the precise measurements of the three-flavor mixing parameters only allow the fourth mass state to be mostly consisting of the sterile flavor state. Due to this high mass splitting, most searches for sterile neutrinos are conducted on very short baselines [86]. At these short baselines, it is expected to see the oscillatory behavior in L/E as it is expected from neutrino oscillations.

Chapter 3

The JUNO experiment

The *Jiangmen Underground Neutrino Observatory* (JUNO) is a next-generation neutrino experiment being under construction in Southern China expected to start data-taking in 2022. Its main detector part consists of a large 20 kton *liquid scintillator* (LS) target instrumented by a dense array of about 18,000 large 20" *Photo-multiplier Tubes* (PMT's) and 25,000 small 3" PMT's.The main goal of JUNO is to measure the MO. Following the assumptions in [11], a significance of 3-4 σ in 6 years is expected. Therefore, it will measure the oscillated energy spectrum of electron anti-neutrinos from two nuclear power plants at a baseline of about 53 km with an unprecedented energy resolution of 3% at 1 MeV. The measurement of reactor electron anti-neutrinos also aims to measure the oscillation parameters θ_{12}, Δm^2_{21}, and Δm^2_{32} to sub-percent precision. Furthermore, it intends to measure geo-neutrinos, solar-neutrinos, atmospheric neutrinos, supernova burst neutrinos, and the DSNB. The JUNO experiment is expected to improve the current knowledge on the proton lifetime in the decay into kaons.

This chapter should provide an overview of the current status and the physics programme of the JUNO experiment. It is based on the comprehensive overview of the JUNO experiment in [11], which is outdated in some points due to the active research and development in the JUNO collaboration. The updated status can be reviewed from recent conference presentations and their proceedings, which are held on behalf of the JUNO collaboration [93, 94].

3.1 Site and reactors

The JUNO experiment is located about 200 km to the west of the Pearl River Delta Metropolitan Region in the Guangdong Province in the south of China. It is placed in a distance of about 53 km to the *Yangjiang* and the *Taishan Nuclear Power Plants* (NPP). In order to achieve minimal smearing of the reactor electron anti-neutrino oscillation pattern, the reactor baseline variation is required to be smaller than 0.5 km. The location of the JUNO experiment is shown in Fig. 3.1.

The Yangjiang NPP has six reactor cores of the pressurized water reactor type *CPR1000* [96]. Since July, 2019 all cores are operational with a thermal power of 2.9 $\mathrm{GW_{th}}$. From the four reactor cores of the Taishan NPP, which were used in past studies of the JUNO experiment in [11], only two reactor cores were realized. They are of the *Evolutionary Power Reactor* (EPR)

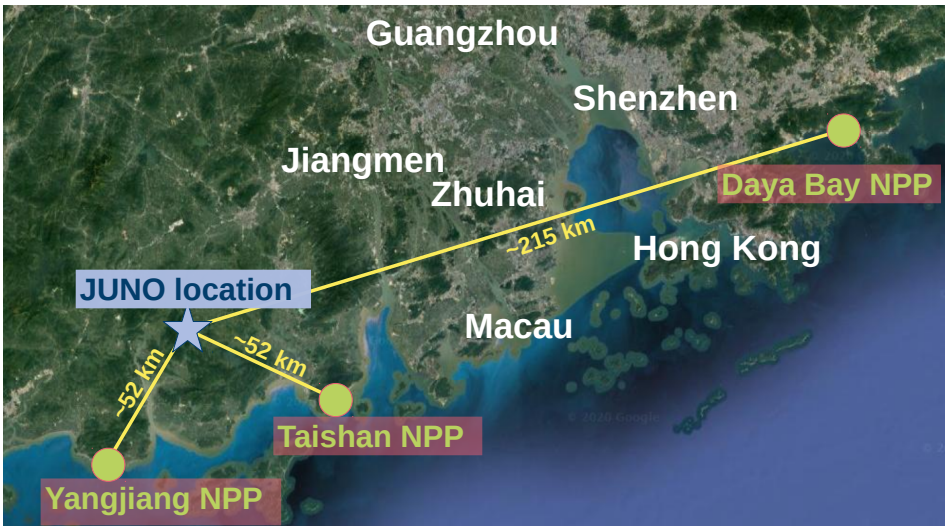

Figure 3.1: The location of the JUNO experiment in southern China. One can see locations of the Yangjiang NPP, the Taishan NPP, and the Daya Bay NPP as well as the cities of the metropolitan region. Map taken from [95] with location markers and names added externally.

type and are both operational with a thermal power of 4.9 GW_{th} since September, 2019 [96]. The total thermal power of the two NPP in 53 km distance is 26.6 GW_{th}.

The *Daya Bay complex* consists of the *Daya Bay* NPP, the *Ling Ao* NPP and the *Ling Ao-II* NPP with two reactor cores with 2.9 GW_{th} each. It is in a baseline of about 215 km from the JUNO site. As this baseline is not matched with the baselines of the Taishan NPP and the Yangjiang NPP, the neutrinos from the Daya Bay complex show a different oscillation pattern and are considered as background for the measurement of the MO.

Apart from the mentioned, there are no NPP in a region of 500 km radius around the position of JUNO.

To suppress background induced by cosmic muons, it is favorable for neutrino experiments to have a high rock overburden. For this reason, the detector cavern of JUNO is placed around 460 m under *Daishi Hill*, which is another 268 m high. The more than 650 m overburden in total is equivalent to about 1900 m of water.

The JUNO site is not connected to any existing infrastructure. Several surface buildings provide some of this local infrastructure. Besides buildings for the personal infrastructure like dormitories and offices, the surface buildings also provide buildings for the technical infrastructure. These include storage halls, power supply, as well as data storage and processing facilities. The underground facilities include, besides the main detector, rooms for data acquisition electronics and the LS handling.

3.2 Detector systems

The original proposed design in [97] consists of a single detector, the main detector. This main detector system is responsible for detecting events for the physics programme of JUNO,

described in Sec. 3.6. However, during the ongoing research and development of the JUNO collaboration it was found, that subsidiary detector systems might be necessary for JUNO to reach its physics goals. Described in Sec. 3.2.3, these are the OSIRIS detector for ensuring the radio-purity of the LS in JUNO and the TAO detector to measure a reference reactor electron anti-neutrino spectrum with negligible oscillation effects.

The main detector of JUNO can be further divided into several sub-detector systems. These are the *Central Detector* (CD), the *Water Pool* (WP), and the *Top Tracker* (TT). A schematic view of the main detector is shown in Fig. 3.2.

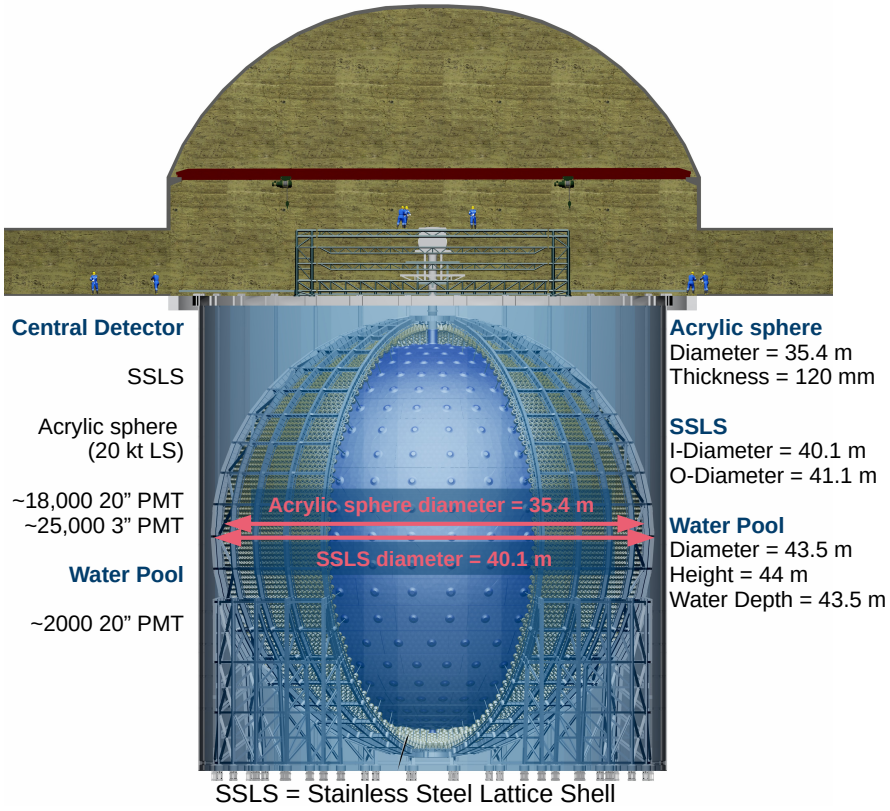

Figure 3.2: Scheme of the main detector of JUNO.

The purpose of the CD is the detection of the physics events for the broad physics programme of JUNO. Its driving requirements of the design are the energy resolution of 3% at 1 MeV and the large event statistics required by the MO measurement [11], which will be described in Sec. 3.6.1. Large event statistics are reached with the use of a large target volume of 20 kton of LS, contained in an acrylic sphere with a diameter of 35.4 m. The good energy resolution is based on the high photon statistics. Therefore, the LS volume is observed by about 18,000 large, 20” PMT’s and about 25,000 small, 3” PMT’s, which are attached to the surrounding *Stainless Steel Lattice Shell* (SSLS). The SSLS is also holding the acrylic sphere. The space between the SSLS and the acrylic sphere is filled with water and serves therefore as a buffer volume. As it is not an active scintillation volume, it does not produce light and shields the LS volume from several sources of radioactivity like the SSLS itself and the PMT array. The efficiency of large volume PMT’s is highly affected by magnetic fields. To shield them against

the Earth's magnetic field, coils are spanned around the CD, which provide a compensating magnetic field.

Optically separated, around the CD, is the WP. It is a cylindrical tank with a height of 44 m and a diameter of 43.5 m, which is filled with ultra-pure water up to 43.5 m. It is instrumented by about 2,000 large, 20"-PMT's, which are attached to the outside of the SSLS on the upper hemisphere of the CD and on the walls and the bottom of the WP below. The WP instrumentation is designed to detect cosmic muons which are entering the detector via their Cherenkov light emission, as they are a major source of background in LS experiments. Moreover, the WP adds another layer of shielding from the outside rock, which reduces the background rate. The needed ultra-pure water in the JUNO experiment will be produced in a water production and purification cycle on-site.

Another system for muon detection and tracking is the TT. It is a plastic scintillator strip detector from the decommissioned target tracker of the OPERA experiment [98]. These are arranged in 62 walls with a sensitive area of $6.7 \times 6.7\,\mathrm{m}^2$ each. Each of these walls divides in its eight modules, from which are four arranged in the same direction and the other four perpendicular to the first. Every module is 26.4 mm wide and consists of 64 plastic scintillator strips, which are each instrumented by a 64-channel multi-anode PMT. As the TT is expected to have a very high noise rate, introduced by background events from the radioactivity of the rock and detector material, it will be built in a 3-layer design, yielding coincident detection of passing muon events. In the design of the JUNO experiment, the TT is placed as a bridge centered on top of the WP, covering about 50% of its area. Together with the WP and the CD, the TT and its placement can be seen in the 3D-rendered image in Fig. 3.3.

The CD is accessible from the experimental hall via the chimney, which is placed on the top in the center. It will be used to deploy calibration sources into the detector.

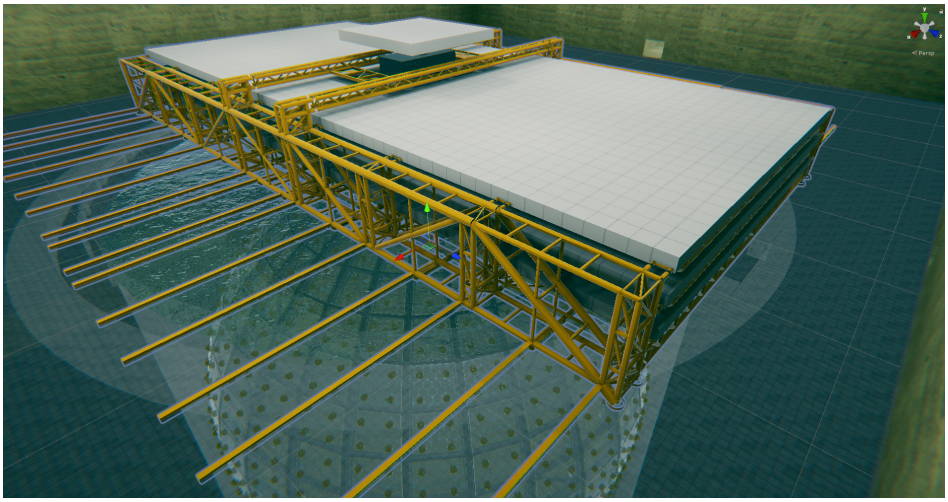

Figure 3.3: A 3D-rendered image showing the placement of the TT in the design of the JUNO experiment. From [99].

3.2.1 Liquid scintillator

As detection medium, the JUNO experiment uses LS, as it allows to be purified and cleaned in large amounts, allowing the construction of large detectors, like the 1 kton KamLAND detector [63], which is the largest LS detector built so far. Using LS, calorimetry is possible as the amount of emitted light is nearly linear to the deposited energy of the detected particle.

As the JUNO experiment requires a high energy resolution via high photon statistics, the LS needs to have a good light yield and, due to the large size of the JUNO detector, an excellent transparency. Low chemical reactivity ensures the chemical stability and a high flash point aids the safety in the use of the LS. Moreover, the LS needs a precise timing as it affects strongly the resolution of the vertex reconstruction. Due to light non-uniformity effects, an imprecise vertex reconstruction directly affects the quality of the energy resolution.

To reach these goals, the JUNO experiment uses *linear alkylbenzene* (LAB) as solvent for the LS mixture, based on the experiences from the Daya Bay experiment [100]. LAB is a straight alkyl chain of 10-13 carbon atoms attached to a benzene ring. The ionization energy loss of traversing charged particles leads to the excitation of electrons in the LS molecules. The emission spectrum of the solvent of a LS is slightly shifted to the absorption spectrum due to the stokes shift [101]. In order to make the LS transparent to its own light emission, an organic fluor is added in LS mixtures. In the case of the JUNO experiment, 2,5-di-phenyloxazole (PPO) is used as fluor in a concentration of 2.5 g/l. The fluor absorbs the emitted photons from the solvent and re-emits them at higher wavelength, allowing them to propagate through the LS. As the emission wavelength of about 390 nm of PPO does not allow efficient detection with PMT's, p-bis-(o-methylstyryl)-benzene (bis-MSB) with an emission wavelength of about 430 nm is added as a wavelength shifter in a concentration of 1-3 mg/l.

Besides the chemical composition of the LS mixture, the cleanliness and radio-purity of the LS is important. To ensure these, a purification plant is planned on-site in the underground laboratory of the JUNO experiment [102]. As there are no storage options for the large amounts of the JUNO LS, it needs to be purified directly before it is filled into the CD. The purification plant uses several techniques. Using an AlO column, it filters the LS to remove impurities. This increases the attenuation length. By distilling the LS, heavy elements are removed and the transparency is increased. Radioactive heavy isotopes, namely Uranium, Thorium, and Potassium are removed by water extraction and the noble gases Argon, Krypton and Radon are removed via gas stripping. For the MO analysis (Sec. 3.6.1) concentrations of less than 10^{-15} g/g of ^{238}U and ^{232}Th are required, while for the solar neutrino analysis (Sec. 3.6.2) concentrations of less than 10^{-16} g/g are required. These high requirements of the radio-purity of the JUNO LS were only achieved by the Borexino [24] and the KamLAND [103] experiment so far.

The functionality of the purification plant for JUNO is being tested at one of the detectors of the Daya Bay experiment [102]. Moreover, the OSIRIS detector, described in Sec. 3.2.3, is planned to measure the radio-purity of the LS before it enters the CD, in order to detect failures of the purification plant.

After purification, the JUNO LS is expected to have a light yield of about 10,000 emitted photons for 1 MeV deposited electron energy and an attenuation length of more than 20 m. The timing of a LS mixture depends on the energy loss per path length and therefore on the particle type. If the difference of the time profiles of two particles, which deposited energy in

the LS, is large enough, these time profiles can be assigned to a particle type. The distinction of different scintillator time profiles is usually called *Pulse Shape Discrimination* (PSD).

In [104] the time profile of LAB was measured for different PPO concentrations. Figure 3.4 shows the time profile of LAB with a PPO concentration of 3 g/l.

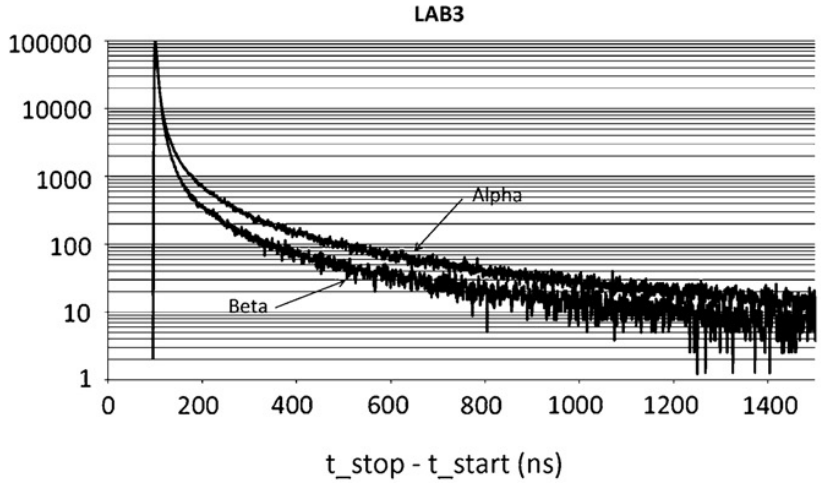

Figure 3.4: Measured time profile of LAB with a PPO concentration of 3 g/l. The different time profiles for α- and β-particles are shown. Taken from [104].

^{14}C contamination

As LAB is an organic substance, it consists mainly of carbon and hydrogen. Therefore, another important radioactive contamination of the LS is the radioactive isotope of carbon, ^{14}C. Natural carbon consists mainly of the isotopes ^{12}C (∼99%) and ^{13}C (∼1%), which are both stable. Due to the interaction of cosmic rays with the stratosphere and troposphere, thermal neutrons are produced. These neutrons may interact with ^{14}N atoms, forming ^{14}C and free protons [105], giving the major source of ^{14}C in the atmosphere[1]. The isotope ^{14}C is unstable and undergoes the β-decay

$$^{14}\mathrm{C} \rightarrow {}^{14}N + e^- + \bar{\nu}_e \tag{3.1}$$

with a half-life of 5730±40 years [108] and a decay energy of $Q = 0.156\,\mathrm{MeV}$ [109]. Typical values for the ^{14}C concentration in the atmosphere are around 10^{-12} ^{14}C atoms per ^{12}C atom. Organic LS is produced out of fossil petroleum, in which major amounts of the ^{14}C already decayed. The JUNO LS is required to have a ^{14}C concentration of less than 10^{-17} ^{14}C atoms per ^{12}C atom [11]. However, due to the chemical similarity of ^{14}C to ^{12}C, the concentration of ^{14}C can not be reduced by purification, but only through to the selection of raw materials in the LS production. In the case of the JUNO experiment, it means, that a high initial ^{14}C concentration can not be reduced by purification and needs to be taken into account in the data-analysis. Even as the upper limit for the ^{14}C concentration seems to be small, due to

[1] Artificial sources of ^{14}C are the tests of nuclear weapons [106] and nuclear power plants [107].

the high amount of carbon atoms in the JUNO LS, it corresponds to a total activity of about

$$\frac{20\,\mathrm{kton}}{232\,\mathrm{g/mol}} \cdot N_{\mathrm{Avogadro}} \cdot c_{\mathrm{LAB}} \cdot c_{14\mathrm{C}} \frac{5730\,\mathrm{years}}{\ln(2)} \approx 40\,\mathrm{kBq}, \tag{3.2}$$

with c_{LAB} being the amount of carbon atoms per LAB molecule and $c_{14\mathrm{C}}$ being the concentration of 10^{-17} ^{14}C atoms per ^{12}C atom, assuming a sum formula for LAB of $C^{17}H^{28}$.

3.2.2 PMT array

Operating principle

PMT's have been found to be a highly efficient solution to detect light on the intensity level of single photons. The principles of light detection for different kinds of PMT's is described in detail in [110] and shown exemplary in Fig. 3.5 on the scheme of a conventional dynode PMT. In a PMT, an incoming photon hits the photo cathode behind the PMT surface glass and emits

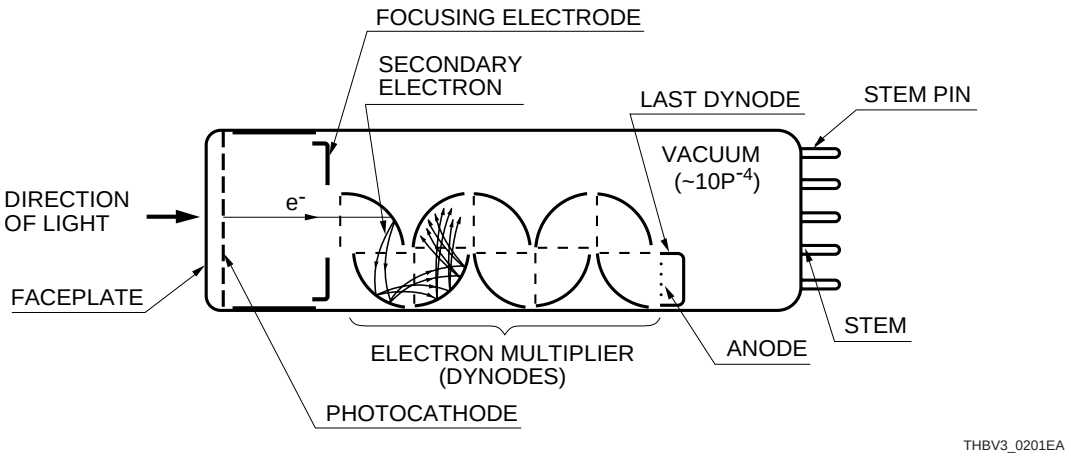

Figure 3.5: Scheme of the working principle of a PMT. From [110].

a so-called *photo-electron* (p.e.) via the photo-electric effect. This electron is accelerated to the first dynode to knock-out more electrons upon hitting the dynode. By using multiple dynode stages, high multiplications are reached until the cascade of electrons reaches the anode. For the acceleration of the electrons, the PMT is connected to a high voltage generator with usually 1-2 kV with a voltage divider, such that there is a potential gradient from the photo cathode over the consecutive dynodes to the anode. The high number of electrons at the anode can be measured as a short voltage drop, which is separated from the high voltage using a *splitter* module. An observable to describe the signal strength is the integral of the voltage difference to its baseline. This signal strength is typically called *charge*. If more than one p.e. is amplified, the measured charge increases nearly linear to the amplified p.e. number.

A different approach to using a discrete dynode structure is the use of *microchannel plates* (MCP) for electron multiplication. A MCP consists of a great number of parallel capillaries (channels) on a disk. Each inner wall of the channels is processed to have the right electrical resistance and secondary electron emission properties to act as an electron multiplier. Analogous to the dynode PMT design, the dynodes in an MCP PMT are replaced by the

inner walls of the MCP. As the channels have a small diameter of just a few micrometers, the amplification in the MCP is less affected by the deflective effects of magnetic fields than the amplification in a dynode structure.

Various parameters describe the properties of a PMT. Among the most crucial parameters for the light detection in the JUNO experiment are the *detection efficiency* (DE), the *dark count rate* (DCR), and the *transit-time spread* (TTS). The DE is the product of the so-called *quantum efficiency* (QE) and the *collection efficiency* (CE). The QE describes the ratio of emitted p.e.'s to incident photons at the photo cathode. It depends mainly on the material of the photo cathode and on the wavelength of the incident photons. The CE is defined as the ratio of p.e.'s, which land on the effective area of the first dynode to total emitted p.e.'s. The DE can be therefore understood as the probability to measure the signal caused by an incident photon.

As a PMT is designed to by a highly sensitive photo-detector, it will produce false signals, called *dark counts*. Typically these are caused by thermionic emission of electrons in the photo cathode or dynode. As caused by such, the DCR depends on the operating temperature, the design of the photo cathode, and the applied high voltage.

After the p.e. is emitted at the photo cathode, it needs the transit time until it is amplified and measurable as electric current. While the central value of this time only creates a constant offset, which can be determined in calibration studies, the spread of this time, the TTS, directly translates to an uncertainty in the photon detection time. The TTS is typically given as the FWHM of the distribution.

Large PMT array

The large PMT array of the JUNO experiment, uses PMT's with a diameter of 20", which will be called *LPMT's* in the following. It uses both, the dynode PMT type R12860 [111] from the Hamamatsu Photonics company and a MCP PMT type [112], designed for the JUNO experiment, produced by the NNVT company. In the CD, it is planned to use about 18,000 LPMT's, 5,000 dynode and about 13,000 MCP PMT's. These LPMT's will reach a optical coverage of the CD of 75%. Additional 2,000 MCP PMT's will be used to instrument the WP.

Among other parameters, the DE, DCR, and TTS for each of the LPMT's are being measured by the JUNO collaboration using dedicated experimental setups [113, 114]. This testing serves the purpose of rejecting LPMT's, which are not satisfying the requirements stated by JUNO collaboration on each LPMT. Here, three types of LPMT's can be distinguished: Dynode PMT's, High-QE MCP PMT's, and Low-QE MCP PMT's. High-QE MCP PMT's are a newer version of the Low-QE MCP PMT's with an improved photo cathode, which reaches higher QE values. From the total of 15,000 MCP PMT's used in the JUNO experiment, about 5,000 are expected to be High-QE MCP PMT's, which are all planned to be installed in the CD. Table 3.1 summarizes the obtained values from the PMT testing from [114]. With the optical coverage and the shown DE's, the full LPMT array of JUNO is expected to detect about 1200 p.e./MeV from the emitted scintillation photons. This rather high number of detected p.e. is needed to reach the energy resolution of 3% at 1 MeV.

[2] As the TTS of the LPMT's was not measured in the testing site so far, these values are given by the vendor in [111] for the dynode PMT's and [112] for the MCP PMT's.

Table 3.1: Measured parameters of the LPMT system from [114]. These parameters were not measured with the final optimized readout electronics and must be seen as preliminary values.

	Dynode PMT's		MCP PMT's		
Parameter	Requirement	Average	Requirement	Average (High-QE)	Average (Low-QE)
DCR (kHz)	< 50	15.3	< 100	48.7	47.9
DE (%)	> 24	28.1	> 24	30.1	26.9
TTS (ns)	< 3.5	$(2.4)^2$	< 15	$(12)^2$	$(12)^2$

To measure the charge and the photon detection time in each LPMT, they are connected in groups of three LPMT's each to *under water boxes* (UWB's), which contain readout electronics [115]. The central part of these readout electronics is the *Analogue-to-Digital Unit* (ADU), which allows the measurement of the time evolution of the LPMT signal. It records the LPMT signal with a digitized time in a range of up to 1000 p.e. in 1 ns steps. The signals from each UWB are send via Ethernet cable to centralized electronic parts, where the UWB clocks are synchronized and the global trigger is formed. For the global trigger, a vertex fitting logic is planned, which creates a positive trigger if the PMT hit multiplicity under the assumption of a possible vertex is high enough.

Small PMT array

To apply the concept of *double calorimetry* [116] in JUNO, an additional system of about 25,000 small 3" PMT's (SPMT's) is planned to instrument the CD, placed in the gaps between the dense LPMT array. The SPMT's are of the type XP72B22 of the HZC company [117]. If a PMT detects more than a single photon at a time, the amount of measured charge does not increase linearly with the amount of detected p.e. This effect is usually called *electronics non-linearity*. As each SPMT covers only about 1/50 of the area of a LPMT, multiple photon hits are unlikely and the effect of electronics non-linearity is highly suppressed. The SPMT array is designed to work entirely in the *photon-counting* mode for events with visible energies in the reactor electron anti-neutrino range. This property allows the electronics non-linearity calibration of the LPMT system. Moreover, while the LPMT's are expected to show saturation effects at high energies, e.g. from atmospheric neutrino events, the SPMT array are less affected by those and can help in calorimetry.

3.2.3 Subsidiary detector systems

OSIRIS

The radio-purity of the LS in JUNO is crucial for the success of the experiment. As the internal radioactivity events are in the energy region of the low energy solar neutrino measurements, they influence these measurements the most. For the reactor electron anti-neutrino measurement, the internal radioactivity is a source of the *accidental* background and the (α, n)-background, which will be introduced in Sec. 3.6.1. Moreover, due to pile-up of the radioactivity events with events from reactor electron anti-neutrinos, the radio-purity of the LS also has an influence on the MO measurement. Therefore, the JUNO collaboration has set

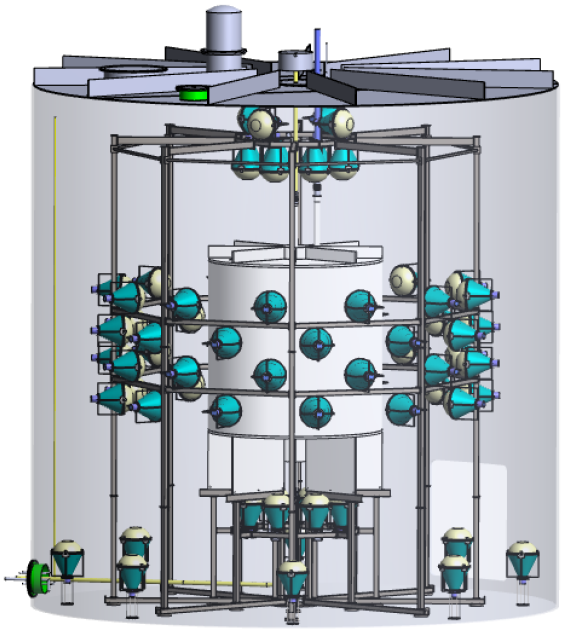

Figure 3.6: The OSIRIS detector design.

stringent limits on the radio-purity level of the LS. For the solar neutrino analysis of JUNO a requirement of a ^{238}U and ^{232}Th concentration of less than 10^{-16} g/g is formulated while for the MO analysis a concentration of less than 10^{-15} g/g is required. The purpose of *OSIRIS* (Online Scintillator Internal Radioactivity Investigation System) is to ensure that the LS of JUNO meets these requirements [118]. Its baseline design intends to measure the contamination of the LS by the natural decay chains of ^{238}U and ^{232}Th. The principle of measurement is the tagging of the fast time-coincident decays of the isotope pairs ^{214}Bi-^{214}Po and ^{212}Bi-^{212}Po. The rate of the measured ^{214}Bi-^{214}Po and ^{212}Bi-^{212}Po coincidence events can then be converted into a concentration of ^{238}U and ^{232}Th. OSIRIS is designed to reach the required sensitivities in the measurement time of about one day. If the LS purification process has a leak, which introduces a contamination by Radon in the scintillator, it will be also detected by OSIRIS. Additionally to the tagging of Bi-Po coincidences, which drives the development of OSIRIS, it is capable of measuring the ^{14}C concentration down to a ratio of 10^{-17} ^{14}C/^{12}C at 90% confidence level. The capability of detecting a contamination with ^{210}Po is still under investigation.

The OSIRIS detector design is shown in Fig. 3.6. It consists of two vessels. The inner vessel is an acrylic glass cylinder with a diameter and heights of each 3 m. It holds the scintillator and is observed by 64 LPMT's, which are the same dynode PMT type as in the CD. These PMT's are held by a steel frame which is fully contained in the outer vessel. Due to the purpose of OSIRIS of constantly observing the LS, which is to be filled into the JUNO detector, it has an inlet on the top and an outlet in the bottom of the inner vessel. Both, the inlet and the outlet, are equipped with an diffusor to ensure an equal distribution of the scintillator in the vessel. This outer vessel, a stainless steel cylinder, which is filled with water, serves as buffer volume to shield against external radioactivity from the surrounding rock. Additional 12 LPMT's are observing this volume to use it as a veto detector against cosmic muons. Both vessels are

optically separated. The diameter and heights of the outer vessel are also 9 m each. These dimensions are limited by the available space in the JUNO underground LS hall.

The readout design of the OSIRIS LPMT's will use a novel approach. To maximize the quality of the signal, the readout electronics as well as the digitizer is placed directly at the base of the PMT. This enables better impedance matching of the PMT base and therefore a higher quality of the signal. The PMT's are sending a digital signal to the data acquisition system, which can contain either the full pulse form or an already extracted time and charge information of the hit.

TAO

The spectral structure of the reactor electron anti-neutrinos is only known with a limited precision, allowing currently unknown but possible fine structures [119]. These could cause the MO measurement of JUNO, described in Sec. 3.6.1, to be unfeasible as it relies on the precise knowledge of the reactor electron anti-neutrino spectrum. To measure this spectrum precisely the *Taishan Antineutrino Observatory* (TAO) is planned [120], following the suggestion in [121]. It consists of a small spherical detector, which holds about 2.6 tons of Gadolinium-doped LS, of which about 1 ton is used as fiducial volume. The doping with Gadolinium is a common technique to enhance the neutron tagging efficiency in LS experiments [67–69]. As to be described in Sec. 3.3, the neutron tagging efficiency is of major relevance for detecting electron anti-neutrino events. This detector is placed in a very short distance of about 30 m to a core of the Taishan NPP. To assist the JUNO experiment with a highly precise reference spectrum for reactor electron anti-neutrinos, the TAO detector is instrumented by *silicon photo-multipliers* (SiPM's) with a DE of about 50%. These SiPM's can be densely packed over the inner surface of the TAO detector to reach nearly full optical coverage. To reduce the DCR of the SiPM's, the whole detector is cooled to a temperature of about $-50\,^{\circ}\mathrm{C}$. With about 4500 p.e./MeV detected, the TAO detector is expected to reach an energy resolution of about 1.5% at 1 MeV.

Apart from providing the highly precise reference spectrum, TAO is expected to improve nuclear databases.

A detailed description of the TAO detector by the JUNO collaboration is in preparation [122].

3.3 Particle interactions and detection at MeV-scale energies

Different particles show different interactions with the detection medium, the LS. These can be distinguished into charged particles, which can be directly detected through the ionization of LS molecules, and uncharged particles, which are detected only via the creation of secondary charged particles. This section introduces the different interaction channels of different particles in the JUNO LS. The description of the light production of electrons, gammas, and positrons will be studied in detail in Chapter 4, while this section introduces the principles of differences of light production for different particles.

As the study of reactor electron anti-neutrinos in JUNO is in the main focus of this thesis, this section focuses on the energy scale below 10 MeV and LS as the detection medium. The total

detection energy range of the physics programme of JUNO starts from the sub-MeV scattered electrons from solar neutrinos up to the detection of muons and electrons from GeV-scale atmospheric neutrinos [11].

3.3.1 Charged particle detection

Electrically charged particles deposit kinetic energy in the liquid scintillator via the ionization and excitation of the medium [22]. As in each of the interactions with the medium, typically only some eV of the MeV-scale energy are transferred, the energy deposition can be seen as a continuous process. This deposited energy will be called *ionization energy* in the following. For electrons, protons, and α-particles it is the dominant energy loss channel. Due to their light mass, electrons of sufficiently high energy can also loose energy through the emittance of gammas due to Bremsstrahlung. The deposited ionization energy causes the production of scintillation light. Moreover, independent of the scintillation process, Cherenkov light is produced by charged particles.

Ionization quenching

As the light output increases with the number of primary excitations in the medium, it increases with the amount of deposited ionization energy. If the density of excited molecules is sufficiently low, the light output increases linearly with the amount of deposited ionization energy. At the end of the particle's track, the energy loss per unit depth[3] $\langle \mathrm{d}E/\mathrm{d}X \rangle$ increases sharply. This increases also the density of excited molecules. Due to interactions between the molecules, which occur at high excitation densities, the light output per ionization energy of scintillation light is reduced. This effect is called *ionization quenching*. Low initial particle energies causing it to deposit high fractions of its energy with high $\langle \mathrm{d}E/\mathrm{d}X \rangle$. This causes the scintillation light output of the LS to be increasing non-linearly with the particle's energy. Heavy charged particles like protons and α-particles have a much higher $\langle \mathrm{d}E/\mathrm{d}X \rangle$ at the same kinetic energy as positrons or electrons. This causes a higher suppression of the light output for heavy charged particles.

The light output of a scintillator per unit depth, including ionization quenching, is empirically parametrized by Birks' formula

$$\left\langle \frac{\mathrm{d}L}{\mathrm{d}X} \right\rangle = L_0 \frac{\left\langle \frac{\mathrm{d}E}{\mathrm{d}X} \right\rangle}{1 + kB \left\langle \frac{\mathrm{d}E}{\mathrm{d}X} \right\rangle}, \tag{3.3}$$

where L is the light yield, L_0 is the scintillation light yield normalization, $\langle \mathrm{d}E/\mathrm{d}X \rangle$ is the energy loss of the particle per unit depth, and kB is the Birks' material constant [123]. The parameter L_0 can be interpreted as the scintillation light output under the absence of ionization quenching.

Cherenkov light

Besides scintillation light, also Cherenkov light is used to detect charged particles in LS experiments. Cherenkov light is caused by the short-timed polarization of atoms along the

[3] The unit depth $\mathrm{d}X$ describes the traveled unit distance $\mathrm{d}x$ weighted with the density of the medium ρ.

propagation path of charged particles. For slow non-relativistic particles, the radiation caused by such polarizations of nearby atoms interferes usually destructively, so that no light can be detected. However, if the particle velocity exceeds the phase velocity of light in the medium, the emitted radiation interferes constructively, creating a coherent detectable light cone. This can be translated to a mass-dependent threshold energy for the emission of Cherenkov light

$$E_{\text{thr}} = \frac{mc_0^2 n(\omega)}{\sqrt{n^2(\omega) - 1}} - mc_0^2, \tag{3.4}$$

with the particle mass m, the light frequency-dependent refractive index $n(\omega)$, and the light vacuum velocity c_0. In the considered energy range, only electrons and positrons produce Cherenkov light. Using an approximate refractive index of $n = 1.5$ for the considered LS mixture, the Cherenkov threshold for electrons and positrons is about 0.17 MeV. The emitted spectrum and amount of Cherenkov light is described by the Frank-Tamm formula [124]:

$$\frac{\mathrm{d}^2 E}{\mathrm{d}x \mathrm{d}\omega} = \frac{q^2}{4\pi} \mu(\omega) \omega \left(1 - \frac{c_0^2}{v^2 n^2(\omega)}\right), \tag{3.5}$$

where q stands for the particle's charge, $\mu(\omega)$ the permeability of the medium, and v the particle's velocity. Cherenkov light is typically emitted at short wavelengths. This is causing the Cherenkov light to be absorbed and re-emitted as scintillation light [125]. Therefore, in the JUNO experiment, the contributions from Cherenkov light and scintillation light to the total light output of the scintillator can not be distinguished. In the case of electrons and positrons, Cherenkov light is expected to contribute by a few percent to the total detected light in the JUNO LS.

Positrons

The energy deposition of positrons needs a more complex description than the one of electrons as it happens typically in two steps. First, the positron deposits kinetic energy like other charged particles in form of ionization energy in the scintillator. After that, the positron annihilates with an electron of the detector material or forms positronium with it. The positron annihilation releases two gammas. The most common case is the positron annihilation at rest with the production of two gammas with the energy of $E_\gamma = m_e c^2 \approx 511\,\text{keV}$ each. If positronium is formed, there is a chance to form para-positronium (p-Ps) or ortho-positronium (o-Ps) [126, 127]. If o-Ps is formed in vacuum, it can not decay into two gammas as o-Ps has a total spin of 1 and therefore needs to decay into an odd number of photons. Due to this reason o-Ps has a much longer vacuum lifetime of 142 ns compared to p-Ps with 125 ps. However in matter, several effects like chemical reactions, spin-flip at para-magnetic centers, or pick-off annihilation with another anti-parallel spin electron, cause o-Ps to decay into two gammas instead of three. This causes the lifetime of o-Ps to be measured in the order of a few nanoseconds in matter [128].

3.3.2 Neutral particle detection

Electrically neutral particles do not directly deposit ionization energy in the scintillator in a continuous energy loss process. Instead, they interact with the LS medium in discrete particle

reactions to produce secondary charged particles, which can produce ionization energy. The important electrically neutral particles in JUNO are gammas and neutrons. The detection of neutrinos will be the focus of the next subsection.

Gammas

Gammas are interacting with the LS with several particle reactions [22], whose cross sections can be extracted from [129]. Below the energy of $E_\gamma = 2 \cdot m_e c_0^2$, gammas can undergo three types of interaction with matter. These are Compton scattering, Rayleigh scattering, and the photo-electric absorption. Compton scattering is the incoherent scattering of a gamma with an electron of the medium. For this type of scattering, a fraction of the gamma energy is transferred to the electron, depending on the energy of the gamma and the scattering angle. During the Rayleigh scattering process, the coherent scattering, no energy is transferred to the scattered-off electron of the medium, just the direction of the gamma is changed. If the energy of the gamma becomes low, the dominant interaction process becomes the photo-electric absorption. In this process, the gamma transfers its full energy to an electron of the medium. Above the energy of $E_\gamma = 2 \cdot m_e c_0^2$, gammas can produce electron-positron pairs in the fields of electrons or nuclei of the LS medium.

In the considered energy regime below 10 MeV, a gamma dominantly undergoes Compton scattering several times until it is absorbed via the photo-electric effect. The scattered-off electrons deposit their energy in form of ionization energy in the scintillator, producing detectable light. Gammas can travel distances on the centimeter-scale between single Compton scattering processes in the LS. Compared to single electrons, which travel only a few millimeters, their signal is spread over a larger region. Figure 3.7 shows an example distribution of deposited energy for electrons and gammas in the JUNO detector evaluated by the JUNO software, which will be introduced in Sec. 3.5. Both particles were simulated with a kinetic energy of 1 MeV, traveling in the x-direction in the JUNO detector. The figure shows the energy depositions at different positions projected on the x-y-plane with the color scale. Additionally, the tracks of electrons are shown in blue, while gamma tracks are shown in red. One can clearly see, that the simulated electron continuously deposits energy along its relatively short track of a few millimeters. Contrary to that, the simulated gamma travels a relatively long path of tenth of centimeters without any energy deposited until it starts to create secondary electrons. These secondary electrons deposit their energy approximately point-like compared to the long paths of the gamma between interactions.

Neutrons

In LS experiments one can distinguish thermal neutrons and fast neutrons due to their different interactions.

Thermal neutrons are detected mainly via their capture reaction on free protons in the LS. The cross section for such a capture reaction increases with decreasing neutron energy [130]. If a neutron is captured on a free proton, a deuteron is formed and a gamma with the deuteron binding energy of about 2.2 MeV is released [11]. Another less abundant neutron capture reaction is the one on Carbon with an energy release of about 4.9 MeV. The detection of thermal neutrons is part of the anti-neutrino detection described in Sec. 3.3.3.

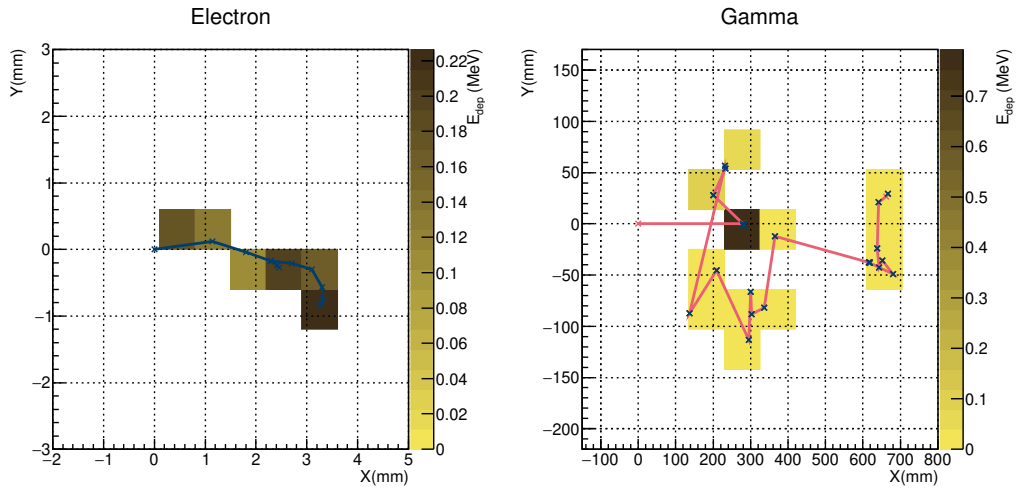

Figure 3.7: Exemplary comparison of the energy deposition pattern of electrons and gammas. The initial electron on the left side, as well as the initial gamma in the right side, were simulated with the JUNO software (Sec. 3.5) traveling in x-direction with a kinetic energy of 1 MeV. The energy deposition is shown in the colored bins, while electron tracks are marked blue and gamma tracks are marked red. One can clearly see the different energy deposition behavior. Details can be found in the text.

In dense materials in the vicinity of the detector, cosmic muons can cause the production of fast neutrons. These neutrons cause the *fast neutron background*, which is a common background in reactor electron anti-neutrino experiments. In the interaction with the detector, these fast neutrons scatter mainly on free protons of the detector material. If high energies are transferred to a proton, it is visible in the detector through its deposition of ionization energy. Through these scatterings on protons, the neutron thermalizes and might be detected as a thermal neutron.

To increase the neutron capture cross section of the LS, Gadolinium can be added, like it is done in small LS detectors [67–69, 122]. Gadolinium has a high cross section for neutron captures with an energy release of about 8 MeV in gammas. In JUNO, Gadolinium is not added in the CD, but only in the TAO detector.

3.3.3 Neutrino interactions

Neutrinos and anti-neutrinos are detected via weak force interactions. This leads to extremely small interaction cross sections, yielding small event rates. These can be distinguished in *charged-current* (CC) interactions, which are mediated by a W-boson, and *neutral-current* interactions, which are mediated by a Z-boson. CC interactions cause the absorption or creation of a charged lepton. As muons and tauons are not present in the LS medium and have masses above the considered energy scale, they can not be absorbed or produced, which leaves only electron flavor CC interactions.

Elastic scattering The commonly used *elastic scattering* (ES) interaction of neutrinos of MeV-scale energies is the one with electrons:

$$\nu_l + e^- \to \nu_l + e^- \quad \text{and} \quad \bar{\nu}_l + e^- \to \bar{\nu}_l + e^- \tag{3.6}$$

with $l \in \{e, \mu, \tau\}$. This interaction is possible in NC interactions for all flavors, and CC interactions, which are only allowed for electron-flavored neutrinos in the considered energy range. While the NC interaction cross sections are equal for all flavors, due to the exclusive electron neutrino CC interaction, the total cross section for ES is different for electron neutrinos. As this interaction channel allows the detection of electron neutrinos without a threshold, it is typically used for the detection of solar neutrinos as in [24]. The detection of a neutrino via neutrino-electron ES is done in a LS detector via the detection of the scattered electron. The cross section of $(\nu_e e^-)$-ES can be approximated by

$$\sigma_{\nu_e e^- \to \nu_e e^-} = 9.5 \cdot 10^{-45} (E_\nu \,[\text{MeV}])\,\text{cm}^2 \tag{3.7}$$

and the cross section of $(\bar{\nu}_e e^-)$-ES can be approximated by

$$\sigma_{\bar{\nu}_e e^- \to \bar{\nu}_e e^-} = 4.0 \cdot 10^{-45} (E_\nu \,[\text{MeV}])\,\text{cm}^2. \tag{3.8}$$

These approximations for these ES cross sections are taken from [131].

Besides electrons, ES on nuclei and nucleons is also possible. Despite the larger cross section, the challenge is the detection of these particles due to their high ionization quenching. Here, all neutrino flavors have the same interaction cross sections, which increases in quadratic order with the energy.

Inverse Beta Decay The *inverse beta decay* (IBD) interaction is the most common interaction to detect electron anti-neutrinos. It is a CC interaction between an electron anti-neutrino and a proton, creating a positron and a neutron:

$$\bar{\nu}_e + p \to e^+ + n. \tag{3.9}$$

Due to the higher total mass of the products of the reaction, it requires an energy threshold of $E_{\text{thr}} = 1.8\,\text{MeV}$.

Detecting an IBD event consists of the detection of two particles: the positron and the neutron. In the kinematics of the IBD reaction, the positron carries the dominant part of the energy information of the electron-neutrino as it has a much lower mass than the produced neutron. It can be measured with a total deposited energy of about

$$E_{\text{prompt}} = E_{\bar{\nu}_e} - 0.784\,\text{MeV}. \tag{3.10}$$

This allows a highly precise energy measurement of the electron anti-neutrino in IBD reactions up to a sub-percent level without measuring the neutron kinetic energy [132]. In the detection of electron anti-neutrinos with the JUNO detector, the intrinsic energy smearing of the IBD reaction due to the neutron recoil is negligible compared to the limited energy resolution of the detector. The neutron in the IBD reaction is produced with an kinetic energy of a few tens of keV. As the neutron capture cross section is small at such energies, it thermalizes with an average time of about $200\,\mu$s, before it is captured [11]. The measurement of the IBD

reaction, the coincidence in space and time of the positron signal and the neutron capture signal significantly suppresses the background. Due to the time delay between both events, the positron signal is usually called *prompt* event and the neutron capture signal is usually called *delayed* event.

The total cross section of the IBD reaction can be approximated by

$$\sigma_{\text{tot}} = 0.952 \cdot \frac{E_e p_e}{1\,\text{MeV}^2} \times 10^{-43}\,\text{cm}^2, \tag{3.11}$$

from [84]. Here, E_e and p_e are the zeroth order energy and momentum of the positron with $E_e = E_{\bar{\nu}_e} - (m_n - m_p)$. This cross section is much higher than the cross sections obtained by ES, yielding higher event rates as shown in Fig. 3.8, which compares the cross section of the IBD reaction with the cross sections of several elastic scattering processes. At an energy of about 6.5 MeV the IBD reaction has an about 100 times larger cross section than the elastic scattering reaction for electron anti-neutrinos.

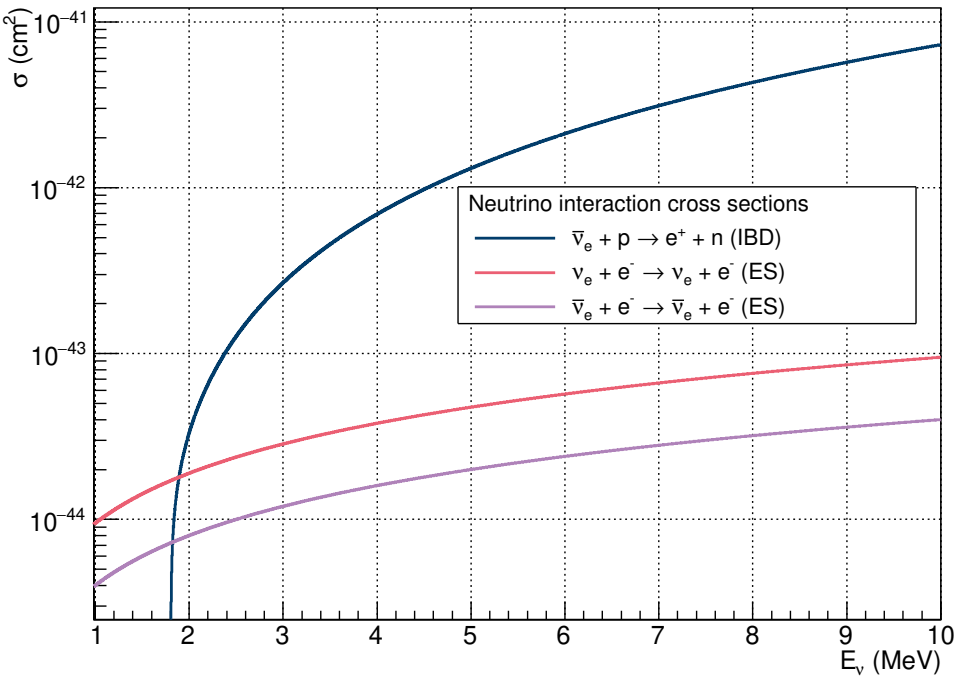

Figure 3.8: Comparison of neutrino interaction cross sections. The cross section of the IBD reaction is taken from [84] and the cross sections for ES are taken from [131].

The detection of electron anti-neutrinos via the IBD reaction has the advantages of the high detection cross section, the precise energy information, and the characteristics of the coincident signal. It is used by the JUNO experiment for the detection of reactor electron anti-neutrinos.

3.4 Calibration programme

The calibration system of the JUNO CD has three major tasks. It needs to calibrate the light non-linearity of the scintillator, the electronics non-linearity of the PMT system, and the position dependent light collection non-uniformity [133].

3.4.1 Light non-linearity

To calibrate the light non-linearity, introduced by ionization quenching and the non-linear Cherenkov light contribution, various gamma and neutron sources are used. For the precise calibration of the light output for neutrino measurements via electron ES and IBD reactions, the use of positron and electron sources would be desirable. Due to the short range of the ionization energy loss, these sources are not feasible, as they need to be contained in a source carrier capsule. Gammas have a long range, which lets them deposit most of their energy outside of this capsule, which is not the case for the primary ionization energy of electrons and positrons. The calibration source energies range from the positron annihilation gamma energy of ^{68}Ge at 511 keV, to the neutron capture gamma energy of ^{56}Fe at about 7.6 MeV. The different non-linearity curves for electrons and positrons are then obtained by converting the gamma non-linearity under the use of an appropriate model. Such a model will be presented in Sec. 4. Besides source calibration, events from cosmogenic isotope decays like the decay of ^{12}B or internal radioactivity can be used to calibrate the light non-linearity. These allow the direct calibration of the positron and electron light non-linearity. Figure 3.9 shows the spectrum of gamma sources and the corresponding usage in light non-linearity calibration from the Daya Bay experiment in [134]. The light non-linearity calibration strategy for the JUNO experiment is planned to be similar to the calibration strategy for the Daya Bay experiment.

For the MO analysis, the light non-linearity is required to be known with a relative accuracy of less than 1%.

3.4.2 Light non-uniformity

Due to the large size of the JUNO detector, the amount of detected light is dependent on the position of emission. This effect is called light non-uniformity. It is caused by the absorption, attenuation, re-emission, and scattering of light in the detector. Several systems are planned in JUNO to deploy calibration sources at different positions in the CD to precisely measure the light output dependent on the source position. These are the *Automated Calibration Unit* (ACU), the *Cable Loop System* (CLS), the *Guide Tube* (GT), and the *Remotely Operated Vehicle* (ROV).
The ACU is an automated calibration source deployment system. It can lower calibration sources through the chimney along the central axis, the Z-axis, of the detector.
The CLS system uses also a cable to lower a calibration source into the detector. However, this cable is connected to pulleys at the CD wall. Using two spools, a two-dimensional area in the detector can be reached. For this kind of calibration, the source position is determined via an ultrasonic sound system and CCD sensors inside the detector.
The GT is an acrylic tube, attached in a circular loop around the outside of the acrylic sphere,

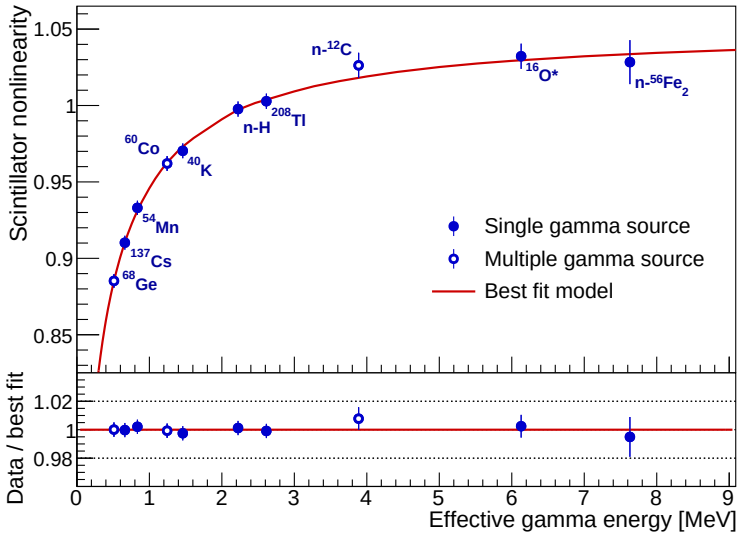

Figure 3.9: The light non-linearity source calibration of the DAYA BAY experiment. One can see the spectrum of gamma calibration sources, which will also be used in the JUNO experiment. From [134].

starting and ending at the chimney. Here, sources can be pulled through the tube via two spools with a precise positioning.
The ROV is a submarine-like source carrier, which can reach nearly any position of the detector. Also the position of the ROV can be determined via the ultrasonic sound system and CCD cameras. Due to the unstable position of the ROV, it is only known up to an accuracy of a few centimeters [133].

The expected light non-uniformity extracted from the JUNO simulation software described in Sec. 3.5 can be seen in Fig. 3.10. It can be seen that on the left side in Fig. 3.10a, that the major non-uniformity is in the radial coordinate, especially at large radii. Due to the total reflection of photons on the border between the acrylic glass and the buffer water, the amount of detected light decreases drastically. Another non-uniformity effect can be seen in the zenith angle θ, caused by the PMT placement. In Fig. 3.10b this non-uniformity in the radial distance and the zenith angle was corrected and no light non-uniformity can be observed in the azimuth angle ϕ due to the symmetry of the JUNO detector.

3.4.3 Electronics non-linearity

The electronics non-linearity of the LPMT system for energies in the reactor electron anti-neutrino range is expected to be small, as each LPMT is expected to detect only up to a few p.e. Besides its calibration via tunable LED's, the electronics non-linearity is calibrated via the usage of the SPMT system. If a LPMT is hit by many photons, its electronics non-linearity can be measured with the signal on its adjacent SPMT's.

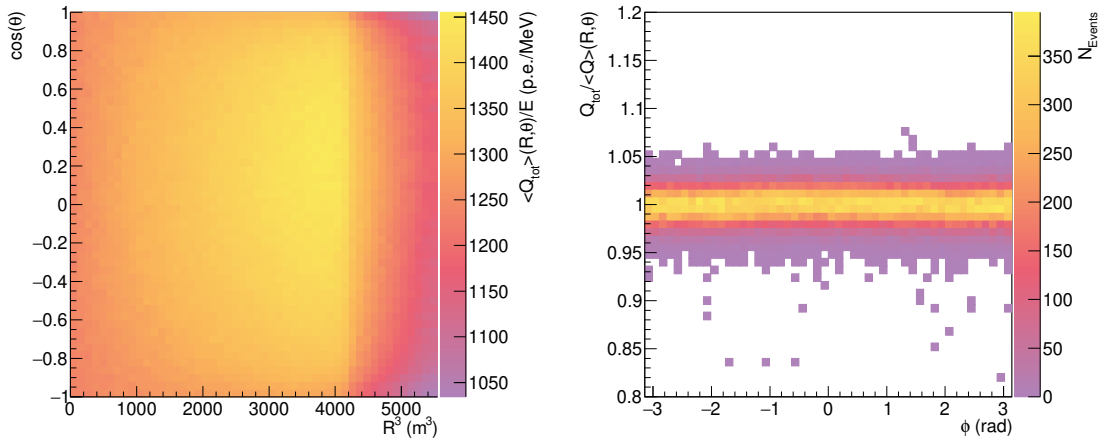

(a) (b)

Figure 3.10: Expected light non-uniformity map from the JUNO simulation software (Sec. 3.5). The left plot shows the light non-uniformity in the radius and the zenith angle created from an electron simulation in the JUNO simulation. The right figure shows that no light non-uniformity remains in the azimuth angle after correcting for the non-uniformity in the radius and zenith angle.

3.5 Simulation and event reconstruction framework

For its simulations and analysis of events, the JUNO experiment uses a software framework [19] based on the *Software for Non-collider Physics Experiments* (SNiPER) framework [18]. SNiPER is developed as a general framework to meet the requirements of both, reactor electron anti-neutrino experiments and cosmic ray experiments. It follows the idea of being a modular framework consisting of many dynamically loadable plug-ins. The Python-language is used for the implementation of a user-interface, which calls the plug-ins, which are written in C++. Furthermore, the JUNO software uses the Geant4 [135, 136] and the ROOT [137] libraries. As the development of the JUNO software is ongoing, properties of the simulation are expected to change continuously. To provide consistency, this thesis uses the same revision number 3386 from October 2018 for all its studies with the JUNO software. This revision uses the ROOT version 5.34.11 and the Geant4 version 9.4.p04.

The event treatment of the JUNO software uses a multi-staged approach, which can be divided into the simulation part and the reconstruction part, which will be summarized in the following. Both, the simulation part and the reconstruction use the same coordinate system, centered around the CD center with the Cartesian z-coordinate pointing up from the detector center to the center of the Chimney. The x- and y-coordinate are arranged perpendicular to it in arbitrary, but fixed, directions.

3.5.1 Event simulation

For the simulation part in the JUNO software, the three stages of the *physics generator*, the *detector simulation* (DetSim), and the *electronics simulation* (ElecSim) are implemented. The physics generator produces the particle list to be simulated. Besides a simple *particle gun*, which allows the placement of particles with defined properties in the JUNO detector, various generators for different studies of the JUNO experiment are implemented. These include the generators for isotope decay simulations as the β^--decay of ^{14}C as well as generators for positron-neutron pairs from an IBD reaction following the expected JUNO spectrum.

The DetSim stage simulates the interactions of particles inside the JUNO detector. It bases on the *Monte Carlo* (MC) simulation by the Geant4 framework [135]. To simulate particles in Geant4, the model of the detector and its components is implemented in detail. The so-called *Physics List* is a set of particle interactions to be simulated required from the user by the Geant4 software. The used Geant4 Physics List of electromagnetic interactions, which are used in this thesis, can be found in Appendix A. If a particle produces ionization energy, the respective optical photons from the scintillation and Cherenkov light are also propagated by the simulation. The output of the DetSim stage used by further simulation stages is a set of PMT hits, which represent p.e.'s released at the photo cathode, but not amplified by the PMT. This includes the treatment of the QE of the PMT, but not the CE. Besides that, it also calculates useful event data during the simulation, such as the event vertex, as the weighted average of energy depositions.

The purpose of the ElecSim is to simulate the behavior of the PMT readout electronics. In order to simulate the information of the multiplicity trigger and the merging of p.e. to single high-charge hits in a realistic way, all hits from the DetSim are time aligned. After merging hits, the so-called *waveforms*, the time-evolutions of the detected PMT signals, are simulated with a digitization window of 1 ns. From these, the event trigger is simulated. In the software, the event trigger is simulated as a multiplicity trigger with the default trigger condition of 800 LPMT hits in the CD in 300 ns. A positive trigger decision bundles all waveforms in a default window of 1250 ns, from -100 ns before the trigger time until 1150 ns, to an event. If needed, the ElecSim stage is also capable of mixing events from different DetSim sources with randomly arranging the corresponding hits on the time-alignment according to specified event rates. Due to the time-alignment on a single-hit level, the correspondence of ElecSim events to DetSim events is not trivial anymore, as the ElecSim redefines an event by the trigger condition instead of the definition by physical origin used in the DetSim stage. Therefore, the ability to assign ElecSim events to DetSim events is only implemented if no events are mixed and each DetSim event is processed consecutively. The output of the ElecSim stage consists of the aforementioned events, containing the PMT waveforms. This output format is designed to represent the output of the data acquisition system in JUNO.

3.5.2 Reconstruction

The reconstruction part of the JUNO software consists of two additional stages, the *calibration* stage and the *event reconstruction* stage. The ElecSim or the data acquisition system have PMT waveforms as output. In the calibration stage, the charge and time from each PMT waveform are reconstructed. The PMT waveforms contain systematic electronics noise and

its signals often shows an overshoot behavior, which can make an accurate reconstruction challenging. Different algorithms are implemented in the JUNO software for the waveform reconstruction, described in [138]. The default algorithm uses a *Fast-Fourier Transformation* (FFT) with the idea to deconvolute the high-frequent electronics noise from the low-frequent PMT signal.

The event reconstruction stage takes the reconstructed PMT charges and hit times as inputs and estimates the event properties, such as the event vertex, the total deposited energy, or the particle's identity. As default algorithm for the vertex reconstruction, an algorithm is implemented, which performs a Likelihood fit on the detected PMT hit times described in [139]. The vertex reconstruction in the JUNO CD is being studied as part of this thesis in Chapter 5.

3.6 Physics goals with the JUNO detector

The large size and unprecedented good energy resolution enable the JUNO detector to be a unique state-of-the-art tool for addressing various physics questions. Besides being designed to study the MO, the JUNO experiment is able to contribute significantly to a broad range of questions in modern neutrino and astroparticle physics, as well as in the searches for rare processes beyond the standard model of particle physics.

3.6.1 Neutrino Mass Ordering

Like shown before in Fig. 2.3, the NO and the IO can be distinguished by their different oscillation probabilities in the measurement of reactor electron anti-neutrinos. Figure 3.11 shows the expected energy spectrum of JUNO with both MO including the effect of the energy resolution of $3\%/\sqrt{E[MeV]}$.

To measure the MO, the JUNO collaboration formulated several requirements in [11]. As the JUNO detector measures reactor electron anti-neutrinos from two NPP's with several reactor cores each, the baseline variance impacts and degrades the expected difference between the MO's. To minimize this effect the baseline difference is required to be less than 500 m between two reactor cores. The JUNO site fulfills this requirement. The MO information in the JUNO experiment is extracted from the spectral shape of the prompt event from the IBD-reactions. Therefore, this shape needs to be precisely known, which introduces the challenging requirement of an energy resolution of about 3% at 1 MeV. A high uncertainty on the reconstructed neutrino energy would conceal the neutrino oscillation pattern, making the good energy resolution a crucial requirement of JUNO. It is realized by the detector design, which gives high photon statistics via the high light yield and excellent transparency of the LS and the high coverage and DE of the PMT array. Besides the energy resolution, the energy scale of the IBD measurement needs to be known with an relative accuracy of less than 1%. An inappropriate model of the non-linearity would bias the determination of the MO and needs to be addressed carefully. For that, the non-linear detector response needs to be determined from the calibration data using gamma sources. A model to describe the positron non-linear light response, which can be determined using gamma calibration data, will be presented in Chapter 4.

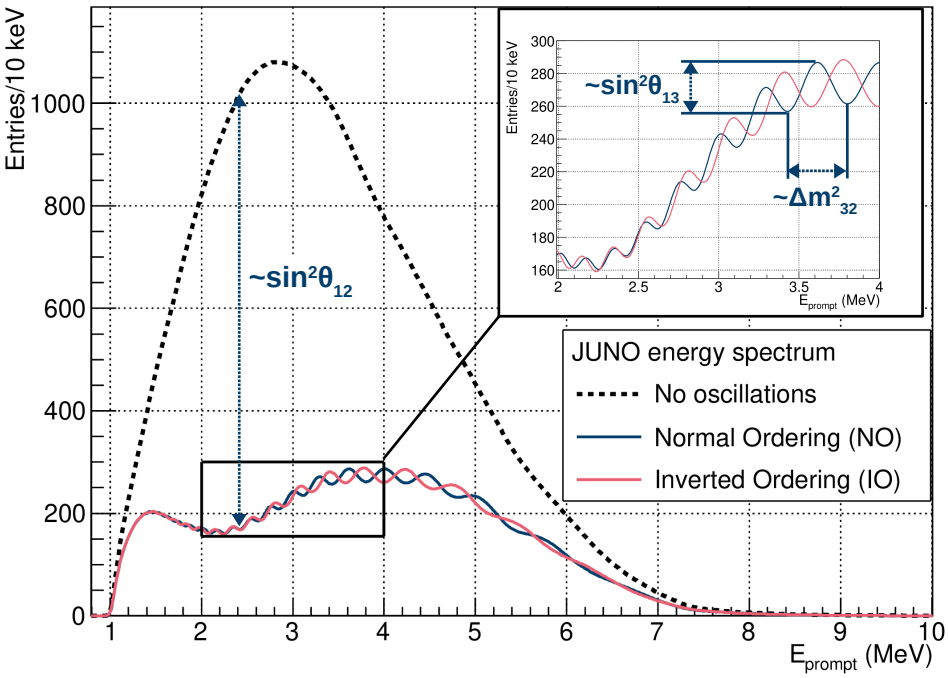

Figure 3.11: Expected energy spectra of the prompt IBD candidates in the JUNO experiment in no oscillation (dashed line) and three-neutrino oscillation models assuming normal (solid blue line) and inverted (solid red line) MO. The calculation was performed with the GNA software [20] assuming $3\%/\sqrt{E_{\text{prompt}}[\text{MeV}]}$ energy resolution and normal ordering oscillation parameters from [22]. To display the inverted ordering, only the sign of Δm^2_{32} was inverted. The insert shows in detail the energy region between 2 - 4 MeV, which is the most dependent on the MO. The features of the spectra sensitive to θ_{12} and θ_{13} mixing angles are also demonstrated.

The standard procedure planned by the JUNO collaboration to discriminate the wrong mass ordering is the application of a hypothesis test with both MO's [11]. For this test, two χ^2-fits are performed under the assumption of each MO to the measured energy spectrum of JUNO. It is expected, that the wrong MO has a higher minimized χ^2-value than the true MO. The significance of the discrimination of the wrong MO can be then obtained by the difference of both minimized χ^2-values, the $\Delta\chi^2$-discriminator

$$\Delta\chi^2_{\text{MO}} = \left|\chi^2_{\text{min}}(\text{NO}) - \chi^2_{\text{min}}(\text{IO})\right| . \tag{3.12}$$

The best estimate for the MO is the model, which yields a lower χ^2_{min} value. Using this standard procedure, the JUNO experiment expected to reach a sensitivity of $\Delta\chi^2_{\text{MO}} > 9$ in 6 years measurement time without external constraints on oscillation parameters in [11]. Due to its early publication, this analysis uses outdated assumptions. It assumes a rather high value of θ_{13}, which enlarges the difference of the MO's, as shown in Fig. 3.11. Moreover, the construction of two more reactor cores at the Taishan NPP and an additional NPP at

Huizhou is assumed. An updated study, concerning these major changes among others, is in preparation by the JUNO collaboration.

While other experiments typically aim to determine the MO using its appearance in matter effects in neutrino oscillations, the JUNO experiment uses the effect of the MO on vacuum oscillations to determine it. Due to the different approach, a combined analysis between experiments of both types drastically increases the sensitivity due to synergy effects. This was demonstrated for the combination of the JUNO experiment with the PINGU experiment in [140].

Backgrounds of the MO analysis

Due to its large overburden, the coincidence requirement in the IBD event selection, and the selection of a fiducial volume, the background contribution in JUNO is largely suppressed. Nevertheless, various background sources are barely distinguishable from IBD events as they mimic the coincidence characteristics of an IBD event.

Accidental background The term *accidental background* is used to describe uncorrelated events, which fall randomly together to form a random coincidence. Accidental background can be caused by all kinds of single sources. Due to the high rates, it is typically caused by gamma radiation from the surrounding rock or the detector material, as well as internal radioactivity from the scintillator.

Pile-up events If a positive trigger condition is stated in the data acquisition process of JUNO, a time window around the trigger time is opened. All PMT hits, which fall into this time window are then collected into one data acquisition event structure. If two physical events fall closely together in time, they are both read out in the same data acquisition event. This random coincidence makes it challenging to reconstruct the information from each physical event. Contrary to other background sources, pile-up events are not visible as another species in the spectrum, but distort the spectra of the other species. As the MO measurement of JUNO extracts the information from the spectral shape measurement, this background can crucially degrade its sensitivity. The rate of most background sources is not high enough to yield a significant amount of pile-up events. As shown before in Sec. 3.2.1, the large amount of JUNO LS is expected to contain high absolute amounts of ^{14}C with a expected high total rate of about 40 kHz. While single ^{14}C-decays can be easily discriminated by a trigger threshold from IBD events, the high rate can cause the pile-up of IBD events and ^{14}C-decays. The rate of pile-up depends on the length of the data acquisition time window, which is to be decided upon by the JUNO collaboration. In the JUNO software, a time window of 1250 ns is used. Under that assumption, the ratio of affected events can be roughly estimated with

$$R_{14\mathrm{C}} \cdot T_{\mathrm{DAQ}} \approx 5\%, \tag{3.13}$$

with the total ^{14}C decay rate $R_{14\mathrm{C}}$ and the data acquisition time window T_{DAQ}. To reduce the distortion of the measured reactor electron anti-neutrino spectrum, algorithms are needed, which identify pile-up events. A strategy and performance for this will be presented in Chapter 6 as part of this thesis.

Cosmogenic isotopes Cosmic muons, which interact in the detector can be identified due to their large energy deposition and are therefore no background for the MO measurement. However, besides their ionization energy deposition, these muons can interact with carbon atoms of the LS to create a wide range of so-called *cosmogenic* isotopes from ^{3}He to ^{18}N and free neutrons [97]. These isotopes mostly decay in a close range and time to the initial muon. Therefore, most of this background contribution can be largely suppressed by a time and position cut around the muon track, which requires a precise muon track reconstruction. The more challenging cosmogenic isotopes are ^{9}Li and ^{8}He, which undergo a (β^{-}, n)-decay. In a (β^{-}, n)-decay, the isotope emits an electron, shortly followed by a neutron. The electron spectrum of these decays overlays completely with the IBD-spectrum from reactor electron anti-neutrinos, making this background barely distinguishable from the signal. Due to the long half-lifes of ^{9}Li and ^{8}He of 0.178 s and 0.119 s, respectively, the discrimination of these decays by a time cut would result in a large loss of signal events in JUNO. A novel approach to discriminate this background is the particle identification of electrons and positrons. Due to the similar LS time spectrum of electrons and positrons, this approach is challenging, but preliminary studies show discrimination power [141].

Fast neutron background The fast neutron background originates from cosmic muons as well. Fast neutrons are created in dense material around the detector by interactions of cosmic muons with the material. Fast neutrons can scatter on free protons, which then ionize the scintillator, as well as being captured on free protons to emit a gamma of about 2.2 MeV. For this kind of background, the prompt event can be mimicked by the ionization light from a proton and the delayed event can be mimicked by a neutron capture.

Geo-neutrinos As they are detected in the same interaction channel (see Sec. 2.2), geo-neutrinos can not be distinguished from reactor electron anti-neutrinos in the IBD energy spectrum. Due to their endpoint energy of about 2.6 MeV, they only affect the low energy end of the reactor electron anti-neutrino spectrum.

(α, n) background The (α, n) background stems from internal α-radiation from the Uranium, Thorium, and Polonium contamination in the LS. These α-particles can interact with ^{13}C atoms in the scintillator, which can cause the production of a fast neutron and a gamma from the de-excitation of the created ^{16}O. If the neutron is fast enough, there is a de-excitation gamma, the $^{13}\mathrm{C}(\alpha, n)^{16}\mathrm{O}$-reaction can cause a correlated background.

Event selection The selection of IBD events presented in [11] uses the following simple cuts to discriminate background:

- Fiducial volume cut: $R < 17\,\mathrm{m}$
- Prompt event energy window: $0.7\,\mathrm{MeV} < E_{\mathrm{prompt}} < 12\,\mathrm{MeV}$
- Delayed event energy window: $1.9\,\mathrm{MeV} < E_{\mathrm{prompt}} < 2.5\,\mathrm{MeV}$
- Time coincidence between prompt and delayed event: $\Delta T < 1.0\,\mathrm{ms}$

- Vertex coincidence between prompt and delayed: distance $< 1.5\,\mathrm{m}$

Moreover, muon veto cuts are applied. If the muon was not trackable, the whole CD is vetoed for 1.2 s to reduce cosmic background. Also if the muon was detected by the WP measurement, the whole CD is vetoed for a time of 1.5 ms. As the vetoing of the whole detector on the second scale at a muon rate of about 3.5 Hz reduces drastically the efficiency of the event selection, for trackable muons a local veto cut is applied. This local veto includes all events within a radius of 3 m around the muon track within a time of 1.2 s after the muon signal.

This event selection of JUNO is expected to have a signal efficiency of 73%. From the assumed 83 IBD events per day including the Taishan-3 and Taishan-4 reactor, about 60 IBD events per day remain after the application of all cuts. The dominant contributions are here the selection of the fiducial volume with 91.8% efficiency and the muon veto cuts with 83% efficiency. After the application of all cuts, only 3.8 background events per day are expected to remain in the data selection.

3.6.2 Extended physics programme

Besides the determination of the MO, the JUNO experiment aims to address a broad spectrum of physics questions. Due to its unprecedented detector design, it is expected to be able to make crucial contributions to many of the presented physics topics. This section should give an overview of selected topics from the physics programme, comprehensively presented in [11].

Precision measurement of oscillation parameters

As the first experiment measuring the fast Δm^2_{31}, and Δm^2_{32} neutrino oscillations simultaneously with the slow Δm^2_{21} neutrino oscillations JUNO has the ability to improve the current knowledge on the oscillation parameters significantly. This measurement is closely related to the determination of the MO, as these parameters will be extracted from the same fit. The oscillation parameters $|\Delta m^2_{31}|$, Δm^2_{21} and $\sin^2\theta_{12}$ are currently known to a precision of 1.2%, 2.8%, and 4.0%, respectively [62]. JUNO aims to measure these parameters to a precision of 0.5%, 0.6%, and 0.7%, respectively, using the measured reactor electron anti-neutrino spectrum.

Solar neutrinos

JUNO aims to measure electron neutrinos from ^{7}Be and ^{8}B in the pp Solar Fusion Cycle. ^{7}Be neutrinos are mono-energetic at 0.862 MeV and ^{8}B neutrinos have an energy from 0 up to 14.6 MeV. These neutrinos are detected via ES on electrons. To measure ^{7}Be neutrinos a low sub-MeV detection threshold and a high radio-purity is needed. For ^{8}B neutrinos JUNO needs to effectively suppress the background from ^{10}C decays. The measurement of these neutrinos by JUNO would help in solving the solar metallicity problem and it would provide more information on the matter effects of neutrino oscillations.

Geo-neutrinos

Besides being a background to the measurement of reactor electron anti-neutrinos, geo-neutrinos are also part of the physics programme of JUNO. Due to its large size, the JUNO experiment is expected to measure about 400 geo-neutrinos per year, which is by far more than the current leading experiments KamLAND [142] and Borexino [25] detected so far. Nevertheless, the geo-neutrino measurement by JUNO suffers from the large reactor electron anti-neutrino signal. The prediction of the geo-neutrino signal in JUNO was performed in a dedicated study of the local crust around the position of the JUNO detector [143].

Supernova burst neutrinos

JUNO will be able to measure the released neutrinos from a SN burst mainly in the IBD reaction channel among others. Due to the large dimensions of the JUNO detector, it is expected to measure a SN signal with high event statistics. For a SN in the distance of 10 kpc, an event rate of 5000 IBD events in the first 10 s is expected. Moreover, 2000 neutrino-proton ES events and about 300 neutrino-electron ES events are expected. For the readout of such a high event rate, a specialized read-out buffer is planned in the data acquisition system of the JUNO detector. To take part in the supernova multi-messenger astronomy, JUNO is part of the Super-Nova Early Warning System (SNEWS) [40].

The observation of the time-development of the neutrino signal of a supernova together with the observations from other experiments will lead to a better understanding of the respective supernova model. It will also give additional information on the MO discrimination.

Besides the accurate optical measurement, the neutrino emission will be a handle to locate the SN. In LS detectors, such as JUNO, the direction of electron anti-neutrinos, which undergo IBD reactions, can be estimated by the difference between the vertex of the delayed event and the vertex of the prompt event [144]. Due to the thermal movement of the neutron from the IBD interaction position and the large spread of the gamma energy deposition, this directionality measurement is not possible on a single event basis and requires large event statistics and a precise vertex reconstruction. This directional information becomes especially important, if the SN is hidden behind dense gas or dust clouds, which make the optical measurement impossible. A possible resolution of such a directionality measurement for low energy events will be presented in Sec. 5.5.2.

DSNB neutrinos

Related to SN burst neutrinos, also DSNB neutrinos are part of the physics programme of JUNO. Different to SN burst neutrinos, which are expected to appear in a very high rate for a short time, DSNB neutrinos are expected to be measured as a continuous flux with a very low rate. Also DSNB neutrinos are measured via the IBD detection channel. Due to this low signal rate, the background rate is relatively high. At low energies the high reactor electron anti-neutrino flux is limiting the measurement, while at high energies, the atmospheric neutrino CC interactions are dominating the spectrum. Depending on the DSNB rate and spectral shape, a small window of about 13 MeV to 18 MeV measured prompt energy is left to search for the DSNB flux with fast neutrons as major background. Under the assumption

of typical DSNB parameters, JUNO is expected to be able to measure a DSNB signal with about $3\,\sigma$ significance. A non-detection would strongly improve current limits on the DSNB parameter space.

Indirect dark matter detection

Dark matter is a hypothetical type of non-baryonic matter, primarily introduced to explain various gravitational effects in galaxies [145], such as the rotation curve of a galaxy or gravitational lensing effects. The existence of dark matter is a To be able to explain the effects dark matter is assumed to be highly abundant in the universe, accounting for about 85% of all matter. To explain these effects, dark matter is assumed to be highly abundant in the universe, accounting for about 85% of all matter in the universe. The searches for dark matter utilize three different detection channels: the direct detection via nuclei recoils, the indirect detection via dark matter self-annihilation, and the production of dark matter in collider experiments. JUNO can contribute to the indirect dark matter searches with the measurement of the dark matter self-annihilation channel into neutrinos:

$$\chi + \chi \rightarrow \nu + \bar{\nu}, \tag{3.14}$$

with χ denoting the dark matter particle. This reaction would produce a neutrino flux with an energy of the mass-equivalent of the dark matter particle. Assuming a dark matter particle mass between 10 MeV and 100 MeV, the backgrounds for the dark matter detection are DSNB neutrinos, fast neutrons, and atmospheric neutrinos.

Proton decay

Besides neutrino physics, JUNO is able to contribute to the search for proton decays due to its large mass and proton number. The most stringent limits on the proton life time are published by the Super-Kamiokande collaboration in [146]. However, the Super-Kamiokande experiment focuses on the proton decay channel into pions. Depending on the model for the proton decay, the channel $p \rightarrow K^+ + \nu$ might be the dominant channel. In JUNO up to three signals are expected for each of these decays. First, the kaon deposits kinetic energy in the scintillator and produces scintillation light. The kaon decays in about 12 ns into a positive charged muon, which decays into a positron after $2.2\,\mu$s. Also the muon and the positron might deposit energy in the detector and cause a visible signal. This channel benefits from the detection of the Kaon which is under the Cherenkov threshold in water and can therefore not be measured by the Super-Kamiokande experiment. As JUNO uses liquid scintillator as detection medium it has a large advantage above water Cherenkov detectors in this detection channel.

Atmospheric neutrinos

Although not being designed for the high energy spectrum of atmospheric neutrinos, JUNO can measure the atmospheric neutrino spectrum with a good energy resolution. With the measurement of atmospheric neutrinos, JUNO aims to address the questions of the MO, the octant degeneracy of θ_{23}, and the CP violation phase δ in Neutrino Oscillations through the

MSW-effect. As Earth is transparent for neutrinos of the considered GeV energy range, JUNO can measure atmospheric neutrinos with a broad range of baselines from the whole atmosphere. The baseline of an atmospheric neutrino is described by the zenith angle of its direction, which can be resolved via tracking algorithms of the secondary particles. For the analysis presented in [11], the measurement of atmospheric neutrinos can reach about 0.9 σ to rule out the wrong MO. This result depends on the reached direction resolution, the energy resolution, and the ability to distinguish neutrino flavors due to their different CC interactions. This measurement is complementary to the measurement of the MO with reactor electron anti-neutrinos and can therefore improve the overall sensitivity of JUNO to the MO.

Part II

Non-linearity studies and event reconstruction for the Neutrino Mass Ordering measurement of the JUNO experiment

Chapter 4

Model of the positron non-linearity

Among the most challenging requirements for the MO analysis are those on the energy scale and resolution. It is required to reach a relative uncertainty on the energy scale of less than 1% and an energy resolution better than 3% at 1 MeV [11]. The light emission in a liquid scintillator is not linear with the deposited energy of particles and depends on the detected initial particle type. As inappropriate modeling of the non-linearity biases the determination of the MO, it is of imminent importance to address this topic carefully. As the JUNO experiment will use gamma sources for the energy non-linearity calibration, it is important to develop methods how to derive a non-linearity model for electrons and positrons based on the gamma calibration data.

This chapter focuses on the description of the energy non-linearity in the scintillation medium. It is a topic of general interest in organic scintillator physics with numerous publications on it [134, 147–149]. The non-linearity will be determined from the ratio of the visible energy over deposited energy. The term *visible energy* is used here to describe the expected amount of detectable light produced in the scintillation medium in the detector.

The part 4.1 deals with the light non-linearity in the measurement of electrons and of the kinetic energy loss for positrons (thus excluding the annihilation part) due to the ionization quenching (Sec. 4.1.1) and Cherenkov light production (Sec. 4.1.2). Since electrons directly produce scintillation photons through ionization, their model is simpler than for gammas or positrons, which also produce other secondary particles. The non-linearity model is based on Birks' empirical formula [123]. Section 4.2 describes the conversion of the electron non-linearity model to the more complex non-linearity model for gammas and positrons including the annihilation. Gammas loose their energy in the scintillation medium under the production of several secondary electrons responsible for the emission of scintillation light. An algorithm is presented to generate the energy distributions of the secondary electrons, as discussed in Sec. 4.2.1. These are then used to calculate the full non-linearity of the gammas by adding up the contributions from each secondary electron. This algorithm is validated and compared to the JUNO Geant4 simulation (Sec. 3.5) in Sec. 4.2.2. It is shown, that it reproduces the results from the Geant4 simulation and has computational benefits due to its easy use and fast calculation (Sec. 4.2.3). The resulting non-linearity model for gammas is then presented in Sec. 4.2.4. As positrons produce scintillation light directly in the deposition of their kinetic energy as well as through the annihilation producing two gammas as secondary particles, their

non-linearity model can be constructed through the combination of these. This is shown in Sec. 4.3. In part 4.3.1, the positron non-linearity is evaluated for the case of positron annihilation at rest into two photons. To evaluate the accuracy of this simplification, the resulting non-linearity is compared to the full JUNO Geant4 simulation with its more comprehensive physics description (Sec. 4.3.2). In Sec. 4.4, it is discussed how this model can be used and validated in the calibration programme of JUNO.

The results from this chapter are submitted for publication as a peer-reviewed article together with the co-authors Yaping Cheng and Livia Ludhova. For this publication and the results of this chapter, the technical work was done entirely by myself. The discussed interpretations and analysis strategies follow discussions with Livia Ludhova, who supervised the work on this thesis, and Yaping Cheng, who had also past contributions on the discussed topics [150]. At the time of the submission of this thesis, the review by the Journal *Journal of Instrumentation* has not yet taken place and the publication of the article as a peer-reviewed article is pending. The pre-print, which was used for this submission, can be found at [151].

4.1 Liquid scintillator non-linearity

4.1.1 Ionization quenching of scintillation light

The total amount of the scintillation light $\langle L(E_{\text{kin}})\rangle$ from the deposition of the kinetic energy E_{kin} of a charged particle in the LS can be expressed as

$$\langle L(E_{\text{kin}})\rangle = \int_{\text{path}} \left\langle \frac{\mathrm{d}L}{\mathrm{d}X} \right\rangle \mathrm{d}X, \tag{4.1}$$

with the use of the unit depth, which is the density weighted unit path length: $\mathrm{d}X = \rho \mathrm{d}x$. Under the use of Birks' formula (Eq. 3.3) and $\mathrm{d}X = \langle \mathrm{d}E/\mathrm{d}X\rangle^{-1}\,\mathrm{d}E$, this equation can be then reformulated as

$$\langle L(E_{\text{kin}})\rangle = L_0 \int_0^{E_{\text{kin}}} \frac{1}{1 + kB\left\langle \frac{\mathrm{d}E}{\mathrm{d}X}\right\rangle (E')} \mathrm{d}E'. \tag{4.2}$$

In the following, the contribution to the *visible energy* E_{vis} from scintillation light will be determined from this equation. The *non-linearity* of the energy scale will be then defined as the dependence of the ratio $E_{\text{vis}}/E_{\text{dep}}$ on the particle's kinetic energy E_{kin}. In the case of electrons and gammas, the particle's deposited energy E_{dep} is equal to its kinetic energy.

To describe the suppression of the light emission in the LS, one needs to know the energy dependent energy loss per unit depth in the scintillation medium. For electrons, it is described by the Møller model, while the Bhabha model describes the energy loss of positrons [22]. The Møller model can be written as

$$\left\langle -\frac{dE}{dX} \right\rangle = \frac{1}{2} K \frac{Z}{A} \frac{1}{\beta^2} \times \left[\ln \frac{m_e c^2 \beta^2 \gamma^2 m_e c^2 (\gamma - 1)}{2I^2} + (1 - \beta^2) - \frac{2\gamma - 1}{\gamma^2} \ln 2 + \frac{1}{8} \left(\frac{\gamma - 1}{\gamma} \right)^2 - \delta(E) \right] \tag{4.3}$$

while the Bhabha model can be written as

$$\left\langle -\frac{dE}{dX} \right\rangle = \frac{1}{2} K \frac{Z}{A} \frac{1}{\beta^2} \times \left[\ln \frac{m_e c^2 \beta^2 \gamma^2 m_e c^2 (\gamma - 1)}{2I^2} + 2 \ln 2 - \frac{\beta^2}{12} \left(23 + \frac{14}{\gamma + 1} + \frac{10}{(\gamma + 1)^2} + \frac{4}{(\gamma + 1)^3} \right) - \delta(E) \right]. \tag{4.4}$$

To apply the energy loss equations for the JUNO scintillator, one needs to find appropriate values for the density correction $\delta(E)$, the mean excitation energy I, and for the ratio of the atomic number to the atomic mass number Z/A. The global coefficient $K = 4\pi N_A r_e^2 m_e c^2 = 0.307075\,\mathrm{MeV\,mol^{-1}\,cm^2}$ with the Avogadro constant N_A and classical electron radius r_e summarizes natural constants. As LAB is by far the dominant component of the LS mixture, the following calculations assume LAB as the only component of the scintillator with a chemical composition of $C_{17}H_{29}$. The parameter Z/A is approximated by $\langle Z \rangle / \langle A \rangle$ by taking the atom-abundancy weighted mean of the LAB-molecule, as it is suggested in [22]. The value is calculated to be $Z/A \approx \langle Z \rangle / \langle A \rangle = 0.087\,\frac{\mathrm{mol}}{\mathrm{g}}$. The mean excitation energy $I = 58.9\,\mathrm{eV}$ is taken from the output of the ESTAR-tool [152].

The left plot in Fig. 4.1 shows a comparison between the energy losses $\langle \mathrm{d}E/\mathrm{d}X \rangle$ calculated using the Møller and the Bhabha models, and evaluated via the ESTAR-tool. The same density correction term was applied in all three cases based on the evaluation in [153]. Then, using the Eq. 4.2, one can obtain the respective $E_{\mathrm{vis}}/E_{\mathrm{kin}} = f(E_{\mathrm{kin}})$ non-linearity curves. The integration was evaluated numerically under the usage of the Gauss-Legendre method implemented in the ROOT framework [137]. A typical value of $k_B = 0.01\,\mathrm{cm^2/MeV/g}$ was used here and will be used in the later evaluations in this chapter. The exact value for the JUNO scintillator was not conclusively measured so far. For the better visibility of the quenching impact, the scintillation light yield normalization is set to $L_0 = 1$. With this normalization, the visible energy from scintillation light only is equal to the deposited energy under the assumption of no quenching.

The resulting three non-linearity curves, shown in the right plot of Fig. 4.1, are similar for all three different $\langle \mathrm{d}E/\mathrm{d}X \rangle$ energy loss models. It should be noted, that the validity of the chosen quenching model needs to be evaluated based on the future calibration data.

4.1.2 Cherenkov light

Additionally to scintillation light, also Cherenkov light is produced by charged particles in the scintillation medium. As it is usually created at small photon wavelengths [124], it is mostly absorbed and re-emitted by the scintillation medium [125]. Due to this conversion, it can not be separated easily from the scintillation light and must be included in the non-linearity model. The amount of Cherenkov light depends on the kinetic energy and the mass of the particle. Therefore, the same amount of Cherenkov light is assumed for electrons and positrons.

To model the amount of detected Cherenkov photons in the detector, a simple empirical expression is applied, which was used in the solar-neutrino analysis of the Borexino experiment

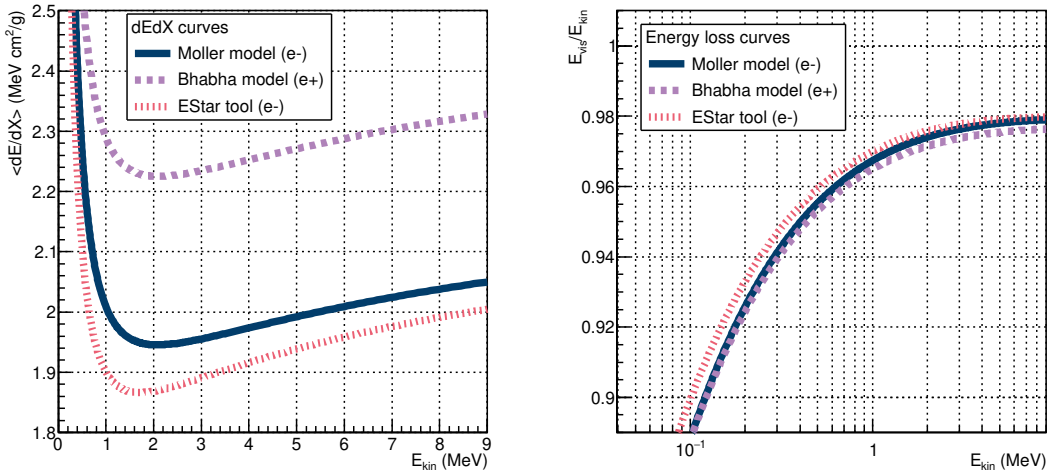

Figure 4.1: Comparison between the three different energy loss models (Møller, Bhabha, and ESTAR-tool) as a function of the kinetic energy. Left: The energy loss per unit depth $\langle \mathrm{d}E/\mathrm{d}X \rangle$. Right: The respective non-linearity curves $E_{\mathrm{vis}}/E_{\mathrm{kin}}$, obtained via integration of the Birks' formula (Eq. 4.2) with $kB = 0.01\,\mathrm{cm}^2/\mathrm{MeV/g}$ and a light yield normalization of $L_0 = 1$.

using Pseudocumene-based LS [154]:

$$\frac{N_{\mathrm{Cherenkov}}(E_{\mathrm{kin}})}{E_{\mathrm{kin}}} = \left(\sum_{n=0}^{3} A_n x^n \right) \cdot \left(\frac{1}{E_{\mathrm{kin}}} + A_4 \right) \tag{4.5}$$

with

$$x = \ln\left(1 + \frac{E_{\mathrm{kin}}}{E_0}\right).$$

To evaluate the model of detected Cherenkov light and to estimate the parameters A_i, Eq. 4.5 is fitted to the detected number of Cherenkov photons based on the JUNO Geant4 simulation for electrons. As the parameters of Eq. 4.5 were found to be highly correlated in the fit, the parameters A_0 and A_1 were fixed to 0 to reduce these correlations. The best fit values for the parameters A_i with $i \in \{2, 3, 4\}$, which are shown with the fit on Fig. 4.2, are used in the following analysis. The Cherenkov threshold was also estimated from the simulation output to be $E_0 = 0.2\,\mathrm{MeV}$.

While the amount of Cherenkov light can be fully determined from Eq. 4.5 after the determination of its parameters, the normalization of scintillation light and therefore the relative contribution of Cherenkov light still needs to be determined. This is also taken from the JUNO Geant4 simulation. A simulation of electrons without quenching at 1 MeV yields a ratio of

$$\frac{L_{\mathrm{Cherenkov}}}{L_{\mathrm{Scintillation}}}(1\,\mathrm{MeV}) = \frac{50.39 \pm 0.07}{1217.6 \pm 0.2} = (4.142 \pm 0.006)\%,$$

with a pure statistical uncertainty originating from the amount of simulated data. This number is used here to fix the relative contribution of Cherenkov light to the visible energy at 1 MeV

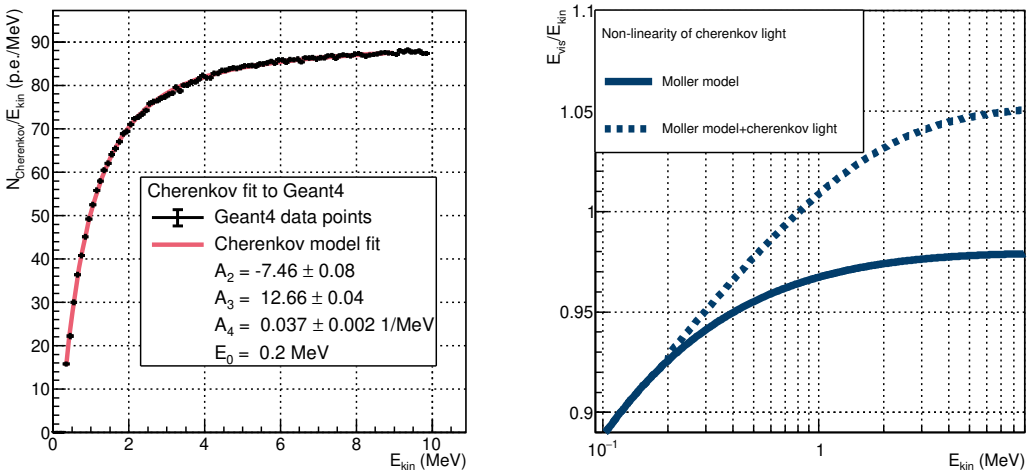

Figure 4.2: Left: Number of detected Cherenkov photons per E_{kin} as a function of kinetic energy based on the JUNO Geant4 simulation of electrons (black points). The solid red line shows the fit of Eq. 4.5 to the Monte Carlo data points. Right: Effect of the Cherenkov contribution to the LS non-linearity $E_{\text{vis}}/E_{\text{kin}}$, as a function of kinetic energy, using the Møller model for the ionization loss calculation. The solid line shows the case with only the scintillation light, while the dashed line the case including also the Cherenkov light.

kinetic energy. Due to this choice of normalization, the non-linearity ratio $E_{\text{vis}}/E_{\text{kin}}$ can be larger than 1, if Cherenkov light is included in the following.

The JUNO Geant4 simulation is not assumed here to yield the amount of Cherenkov light with a high precision. However, it is used here to obtain parameter values of Eq. 4.5 and a normalization. These values can be seen illustrative here, as they need to be evaluated in the calibration programme.

4.2 Algorithmic calculation of the gamma non-linearity

4.2.1 Algorithm for calculating secondary electron energies

To develop a non-linearity model for positrons based on the electron non-linearity model, one needs to combine the non-linearity model of the positron itself and the non-linearity model of the annihilation gammas. The annihilation gammas interact with electrons of the scintillator with several different processes creating secondary electrons. To describe the energy loss of gammas, an algorithm was developed to obtain the energies of the secondary electrons, which are responsible for the production of scintillation light. In the regime of gamma energies below $E_\gamma = 2 \cdot m_e c^2$, these are the photoelectric effect, Rayleigh-scattering, and Compton-scattering [22]. Above $E_\gamma = 2 \cdot m_e c^2$, the gamma can also produce an electron-positron pair in an interaction with a nucleus or an electron.

To simulate the behavior of the initial gamma, the scattering process is determined first. This was done by using the relative contribution of the process to the total interaction cross section

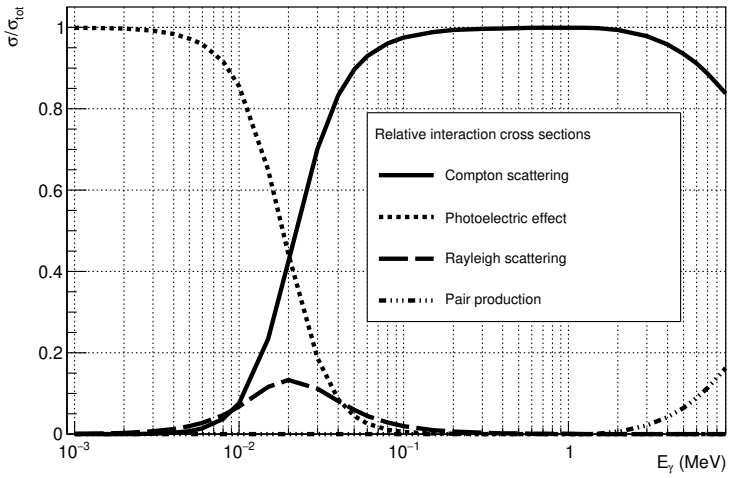

Figure 4.3: Relative cross sections of gamma scattering processes in LAB from [129].

as the probability to undergo that process. The relative cross sections are shown in Fig. 4.3. These provide the probabilities of the gamma to interact with the respective process in the medium. For higher energies above $E = 2 \cdot m_e c^2$, pure Compton-scattering was assumed as the cross section for electron-positron pair production is small compared to the cross section for Compton scattering for typical energies of a few MeV in JUNO [129].

In the case of Rayleigh-scattering, the gamma does not loose energy and is just re-emitted in a different direction. As the simulation does not consider the spatial behavior of the gammas but only the energy, the process of Rayleigh scattering is not considered.

In the case of the photoelectric effect, the full energy of the gamma is transferred to the electron of the scintillation medium. The gamma gets absorbed and the algorithm is stopped, if the photoelectric effect occurs.

Compton-scattering is the dominant process for initial gammas with an energy above ≈20 keV in LAB. For the process of Compton-scattering on an electron at rest, the distribution of scattering angles is calculated first. The distribution of scattering angles is determined via the Klein-Nishina differential cross section [155]:

$$\frac{\mathrm{d}\sigma}{\mathrm{d}\Omega} = \frac{\mathrm{d}\sigma}{\mathrm{d}\phi\,\mathrm{d}\cos\theta} = \frac{\alpha^2}{2m_e^2}\left(\frac{E'_\gamma}{E_\gamma}\right)\left[\frac{E'_\gamma}{E_\gamma} + \frac{E_\gamma}{E'_\gamma} - \sin^2\theta\right]. \tag{4.6}$$

In this formula, $\alpha \approx 1/137$ is the electromagnetic fine structure constant, E_γ is the gamma energy before scattering, E'_γ is the gamma energy after scattering, and θ is the scattering angle. The energy loss ratio follows

$$\frac{E'_\gamma}{E_\gamma} = \frac{1}{1 + \frac{E_\gamma}{m_e}(1 - \cos\theta)}. \tag{4.7}$$

Since the total cross section in an scattering angle interval is proportional to the scattering probability, the normalized Klein-Nishina differential cross section is the probability density function (PDF) for the angular distribution shown in Fig. 4.4.

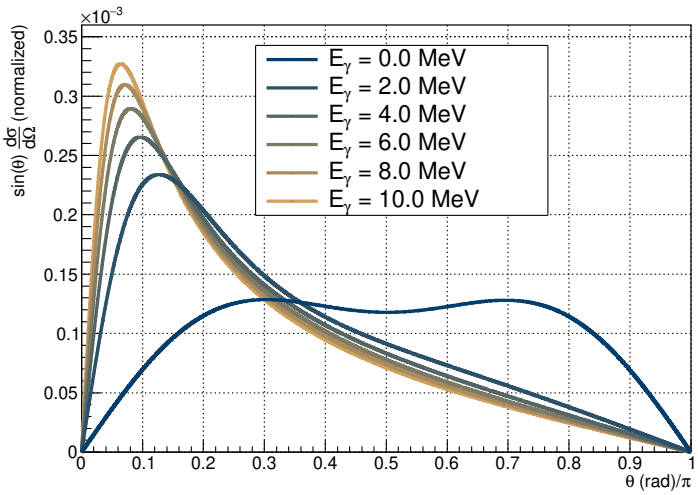

Figure 4.4: The evaluation of the Klein-Nishina cross section Eq. 4.6. As it is used as a probability distribution, it is normalized to 1 and weighted with $\sin(\theta)$ as the integration is evaluated over $\mathrm{d}\cos\theta$.

The energy of the gamma after scattering is obtained from Eq. 4.7 by inserting a random angle following the angular distribution shown in Fig. 4.4. The kinetic energy of the scattered electron follows energy conservation:

$$E'_{\mathrm{e,kin}} = E_\gamma - E'_\gamma. \tag{4.8}$$

After each Compton scattering the calculation is repeated until the gamma is absorbed via the photoelectric effect or has an energy of less than $E_{\mathrm{min}} = 250\,\mathrm{eV}$. This minimal energy was chosen to be the same as the default one used by the Geant4-software for electromagnetic processes [135].

4.2.2 Validation and cross check

The algorithm for calculating the distributions and energies of secondary electrons, as it was presented in the previous Section, is validated against the JUNO Geant4 simulation. Gammas with $E = m_e c^2 = 511\,\mathrm{keV}$ energy simulated in the detector center are chosen, in order to avoid border effects at the acrylic vessel. Figure 4.5 compares the distribution of the number of secondary electrons and their full energy spectrum for the case of the algorithm from this thesis (solid blue line) and the JUNO Geant4 simulation (solid red line). The complete physics list of the JUNO Geant simulation can be found in Appendix A. For a better comparison, the histograms obtained with the algorithm from this thesis were scaled down to match the amount of data in the Geant4 simulation. In general, the number of secondary electrons is not a reliable number for comparison, as it can depend on the so called *production cuts*, *i.e.* the lower energy cut, at which the tracking of the mother particle is stopped [136]. As the lower energy limit here is given by the dominance of the photoelectric absorption at low energies, these production cuts are not reached and the number of secondary electrons is a reliable quantity for comparison. As one can see in the left part of Fig. 4.5, the distribution of the number of

secondary electrons shows a reasonable agreement with only slight differences of the mean and the standard deviation. The right part of Fig. 4.5 demonstrates the excellent agreement of the overall energy spectrum of the secondary electrons. This comparison approves the reliability of the presented algorithm. Here, only the comparison of the full secondary electron spectrum is shown. In Appendix B, the comparison of the secondary electron spectrum of each electron generation up to the 24th generation is shown.

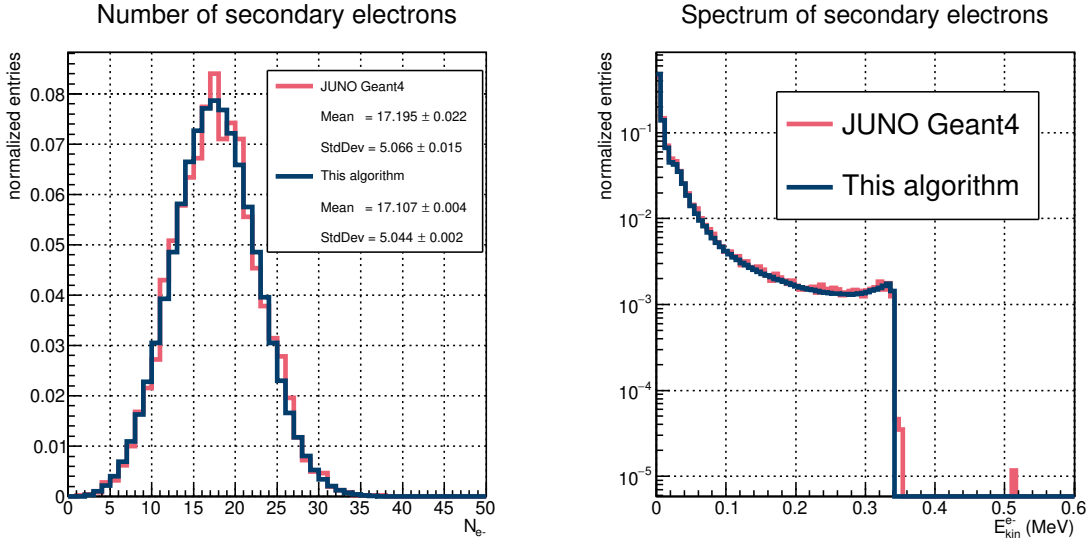

Figure 4.5: Comparison of the presented algorithm for secondary electrons (Sec. 4.2.1, solid blue line) with the JUNO Geant4 simulation (Sec. 3.5) (solid red line) for $E_\gamma = 511\,\text{keV}$. The left side shows the number of secondary electrons and the right side shows their overall energy spectrum.

4.2.3 Computational benefits

In the process of calculating the non-linearity from gammas or positrons (see Sec. 4.3) using this algorithm, the production of a representative sample of secondary electrons, dominates the computing time. To estimate the gain in computation time of this algorithm with respect to the evaluation by Geant4, both algorithms were run for different initial gamma energies and number of generated events. All of these runs were executed on the same machine by an AMD Opteron$^{\text{TM}}$ Processor 6238. In the JUNO Geant4-framework, the computation time is usually dominated by the propagation of optical photons, when the default settings are used. The production of these optical photons has been disabled. For the computation time it is assumed, that each algorithm needs a certain amount of start-up time T_0 for its setup before each event needs the same time T_{event} on average to be processed. The total computation time is expected to follow

$$T_{\text{comp}} = T_0 + T_{\text{event}} \cdot N, \tag{4.9}$$

with N being the number of processed events. For both algorithms, the computation times for the energies of 0.1 MeV, 3.3 MeV, 6.7 MeV, and 10.0 MeV, as well as for the event numbers of 1, 500, 1000, 1500, 2000, and 2500 events were evaluated. The parameters T_0 and T_{event}

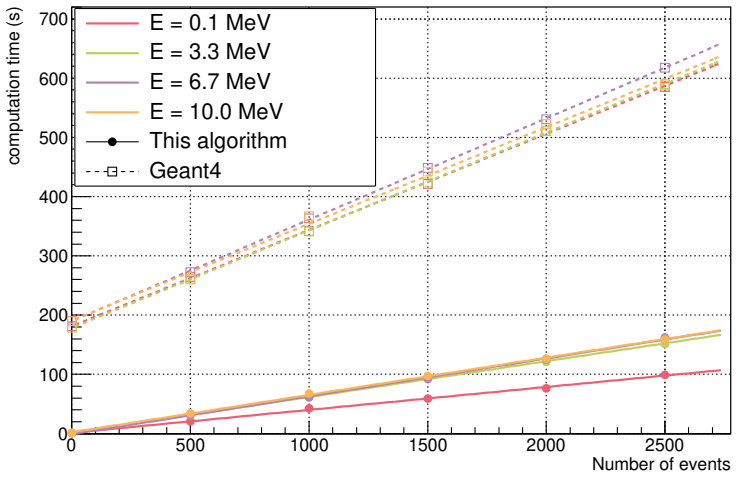

Figure 4.6: Comparison of the presented algorithm for secondary electrons (Sec. 4.2.1, solid lines) with the JUNO Geant4 simulation (Sec. 3.5) (dashed lines) for E_γ = 0.1, 3.3, 6.7, and 10.0 MeV in terms of the computational time. The lines represent estimations for the parameters T_0 and T_{event} from Eq. 4.9 for each E_γ energy, obtained by a fit with equal weights for each data point. One can clearly see a large gain on the CPU time using the algorithm from this thesis, due to differences both in the start-up time T_0 as well as in the T_{event} time needed per event.

were estimated then for each energy separately. The results are then summarized graphically in Fig. 4.6 and numerically in Table 4.1. The large gain in computation time is directly visible. As described in Sec. 3.5, the JUNO Geant4 framework contains a comprehensive description of the detector geometry and the physics processes, which are relevant in the JUNO experiment. It serves the purpose of being a general tool for simulating events in a broad energy range to study analysis methods and particle interactions with a precise model of the detection effects in the JUNO detector. The higher complexity, caused by the higher universality, results especially in a higher start-up time, but as well in a higher time needed per event. Extrapolating the values from Table 4.1 one would need around 4.5 h to simulate 100 000 gammas at 0.1 MeV using the JUNO Geant4 simulation and only about 1 h using the presented algorithm.

Apart from the gain in computational time, the presented algorithm has benefits in easier maintenance. While the JUNO Geant4 framework is a complex framework built upon a software stack of external programs, the presented algorithm consists of single C++ class, which uses methods from the ROOT framework [137].

4.2.4 Results for the non-linearity model of gammas

To evaluate the scintillator non-linearity model for gammas from the simulation of the secondary electron spectrum, the sum of all light emissions from secondary electrons was taken. The non-linearity of the secondary electrons was evaluated using the Birks' law (Eq. 4.2) and the energy loss via the Møller model (Eq. 4.3). It was assumed that there are no correlated

Table 4.1: Comparison of the presented algorithm for secondary electrons (Sec. 4.2.1) with the JUNO Geant4 simulation (Sec. 3.5) for $E_\gamma = 0.1$, 3.3, 6.7, and 10.0 MeV in terms of the computational time. The estimated values for the start-up time T_0 and the computational time needed per event T_{event} as estimated from Fig. 4.6.

	This algorithm		JUNO Geant4	
Energy (MeV)	T_0 (s)	T_{event} (s)	T_0 (s)	T_{event} (s)
0.1	1.41	0.0386	181.23	0.1624
3.3	1.38	0.0604	178.02	0.1650
6.7	-1.10	0.0640	189.77	0.1712
10.0	2.40	0.0629	190.93	0.1631

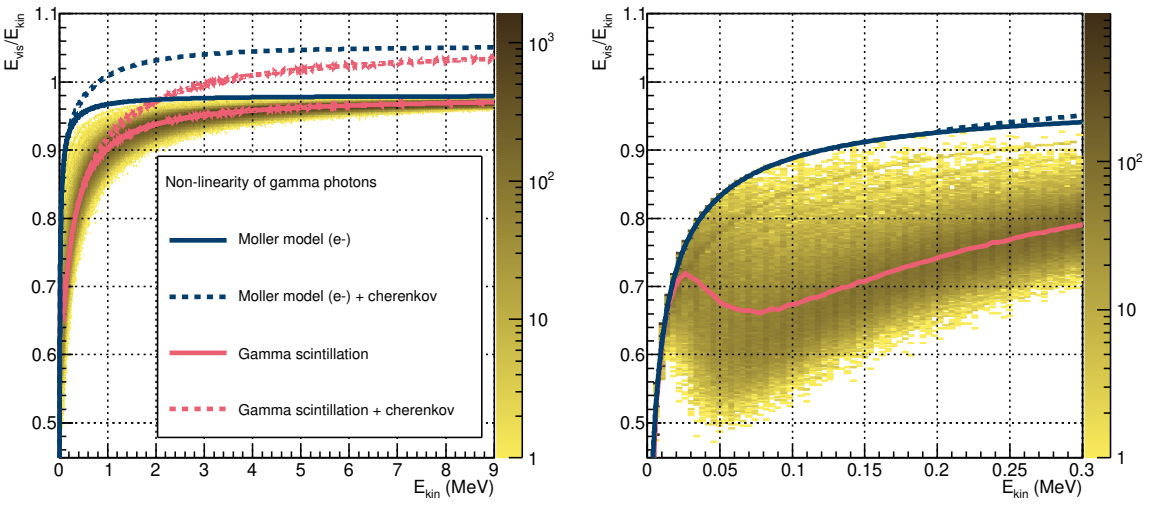

Figure 4.7: The results for the non-linearity $E_{\text{vis}}/E_{\text{kin}}$ model for gammas calculated with the presented algorithm. The distribution of the non-linearity of all gammas without the Cherenkov light is shown in yellow, while the corresponding average non-linearity is shown in solid red. The red dashed curve shows the average non-linearity of gammas with the Cherenkov light included. For comparison, the electron non-linearity curve resulting from the Møller model is shown in blue, without (solid) and with (dashed) lines. The right plot shows the zoom of the left plot in the energy range below $E_{\text{kin}} < 0.3$ MeV.

effects in the light production between different secondary electrons and each of them can be treated individually.

In Figure 4.7 one can see in yellow the evaluation of $E_{\text{vis}}/E_{\text{kin}}$ for about $1.5 \cdot 10^7$ gammas simulated without the Cherenkov light in the energy range $E_{\text{kin}} = E_\gamma$ from 1 keV to 9 MeV. The right plot shows the zoom of the left plot in the energy range below $E_{\text{kin}} < 0.3$ MeV. The average visible energy for the gammas without the Cherenkov light is shown with the solid red line, while the dashed red line represents the case with the Cherenkov light included. For

comparison, the blue lines show the non-linearity model for electrons, again without (solid lines) and with (dashed lines) the Cherenkov light. For the same incident kinetic energy, the visible energy of electrons is always higher (or equal at very low energies) than the visible energy of gammas. This is because the gammas only create visible energy due to secondary electrons, having lower energies and thus, higher quenching (Fig. 4.1 right), with respect to the electron of the same kinetic energy as the original gamma. At very low energies below 20 keV, the photoelectric effect becomes dominant, as it can be seen in Fig. 4.3. This causes the non-linearity curves for electrons and for gammas to be the same, as the full kinetic energy of the gamma is transferred to the electron. In the transition region at around 70 keV, a local minimum of the nonlinearity can be seen in the right plot in Fig. 4.7.

4.3 Non-linearity model for positrons

4.3.1 Positron non-linearity at rest

The energy deposition of positrons at energies of a few MeV happens usually in two steps. First, positrons deposit energy in the scintillator due to ionization and create scintillation light similar to the energy loss of electrons. Additionally, a positron annihilates afterwards with an electron of the detector material to produce gammas. In this section is is assumed, that positrons annihilate at rest into two gammas after depositing their total kinetic energy due to ionization. The resulting two gammas have therefore a total energy of $E_\gamma = m_e c^2 = 511\,\mathrm{keV}$ each. To calculate the non-linearity curve for these positrons, one needs to combine the non-linearity curve resulting from the Bhabha model in Fig. 4.1 and the non-linearity of the two gammas at $E_\gamma = m_e c^2$:

$$E_{vis}^{\mathrm{e}+}(E_{\mathrm{kin}}) = E_{\mathrm{Bhabha}}^{\mathrm{ion}}(E_{\mathrm{kin}}) + 2 \cdot E_{\mathrm{vis}}^{\mathrm{Gamma}}(m_e c^2). \tag{4.10}$$

The result of this evaluation together with the models for the electron non-linearity and the gamma non-linearity are shown in Fig. 4.8. Again, the dashed lines show the full deposited energy of scintillation light and Cherenkov light combined, while the solid lines represent the scintillation light only. Here, the non-linearity is expressed as $E_{\mathrm{vis}}/E_{\mathrm{dep}}$, where the variable E_{dep} is used for the total deposited energy. For electrons and gammas it is $E_{\mathrm{dep}} = E_{\mathrm{kin}}$, while for positrons it is $E_{\mathrm{dep}} = E_{\mathrm{kin}} + 2m_e c^2$.

4.3.2 Evaluation of the full JUNO Geant4 simulation

The calculation of the previous section assumes that positrons always annihilate at rest into two gammas after loosing their kinetic energy completely in the scintillation medium via ionization. The annihilation in flight, the forming of positronium, and the creation of gammas via Bremsstrahlung are not considered. If positronium is formed, there is a chance to form para-positronium (p-Ps) or ortho-positronium (o-Ps). If o-Ps is formed in vacuum, it can not decay into two gammas, as o-Ps has a total spin of 1 and therefore needs to decay into an odd number of photons. However in matter, several effects cause o-Ps to decay into two gammas instead of three [126, 127]. These are e.g. magnetic effects which cause a spin-flip or positron pick-off by surrounding electrons. Moreover, the creation of electron-positron pairs by gammas

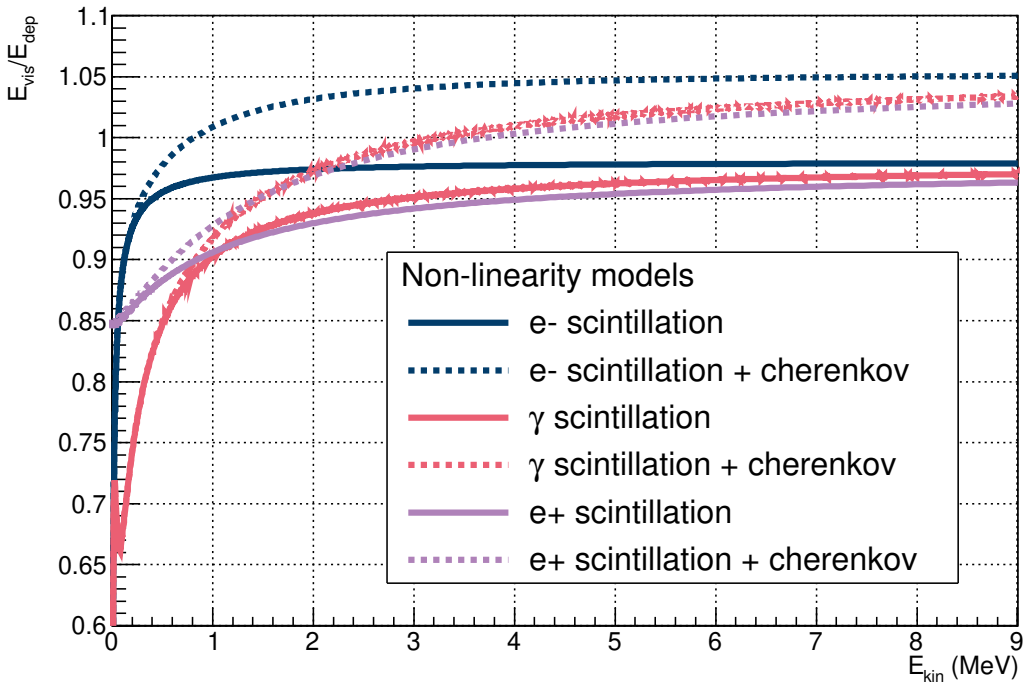

Figure 4.8: The non-linearity $E_{\text{vis}}/E_{\text{dep}}$ (E_{dep} is the total deposited energy) models for positrons (purple), electrons (blue), and gammas (red). The solid curves show the non-linearity curves for scintillation light only, while the dashed curves include also the Cherenkov light.

was not considered in Sec. 4.3.1. To study the impact of these effects, the JUNO Geant4 simulation was used to generate a comprehensive set of particles and their energy depositions created by an initial positron. Also here, the detectable light is entirely produced by positrons and electrons. To evaluate the amount of visible energy, the amount of scintillation light was evaluated from the integration of Birks' formula (Eq. 4.2) and the amount of Cherenkov light was evaluated from Eq. 4.5 for each positron and electron. These contributions were summed up to the visible energy of the full event. To cross-check the validity of the simple positron model from Sec. 4.3.1, a sub-sample of these events was selected, which follows the assumptions of Sec. 4.3.1. These are the annihilation at rest into two gammas after the total kinetic energy is deposited due to ionization. The production of Bremsstrahlung as well as the o-Ps decay into three gammas was not considered in Sec. 4.3.1. In total 970 000 events were simulated in the JUNO Geant4 simulation, from which 78 884 events were contained in the sub-sample following the assumptions of Sec. 4.3.1. The comparison of presented model from Sec. 4.3.1 with the full JUNO Geant4 simulation as well as the selected sub-sample can be seen in Fig. 4.9.

One can clearly see the difference between the positron non-linearity curve and the full simulation, while the selected sub-sample shows no clear difference to the positron non-linearity curve. This approves that the selected sub-sample is well described by the results of Sec. 4.3.1, like it is expected from the validation results of Sec. 4.2.2. It can be further seen, that the deviation of the full simulation to the model barely exceeds 1%, which is the requirement for

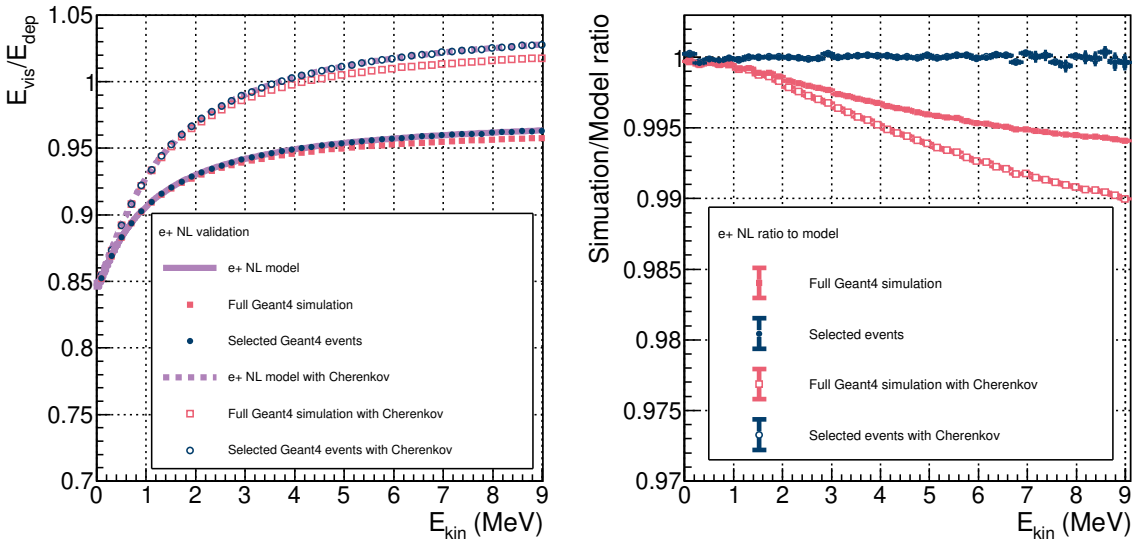

Figure 4.9: Comparison of the positron non-linearity curve from Sec. 4.3.1 to the non-linearity obtained by using the particle set created by the JUNO Geant4 simulation (Sec. 3.5) under usage of the Møller- and the Bhabha model. The graphs on the left show the comparison of the non-linearity model from Sec. 4.3.1 (purple) to all simulation events (red) and selected simulation events, which followed the assumptions of Sec. 4.3.1 (blue). In the right graphs the ratios of the non-linearity evaluated using simulated particles by Geant4 to the non-linearity curve from Sec. 4.3.1 are shown.

the accuracy of the calibrated non-linearity in JUNO. Nevertheless, it is expected to have additional sources of uncertainties as the limited range of calibration sources, as well as the limited amount of calibration data. Therefore, the effects of the annihilation in flight and Bremsstrahlung should to be studied further and be included in the model.

The averaged deviation of the Geant4 evaluation compared to the simple model in dependence of the Birks' constant is shown in Fig. 4.10. The average was taken over the expected JUNO prompt spectrum under the assumption of the normal neutrino mass ordering shown in Fig. 3.11. One can see, that the average deviation is less than 0.5% for the large evaluated range of kB.

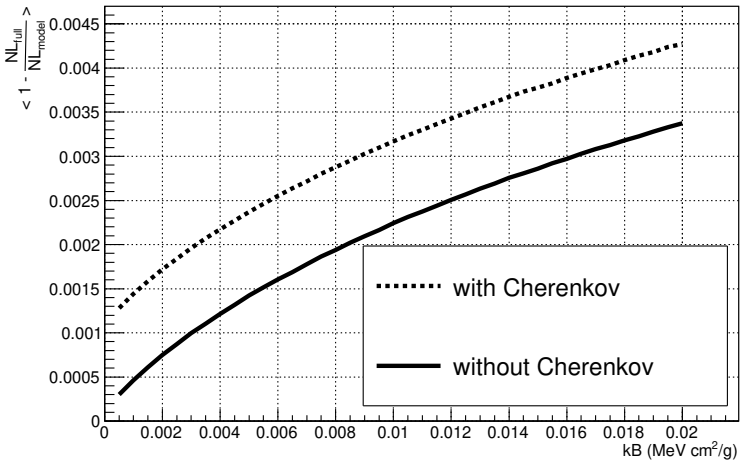

Figure 4.10: The deviation shown in Fig. 4.9 of the simple model to the JUNO Geant4 evaluation versus the Birks' constant averaged over the JUNO prompt spectrum under the assumption of normal neutrino mass ordering.

4.4 Application of the non-linearity model in JUNO

In Fig. 3.9 the spectrum of gamma calibration sources was shown from the calibration programme of the Daya Bay experiment [134]. JUNO plans to use the same spectrum of calibration sources. To avoid non-uniformity effects, one would need to perform this calibration in an area of the detector with a low gradient in the non-uniformity map and a fixed source position, such as the detector center. From the gamma calibration points, the gamma non-linearity curve (Fig. 4.7) can be calibrated. Here, the scintillation light normalization need to be determined, as well as the Birks' constant kB and the set of Cherenkov parameters A_i. Together with the results of Sec. 4.3, this set of parameters can be used to evaluate the non-linearity curve of positrons. Besides the use of gamma calibration sources, a variety of natural sources exists, which can be used for calibration. These include the cosmogenic isotope ^{11}C, for which an event rate of 1.62×10^4 events/day is predicted for JUNO in [11]. The isotope ^{11}C undergoes the β^+ decay into ^{11}B with a decay energy of about 0.96 MeV:

$$^{11}C \rightarrow ^{11} B + \nu_e + e^+ + 0.96\,\text{MeV}. \tag{4.11}$$

These decays are expected to largely dominate the singles spectrum of JUNO in the energy range of about 1 MeV to about 2 MeV, which makes a selection possible [11]. It might be possible to use the known spectral shape of the β^+ decay of the ^{11}C decays to validate the conversion from the gamma non-linearity to the positron non-linearity. Also here, the systematic impact of the non-uniformity in JUNO needs to be minimized under the use of an appropriate vertex reconstruction.

Chapter 5

Vertex Reconstruction

The reconstructed electron anti-neutrino energy in JUNO, which is needed to resolve the MO, depends mainly on the amount of detected photons. For a constant energy the expected amount of detected photons also varies with the emission point of these photons. This light non-uniformity causes an energy smearing due to the uncertainties on the reconstructed light emission point. Due to this reason, a good vertex reconstruction, which can resolve the light emission point with a good resolution, is needed in JUNO.

Moreover, the vertex reconstruction is used to define events inside a so-called *fiducial volume*. The FV serves the purpose of separating signal events from gamma background events from the outside rock and the detector construction materials. As the vertex reconstruction utilizes the full PMT hit information of an event, it typically shows potential to be used to extract more properties of the event. Two possible use-cases are the discrimination of electron and positron events as successfully done in the data analysis of the Borexino experiment [156] or the discrimination of point-like and track-like events as successfully done in the data analysis of the Double Chooz experiment [68]. In this thesis, the presented vertex reconstruction will be used in Chapter 6 to discriminate pile-up events.

This chapter introduces a method to find an estimate for the light emission point under the use of the measured PMT hit times and charges of the LPMT array. As IBD events are in the focus of this thesis, the presented vertex reconstruction focuses on the reconstruction of positron vertices.

5.1 Parameter estimation via log-likelihood minimization

To extract the best estimate for the light emission vertex, a log-likelihood estimation is used.

A Likelihood estimation is a statistical method to obtain estimates of model parameters from a data set, which follows this model. The *Likelihood function* ($\mathcal{L}$) is constructed as the probability to obtain the observed data set with the data points $\vec{x}$ under the assumption of a set of model parameters $\vec{\theta}$. It reads as

$$\mathcal{L}(\vec{\theta}|\vec{x}) = \prod_k p(x_k|\vec{\theta}), \tag{5.1}$$

with $p(x_k|\vec{\theta})$ being the probability to measure the data point x_k under the assumption of the parameter vector $\vec{\theta}$. A maximum of $\mathcal{L}$ is reached for certain set of parameters $\hat{\vec{\theta}}$. This set of parameters can be seen as the best estimate for $\vec{\theta}$ for the given data set under the assumption of the used model.

For practical reasons in computation, typically the logarithm of $\mathcal{L}$ is taken. This preserves the monotony of $\mathcal{L}$, while it transforms the product of probabilities into a sum, which is more practical to calculate. Moreover, the numerical minimization of a function is more practical than the maximization. For this reason the negative log-likelihood function is formed:

$$\ell(\vec{\theta}|\vec{x}) := -\log \mathcal{L}(\vec{\theta}|\vec{x}) = -\sum_k \log p(x_k|\vec{\theta}). \tag{5.2}$$

One advantage of the usage of the log-likelihood estimator compared to the similar χ^2-estimator, is its flexibility. While the χ^2-estimator assumes the usage of Gaussian-distributed data points, any *probability density function* (pdf) can be used in the log-likelihood estimator.

5.2 Creation of the likelihood function

5.2.1 Likelihood function of PMT hit times

The main information of the vertex reconstruction is received from the time information of each PMT hit. After light is produced in the scintillation medium it propagates through the scintillator until it is eventually measured by a PMT. Due to the possibly different distances of PMT's to the light emission point, the measurement time differs due to the different photon propagation times. These differences can be used to estimate the vertex of the light emission as well as the global light emission time T_0. The log-likelihood term for the time fit neglecting the treatment of the DCR, which will be introduced in Sec. 5.2.4 reads as

$$\ell_{\text{time}}(\vec{X}, T_0|\vec{t}) = -\sum_i \log p_s(t_i|\vec{X}, T_0), \tag{5.3}$$

with the minimization parameters of the 3-dimensional light emission point $\vec{X}$, as well as the event time T_0. Here the probability $p_s(t_i|\vec{X}, T_0)$ is read from a pre-calculated probability map containing the time-profile of the measured hit times. The subscript s is used to distinguish this contribution from the event signal from the later introduced DCR.

As the each SPMT is expected to have a similar timing as a dynode LPMT and only about 2.5% of coverage is added by the use of the SPMT system, the reconstruction uses only the LPMT system. In the considered energy range of IBD events from reactor electron anti-neutrinos, no saturation effects for the LPMT array are expected.

5.2.2 Time profile probability map

The pre-calculated probability map for the PMT hit times contains the probability of detecting a photon under the assumption of a distance of the vertex to the PMT and the hit time. Several effects, which are affecting the hit time, need to be included in this map.

LS time profile The major effect on the hit time profile is the decay profile of the scintillator as shown in 3.4 In the JUNO software it is described by the sum of three exponential functions:

$$\phi(t) = \sum_{i=1}^{3} \frac{q_i}{\tau_i} \mathrm{e}^{-t/\tau_i}, \tag{5.4}$$

with τ_i being the decay constants and q_i their weights. As it can be seen from 3.4, these parameters are particle-dependent due to the different ionization densities of particles with different masses. The corresponding values used for electrons and positrons can be found in Tab. 5.1.

Table 5.1: Parametrization of the LS time profile according to Eq. 5.4 from [11].

Parameter	value	Parameter	value
τ_1 (ns)	4.93	q_1	0.799
τ_2 (ns)	20.6	q_2	0.171
τ_3 (ns)	190	q_3	0.03

Time uncertainty from the PMT and the electronics Another important effect which needs to be considered is the time smearing by the PMT measurement itself and its reconstruction. While the FWHM of the time measurement of the PMT can be directly obtained by the implemented TTS values from Tab. 3.1, other parts of the electronics may also introduce a time smearing effect. Additionally, the PMT time reconstruction via the waveform analysis introduces an uncertainty in the measured time as well, which needs to be tested on the algorithm. The full timing effect can be tested on the obtained large statistics data from the PMT testing in JUNO. As this data is not ready for analysis at this point, a preliminary study using the JUNO simulation was performed. A simulation was run with 5000 optical photons with 2.8 eV energy in random directions at the center of the JUNO detector. Moreover, the scintillation process was turned off and the Rayleigh scattering and absorption length was both set to 5000 m to minimize optical effects and obtain almost the same hit time on each PMT. This creates a sharp hit time distribution with about 750 expected hits in the simulation as each LPMT has about the same distance to the detector center in the simulation.

For the simulation of electronics and the reconstruction, the JUNO simulation does not offer a direct correspondence of the reconstructed hits and the simulated ones. Therefore a strict multiplicity trigger condition in the ElecSim of 500 hits in 10 ns with a slip of 1 ns was used to minimize the influence of the uncertainty of the trigger time. For the waveform reconstruction, the default deconvolution algorithm was used. The time distribution of the reconstructed hits relative to their trigger times can be approximated by a Gaussian distribution for each LPMT type. These distributions are shown in Fig 5.1. The uncertainties of the photon arrival times by the PMT measurement were approximated by the σ from a fitted Gauss curve. For the dynode PMT's, a value of $\sigma_{\mathrm{Dyn}} = 3.629$ ns was obtained and for the MCP PMT's, a value of $\sigma_{\mathrm{MCP}} = 6.132$ ns was obtained.

This method for estimating the spread of the photon measurement time can only give a very rough approximate estimation. As the hit correlation is lost, the trigger time, which was used

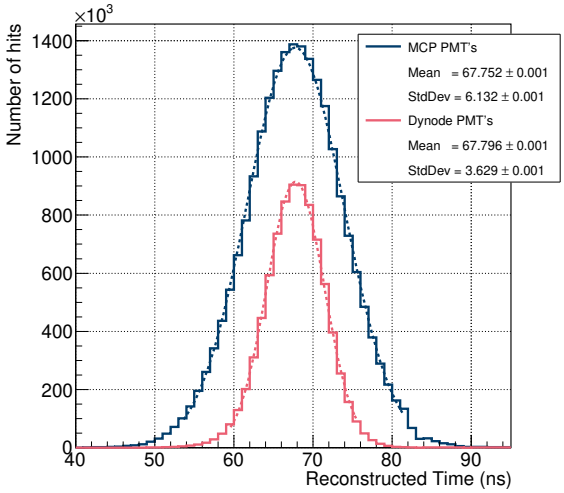

Figure 5.1: Estimation of the time spread from the photon measurement of LPMT's. It was created with a simulation of optical photons from the detector center without the scintillation effect and increased Rayleigh scattering and absorption length of 5000 m each.

to align the hits in Fig. 5.1, is the major source of uncertainty. Depending on the selection criteria of the multiplicity trigger, either a misalignment of the events, or a selection of a sharply distributed sub-sample is caused. However, the obtained values are much larger than the vendor TTS values from Tab. 3.1, which are implemented in the JUNO software. As the TTS effect is expected to be the major effect in the smearing of the hit times, the obtained values can be seen as conservative estimates. In future they they need to be changed to the measured values from the planned PMT testing of the JUNO experiment under the use of the full readout electronics.

Optical effects Major optical effects which need to be considered in the hit time profile are the chromatic distortion of the photons and total reflection on the acrylic glass. As the scintillator emit photons in a broad spectrum of wavelengths and the refractive index of the scintillator is wavelength dependent, the emitted photons travel with different group velocities. This effect creates a smearing of the measured hit profile at the PMT. If the photons were emitted at a large distance to the PMT, the propagation through the scintillator is longer and therefore the effect of the chromatic distortion is larger. Total reflection happens if a photon is emitted in a sufficiently small angle to the tangential plane of the acrylic sphere, making refraction and the propagation through the glass into the surrounding water impossible. This lets the photon be reflected once or a few times on the acrylic sphere until it eventually propagates through it to be measured by a PMT. The effect of total reflection only occurs if the light is emitted near to the acrylic vessel at large radii of

$$R_{\mathrm{TotRef}} = \frac{n_{\mathrm{water}}}{n_{\mathrm{acryl}}} \cdot R_{\mathrm{sphere}} \approx \frac{1.33}{1.48} \cdot 17.7\,\mathrm{m} = 15.9\,\mathrm{m} \Leftrightarrow R^3_{\mathrm{TotRef}} \approx 4000\,\mathrm{m}^3 \tag{5.5}$$

Total reflection process causes these photons to be measured at late times and large distances of the PMT to the vertex. Other optical effects are the Rayleigh scattering and the absorption

of photons on molecules [157]. Also these effects are wavelength dependent. The Rayleigh scattering length and the absorption length of the JUNO scintillator were not measured so far, but are expected to be measured in the calibration programme. In the JUNO software, estimates for the Rayleigh scattering length of 27 m at 430 nm wavelength and the absorption length of 77 m at 430 nm are implemented. These values represent typical values, which are expected for the used LS mixture [11].

Creation of the time profile map As all the mentioned effects, as well as the JUNO geometry is implemented in the Geant4-model of the JUNO software, it was used to create a two-dimensional probability map for the PMT hit time distribution. This map contains pre-calculated values for the probability to measure a PMT hit at a certain time under the assumption of a distance to the PMT. Due to the discussed optical effects, the description of the hit time probability using only one dimension with an appropriate time-of-flight correction is not sufficient.

For the calculation of the probability map, a simulation of 200,000 electrons with kinetic energies distributed uniformly between 0 and 7 MeV, uniformly distributed in the LS volume, was used. Positrons from the IBD interactions from reactor electron anti-neutrinos are in the focus of this reconstruction. Electrons were chosen for the creation of the probability map as they have the same LS time profile as positrons. Moreover, due to the missing annihilation gammas, the ionization energy is deposited inside a smaller volume, which increases the resolution of the map and avoids the effect of light loss at the edges of the acrylic vessel. The hit times, obtained from the simulation, are shown in Fig. 5.2 on the left side. Each hit was sorted into a two-dimensional histogram with 1100 equal-width bins on the X-axis, which is used for the distance to the PMT, from 0 to 41800 mm distance. The Y-axis is used for the arrival time of the photon on the photo-cathode and is divided into 2300 equal-width bins from -300 ns to 2000 ns, for which the point at 0 ns stands for the time, when the initial electron was created by the Geant4-simulation. To avoid numerical problems in the further calculation, for each distance bin, the time distribution was normalized to 1. After that, to smooth out the time distribution and apply the smearing of the time measurement of the PMT the time distribution was convoluted with a Gaussian. The σ of the applied Gaussian smearing was taken from the estimated time smearings shown in Fig. 5.1. Another Gaussian convolution was applied to each distance distribution for each time bin. In order to do that, the whole distribution was temporarily corrected by an approximate time-of-flight by aligning the time distribution maxima of each distance bin, which was reverted after the convolution. The convolution in distance direction uses a Gaussian with a width of $\sigma = 50$ mm. This convolution has no direct physical motivation, but has the purpose of smoothing out the probability map in order to avoid a non-continuous behavior. To finish up the probability map, the time distribution of each distance bin was normalized to 1 again. The finalized map for the dynode PMT type can be seen on the right side of Fig. 5.2. For the better visibility, Fig. 5.3 shows example time probability distributions for the distances of 3 m and 36.85 m for both LPMT types. One can clearly see the shift between both distances due to the longer time-of-flight. Furthermore, the second maximum, which can be seen in the time distribution at 36.85 m stems from the late photons which were totally reflected on the acrylic sphere.

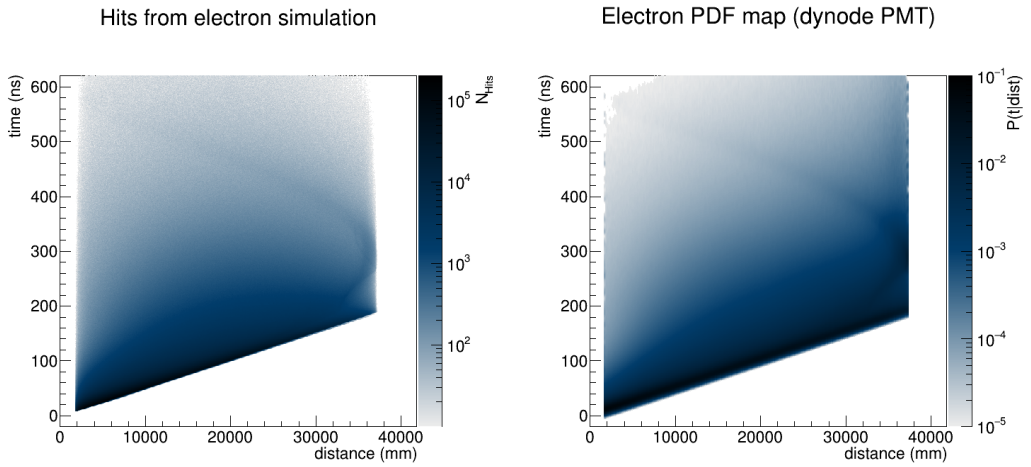

Figure 5.2: The time probability map for dynode PMT's. On the left side, the PMT hits from the electron simulation are shown. The number of hits is shown in the dependence of hit time and distance to the PMT. On the right side, the obtained probability map is shown, which contains the probability to measure a hit at a certain time under the assumption of a certain distance to the PMT. In this map a value of $T_0 = 0$ is shown. To obtain the probability $p_s(t_i|\vec{X}, T_0)$ one needs to correct the measured times accordingly for $T_0 \neq 0$. One can clearly see the effects of the total reflection on the acrylic sphere as an arc at high times.

5.2.3 Likelihood function of PMT charges

Another part of the log-likelihood function is the one on the total charge of each LPMT. As the total number of p.e. measured by the PMT is expected to be Poissonian distributed, this probability distribution was also assumed for the distribution of calibrated measured charges $\vec{q}$ in units of p.e. The corresponding term of the log-likelihood function, neglecting the treatment of the DCR introduced in Sec. 5.2.4, is

$$\ell_{\text{charge}}(\vec{X}|\vec{q}) = \sum_{k\in\{\text{All LPMT's}\}} q_{\text{pred},k}(\vec{X}, q_{\text{tot}}) - q_{\text{meas},k} \log q_{\text{pred},k}(\vec{X}, q_{\text{tot}}), \tag{5.6}$$

with the minimization parameters of the light emission point $\vec{X}$. The predicted charge for PMT k, $q_{\text{pred},k}(\vec{X}, q_{\text{tot}})$, depends on the light emission point $\vec{X}$, as well as on the total measured charge q_{tot}. Like the PMT hit time probability, the amount of charge measured at a PMT was estimated under the use of a two-dimensional map. This two-dimensional map contains the average charge on a PMT divided by the total charge of the event in dependence of the distance of the vertex to the PMT and the angle between the facing direction vector of the PMT and the simulated event vertex vector. It was created under the use of the same electron simulation as for the creation of the time probability map. This map is shown in Fig. 5.4 on the left side.

The cosine of the angle $\cos(\alpha)$ is calculated via the scalar product of the energy deposition vertex vector $\vec{X}$ and the PMT facing vector $\vec{v}_{\text{PMT}}$:

$$\cos(\alpha) = \frac{\vec{X} \cdot \vec{v}_{\text{PMT}}}{|\vec{X}| \cdot |\vec{v}_{\text{PMT}}|}. \tag{5.7}$$

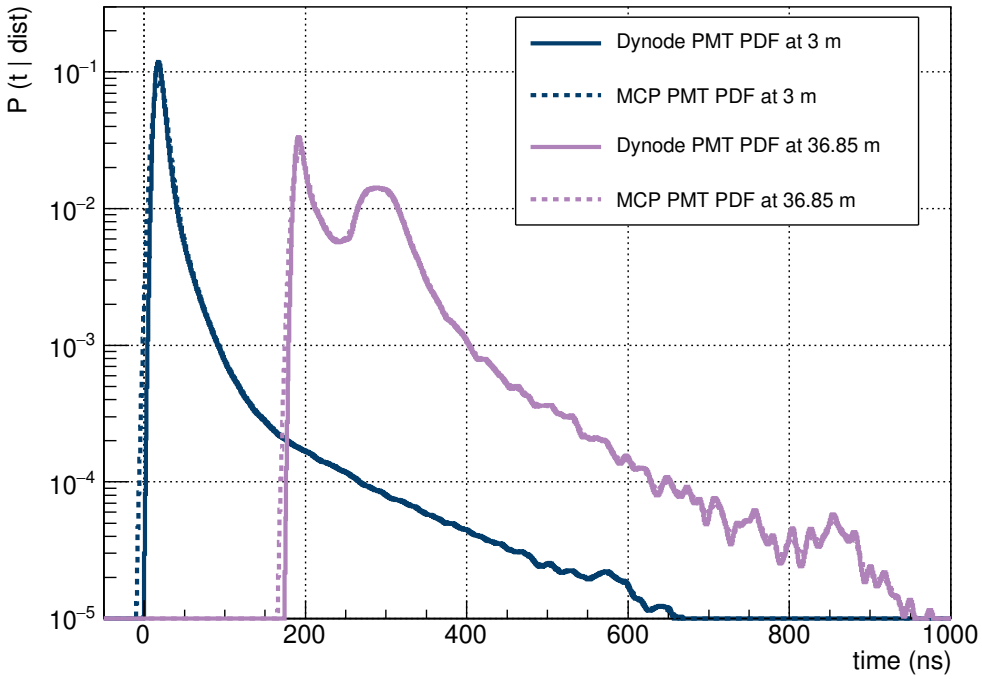

Figure 5.3: Example time probability distributions for both LPMT types at the distances of the PMT to the vertex of 3 m and 36.85 m. In the distribution at 36.85 m, one can clearly see the second maximum from the late totally reflected photons.

The PMT facing vector $\vec{v}_{\mathrm{PMT}}$ is equivalent to the vector from the PMT center to the detector center. For a vertex on the line between the PMT and the detector center, the angle would be $\cos(\alpha) = -1$. In both, the creation of the map and in the reconstruction algorithm, Eq. 5.7 is used for the calculation of $\cos(\alpha)$. Therefore, the cosine of α was used directly to save the computational time of calculating the arccosine. The right side of Fig. 5.4 shows an example charge expectation map for the PMT with the ID 1 in the Cartesian detector coordinates in the x-z-plane. The center of this PMT is placed at the coordinates $(x, y, z) = (1065.41\,\mathrm{mm}, 0, 19470.9\,\mathrm{mm})$ and marked with a star in the graphic.

This map is created as an average of all simulated events. To obtain the charge expectation for a specific vertex, one needs to multiply the value at the currently tested vertex from the map and multiply it with the total expected signal charge. It is assumed that the charge in each PMT increases linearly with the total measured charge from all PMT's for each position in the detector. To check this assumption, three maps were created from three sub-samples of the electron simulation. For the creation of these sub-samples, events in the energy range up to 2.5 MeV, between 2.5 MeV and 5 MeV, and above 5 MeV deposited energy were selected. The individual charge expectation maps from each sub-sample showed no significant difference to each other so the assumption of the charge linearity with the total deposited charge was found to be valid.

As it can be clearly seen in Fig. 5.4 for each PMT there is a so-called *dark region* at large

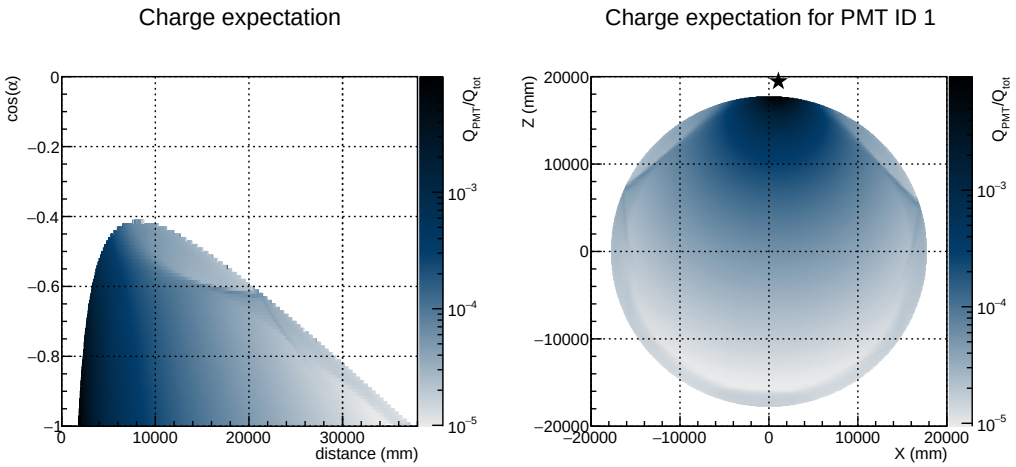

Figure 5.4: The charge expectation of a PMT. The left side shows the ratio of detected charge at the single PMT to the total charge measured in the whole detector in dependence of the measurement distance and angle between the facing vector of the PMT and the event vertex vector from Eq. 5.7. The right side shows the same ratio from the perspective of PMT 1 at $(x, y, z) = (1065.41\,\text{mm}, 0, 19470.9\,\text{mm})$ on the x-z-plane of the JUNO detector for illustration. The position of this PMT is marked with a star.

angles, caused by the effect of total reflection on the acrylic sphere. If an event occurs in the dark region of the PMT, the PMT is expected to see only a small amount of re-emitted light as the direct light can not reach the PMT. At smaller angles one can see, that the expected charge on the PMT decreases smoothly like expected with increasing distance of the light emission point. Besides the effect of the decreasing aperture of the PMT, this effect is enhanced by light attenuation. At very large distance on the opposite side of the LS volume from the PMT point-of-view however, the expected charge increases again as the light emission point moves towards the acrylic sphere. Also this effect can be explained by the reflection of light on the acrylic sphere. Due to several reflection on the acrylic wall, the light can reach the PMT's on the opposite side of the CD.

While different QE values for each PMT are not implemented in the JUNO software, each PMT uses a different CE value. As the charge expectation was calculated as average of all LPMT's, the expected charge of each PMT in the reconstruction needs to be corrected by the deviation from the average efficiency. In the used version of the JUNO software, the CE distribution is implemented as a Gaussian distribution with a mean of $\mu = 90.0\%$ and a width of $\sigma = 6.4\%$. A calculated CE from this distribution above 100% is treated as CE=100% in the ElecSim simulation code of the JUNO software. In the reconstruction these values from the software were used to correct the expected charge for the CE value distribution of each PMT to be compatible to the analyzed simulation.

For the application of measured data from the JUNO detector, the charge expectation needs to be recalculated using the final measured LS values and LPMT parameters. The individual CE corrections need to be replaced by analogous individual DE corrections obtained from the PMT tests.

5.2.4 Treatment of dark counts

Individual DCR's of the PMT array

During the run-time of the JUNO experiment, the DCR of each PMT is planned to be monitored by random triggers. Due to this continuous monitoring, the uncertainty on the average DCR of each PMT is assumed to be negligible compared to the statistical fluctuation of the number of dark counts in a single event on a PMT. The expected total amount of dark counts at PMT k with the DCR $R_{\mathrm{DCR},k}$ in a readout window with the time duration T_{DAQ} can be calculated by

$$\lambda_{\mathrm{DCR},k} = R_{\mathrm{DCR},k} \cdot T_{\mathrm{DAQ}}. \tag{5.8}$$

The individual DCR's for each LPMT, according to its type, were randomly assigned following the DCR distributions from the PMT tests in JUNO, presented in [114]. These tests are preliminary tests, performed without the final readout electronics setup and PMT bases. During the PMT tests, all dynode PMT's with a DCR of more than 50 kHz and all MCP PMT's with a DCR of more than 100 kHz are rejected from the use in the JUNO detector. The distribution of DCR's for all remaining PMT's is shown in Fig. 5.5. Under the assumption

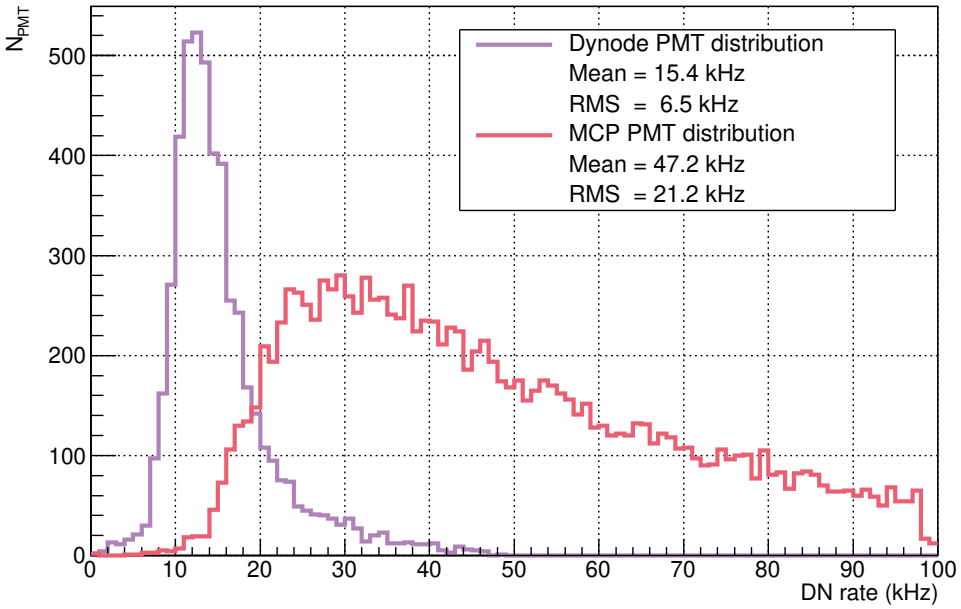

Figure 5.5: The distribution of DCR's for both LPMT types as it is applied in this work. These DCR's follow the measured DCR distribution at the PMT testing site of JUNO [114].

of $T_{\mathrm{DAQ}} = 1250\,\mathrm{ns}$, Eq. 5.8 yields a range from $\lambda_{\mathrm{DCR},15375} = 6.7 \cdot 10^{-4}\,\mathrm{hits}$ to $\lambda_{\mathrm{DCR},5183} = 0.124\,\mathrm{hits}$ for the applied PMT DCR's. The version of the JUNO software, which was used in this thesis does not contain such a realistic distribution of DCR's for each PMT, but assumes the same DCR for each PMT. For the use of an appropriate DCR distribution, the creation of dark counts was switched off in the JUNO software for the event production. Instead the reconstruction algorithm adds a Poissonian distributed amount of dark counts by itself, using

the applied average rate for each PMT shown in Fig. 5.5, before the reconstruction of the event.

Impact on the charge prediction of each PMT

To adjust the Likelihood function of PMT charges, the expected DCR contribution can be added to the expected charge of each PMT. The predicted charge from Eq. 5.6 needs to be replaced by the sum of the signal part and the DCR part:

$$q_{\text{pred},k}(\vec{X}, q_{\text{tot}}) \rightarrow q_{\text{pred},k}(\vec{X}, q_{s,\text{tot}}) = q_{s,k}(\vec{X}, q_{s,\text{tot}}) + \lambda_{\text{DCR},k}. \tag{5.9}$$

Here, the total amount of signal charge on the PMT k is described by $q_{s,k}(\vec{X}, q_{s,\text{tot}})$ with the total signal charge $q_{s,\text{tot}}$. The signal part of the total expected charge $q_{s,k}(\vec{X}, q_{s,\text{tot}})$ is extracted from the charge expectation map in Fig. 5.4, while the expected amount of dark counts is calculated according to Eq. 5.8. Before the reconstruction, only the total measured charge q_{tot} is known, but due to the statistical fluctuations of the DCR contribution, the total amount of signal charge $q_{s,\text{tot}}$ is not known. This parameter is therefore added as a minimization parameter in the log-likelihood function (Eq. 5.6):

$$\ell_{\text{charge}}(\vec{X}|\vec{q}) \rightarrow \ell_{\text{charge}}(\vec{X}, q_{s,\text{tot}}|\vec{q}). \tag{5.10}$$

For a better stability of the minimization the parameter $q_{s,\text{tot}}$ is constrained by an additional Gaussian pull-term:

$$\text{pull}_{\text{charge}}(q_{s,\text{tot}}|q_{\text{tot}}) = \frac{(q_{s,\text{tot}} - \hat{q}_{s,\text{tot}})^2}{\lambda_{\text{DCR,tot}}}, \tag{5.11}$$

with $\hat{q}_{s,\text{tot}} = q_{\text{tot}} - \lambda_{\text{DCR,tot}}$ and $\lambda_{\text{DCR,tot}}$ being the total expected amount of dark counts from all PMT's:

$$\lambda_{\text{DCR,tot}} = \sum_{k \in \{\text{All LPMT's}\}} \lambda_{\text{DCR},k} \tag{5.12}$$

Impact on the PMT hit time distribution

Dark hits are affecting not only the total charge at each PMT, but also the time profile. As dark counts occur independent of the signal, they are uniformly distributed in the time profile of each PMT. The expected hit time probability in Eq. 5.3 needs to be adjusted to contain this uniform distribution of dark count hits. To add up the time probability distribution of the signal (Fig. 5.2) and the uniform DCR probability distribution on the PMT k, the following formula was used, which calculates the probability to measure a PMT hit time t_i:

$$p_s(t_i|\vec{X}, T_0) \rightarrow p_k(t_i|(\vec{X}, T_0, q_{s,\text{tot}})) = \frac{p_s(t_i|\vec{X}, T_0) \cdot \lambda_{s,k}(\vec{X}, q_{s,\text{tot}}) + R_{\text{DCR},k} \cdot 1\,\text{ns}}{\lambda_{s,k}(\vec{X}, q_{s,\text{tot}}) + \lambda_{\text{DCR},k}}. \tag{5.13}$$

This equation weights the contribution of the signal time profile and the uniform DCR time profile by their expected charge contribution. Here, the expected amount of signal PMT hits $\lambda_{s,k}(\vec{X}, q_{s,\text{tot}})$ was used as the charge information is not used in the time part of the likelihood

fit. It is calculated with the approximation, that the number of hits is linear with the amount of charge and that each dark count hit has an expected calibrated charge of 1 p.e:

$$\lambda_{s,k}(\vec{X}, q_{s,\mathrm{tot}}) = \lambda_{s,\mathrm{tot}} \cdot \frac{q_{s,k}(\vec{X}, q_{s,\mathrm{tot}})}{q_{s,\mathrm{tot}}} \quad \text{with} \quad \lambda_{s,\mathrm{tot}} = N_{\mathrm{tot}} - (q_{\mathrm{tot}} - q_{s,\mathrm{tot}})\,, \tag{5.14}$$

with the total number of reconstructed hits N_{tot}. The DCR $R_{\mathrm{DCR},k}$ is multiplied with 1 ns, because it is the bin width of the time profile map, which is used to determine $p_s(t_i|\vec{X}, T_0)$. Its denominator re-normalizes the full probability to 1 again under the assumption, that the signal hit probability vanishes outside of the readout window.

This dark count treatment also introduces the minimization parameter $q_{s,\mathrm{tot}}$ in the time likelihood function (Eq. 5.3):

$$\ell_{\mathrm{time}}(\vec{X}, T_0|\vec{t}) \rightarrow \ell_{\mathrm{time}}(\vec{X}, T_0, q_{s,\mathrm{tot}}|\vec{t}) \tag{5.15}$$

The full log-likelihood function with dark count treatment

Following this discussion on the impact of dark counts, combining Eq. 5.15, Eq, 5.10, and Eq. 5.11, the full log-likelihood function reads as:

$$\ell_{\mathrm{Full}}(\vec{X}, T_0, q_{s,\mathrm{tot}}|\vec{t}, \vec{q}) = \ell_{\mathrm{time}}(\vec{X}, T_0, q_{s,\mathrm{tot}}|\vec{t}) + \ell_{\mathrm{charge}}(\vec{X}, q_{s,\mathrm{tot}}|\vec{q}) + \mathrm{pull}_{\mathrm{charge}}(q_{s,\mathrm{tot}}|q_{\mathrm{tot}}), \tag{5.16}$$

with 5 parameters: The light emission vertex $\vec{X}$, the global event time T_0, and the absolute total signal charge $q_{s,\mathrm{tot}}$.

5.2.5 Accuracy of the detector response model

The creation of the pre-calculated maps rely here completely on the implementation of the JUNO simulation. A different approach would be the creation of these maps under the use of calibration data. As described in Sec. 3.4, the JUNO calibration programme foresees the use of gamma sources at many positions and energies in the detector. This allows the creation of the pre-calculated maps analogous to Fig. 5.2 and 5.4. However, in the analogous map to Fig. 5.2, the time-alignment of the PMT hits is missing. As the calibration gamma sources are radioactive sources, each decay happens at a randomized time so that the time of the creation of the gamma is lost. This time would need to be reconstructed for each event before the calibration data could be used, which introduces an uncertainty on the hit times from the time-alignment. Moreover, the maps shown in Fig. 5.2 and 5.4 are created under the use of an electron sample, since electrons deposit ionization energy in a rather small volume compared to gammas (see Fig. 3.7). Moreover, a single gamma travels a distance on the order of about $\sim$10 cm before it undergoes its first Compton scattering. While the position of the source is, depending on the calibration system, well known up to a sub-centimeter precision, the average position of the creation of ionization energy has a rather high uncertainty. It can be interpreted to a missing vertex alignment of the calibration data. This effect causes a smearing of the created maps. The spill-out of gammas at the detector edge could cause a bias.

The creation of Fig. 5.2 and 5.4 via the JUNO simulation could suffer from a possible mismatch between the simulation and the measurement. The simulated physical processes (see

Appendix A) are well-known and are expected to be correctly simulated. Moreover, in the simulation the maps rely on the knowledge of the LS characteristics, the characteristics of the PMT's, as well as a precise knowledge of the shape and refractive index of the acrylic sphere. The LS time profile, the scintillation photon spectrum, as well as the optical properties of the LS and the acrylic sphere, are expected to be precisely measured externally [158]. The PMT tests of JUNO plan to measure the PMT properties, such as the TTS and DCR, with the full electronics setup [114]. The attenuation length and the DCR of each PMT are expected to be continuously monitored during the run-time of the JUNO detector. If all these measurements are used in the simulation, the simulation software can be tested and improved on the calibration data. A possible mismatch between the simulation data and the calibration data would lead to biases and imprecisions for this method of creating the maps. Due to the meticulous efforts of measuring the detector properties and the disadvantages of the calibration data, the simulation data is assumed here to yield better results for the vertex reconstruction. This assumption needs to be tested on the calibration data, once ready.

5.3 Minimization of the Likelihood function

To minimize the likelihood function, an appropriate minimization algorithm is needed. If the parameter space can be reasonably constrained, the simplest way of finding the minimum is to scan the full parameter space and evaluate the negative log-likelihood at all possible positions. This way of finding the minimum would guarantee to find always the global minimum in a constant time. If assumptions, such as smoothness or monotony, of the negative log-likelihood function can be found, the minimum can be found in a much smaller time. In general the purpose of a minimization algorithm is to find reliably the minimum, while requiring a reasonable computing time. For the minimization of likelihood functions, often the Minuit package [159] is used. As Minuit was found to be highly unstable for the given problem, a more robust minimization procedure is used here. In the minimization procedure used here, the first estimate of the light emission point is found via the charge center reconstruction described in Sec. 5.3.1. From this reconstructed point, the likelihood function is minimized via the *SIMPLEX*-algorithm as implemented in the ROOT framework [137]. The SIMPLEX algorithm was found to be much more stable than the Minuit algorithm, but still claims a failed minimization in many cases. Although if it claims to be failed, the SIMPLEX algorithm can improve the first estimate from the charge center reconstruction in most cases. Moreover, it gives an estimate for the global event time T_0, which is not provided by the charge center reconstruction. Afterwards, the grid search algorithm, which will be presented in Sec. 5.3.2, is called. The grid search algorithm is used to provide a stable minimization of the log-likelihood function and is expected to always converge to a local minimum around its starting point. It was found, that the grid search algorithm is more effective in finding the minimum, than the SIMPLEX algorithm, while the SIMPLEX algorithm is much more time efficient. Therefore, the seeding of the grid search on the output of the SIMPLEX algorithm was found to improve the time efficiency, while maintaining the good effectivity of the grid search algorithm.

5.3.1 Charge center reconstruction as starting point

To find a first estimate of the position of the light emission vertex, the charge center of the event is calculated. This serves the purpose of finding a start point for the minimization of the log-likelihood function. The charge center is the average of the PMT positions weighted with the measured charge q_k:

$$\vec{X}_{\text{cc}} = c_{\text{corr}} \cdot \frac{\sum_{k\in\{\text{All LPMT's}\}} q_k \cdot \vec{X}_k}{\sum_k q_k}. \tag{5.17}$$

The charge center radius $R_{\text{cc}} = |\vec{X}_{\text{cc}}|$ is shifted to the light emission vertex radius $R_{\text{vertex}} = |\vec{X}_{\text{vertex}}|$ by a correction factor of about $c_{\text{corr}} = \langle R_{\text{vertex}}/R_{\text{cc}}\rangle$ =1.228. After correcting for this bias, the light emission vertex can be found with a precision of about 30 cm to 40 cm for energies of about 5 MeV.

Here, the correction factor c_{corr} was calculated from the used simulation. The charge center algorithm is expected to be biased. An analytical calculation, neglecting any optical effects of the JUNO detector, would yield an correction factor of $c_{\text{corr}} = 1.5$ [139].

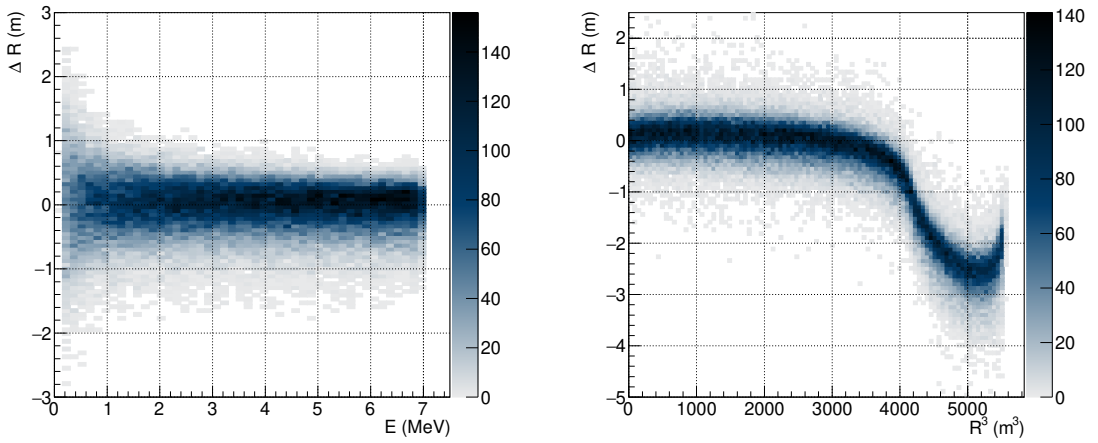

(a) (b)

Figure 5.6: Distribution of the difference ΔR of the reconstructed radius and the simulated radius for the charge center reconstruction. The blue colored histogram shows the distribution of reconstructed electron radii. The charge center was calculated via Eq. 5.17 and corrected with the factor c_{corr} =1.228. Figure 5.6a shows the distribution in dependence of the deposited energy. Only events with a simulated radius of $R < 16$ m were selected here due to the large bias at large radii. Figure 5.6b shows the distribution in dependence of the simulated radius.

5.3.2 Grid search algorithm

This grid search algorithm has the requirement of providing a stable minimization after the initial minimization of the SIMPLEX algorithm. The idea of the algorithm was introduced in

a similar vertex reconstruction algorithm, presented in [139].

This algorithm, which is supposed to minimize the log-likelihood function $\ell(\vec{\theta})$ with the parameter vector $\vec{\theta}$, requires a start point of central parameters $\vec{\theta}_c^0$ with initial step lengths for these parameters $\vec{\Delta}^0$, as well as a termination condition on the step length $\vec{\Delta}_{\min}$. It uses an iterative approach. In each iteration of the algorithm, numbered with the index i, a set $\mathbf{T}^i$ of perturbed parameter vectors $\vec{\theta}_p^i$ created via perturbation of the central parameters $\vec{\theta}_c^i$ by their step length:

$$\mathbf{T}^i = \{\vec{\theta}_p^i \ : \ \theta_{p,j}^i = \theta_{c,j}^i + \epsilon \cdot \Delta_j^i \ , \ \epsilon \in \{-1, 0, 1\}\}. \tag{5.18}$$

For the perturbed parameter vectors in this set, the log-likelihood function is evaluated. In the presented vertex reconstruction, the minimization is constrained on the LS target from the simulation, such that only perturbated parameter vectors with $|\vec{X}| < 17.7\,\mathrm{m}$ are considered here. This has the physical reason, that the larger fraction of the considered light is scintillation light, which originates partly from re-emitted Cherenkov light. Scintillation light can only be produced in the LS medium, while outside the LS medium only small amounts of Cherenkov light can be produced in the Buffer water. Due to the different properties of the light created outside the LS target, the presented vertex reconstruction is not expected to yield trustable results there. Moreover, the constraint on the LS target volume is a technical requirement as the reconstruction uses pre-calculated maps from simulations inside the LS target. Therefore, these maps and the likelihood function are only defined inside the LS target, which makes this constraint necessary.

The perturbed parameter vector with the minimal evaluated log-likelihood function is set then to be the central parameter vector of the next iteration:

$$\vec{\theta}_c^{i+1} = \underset{\vec{\theta}_p^i \in T^i}{\arg\min}\, \ell(\vec{\theta}_p^i). \tag{5.19}$$

If the minimum is found in the center of the evaluated grid, the step length of each parameter is halved:

$$\vec{\Delta}^{i+1} = \begin{cases} \vec{\Delta}^i/2 & \text{if } \vec{\theta}_c^{i+1} = \vec{\theta}_c^i \\ \vec{\Delta}^i & \text{otherwise} \end{cases} \tag{5.20}$$

This lets the parameter space be explored in a finer grid, which increases the precision of finding the position of the minimum. If the step length is not changed, the calculated log-likelihood values are cached to increase the computational efficiency of this algorithm. In the case the step length of each parameter is reduced below its termination condition, such that $\vec{\Delta}_j^{i+1} < \vec{\Delta}_{\min,j}$ for each component of the step length vector, the minimization process is stopped.

5.4 Bias and resolution of the reconstructed vertices

The same electron sample, which was used for the creation of prediction maps (Sec. 5.2.1 and Sec. 5.2.3) will be also used in this section to evaluate the resolution and the bias of the vertex reconstruction. This simulation contains electrons uniformly distributed in the LS target with a uniform kinetic energy from 0 to 7 MeV. It was propagated through the ElecSim

stage of the simulation with a multiplicity trigger condition of 200 PMT hits in 300 ns. This condition yields a full trigger efficiency at about 0.25 MeV. Moreover, a simulation of positrons was created with the same distribution of initial vertices and kinetic energies. Due to the annihilation of the positrons, the deposited energy of the positrons is shifted to the kinetic energy by $\Delta E = 2 \cdot m_e c^2 \approx 1.022\,\text{MeV}$. The deposited energy E_{dep} describes here the total energy, which was deposited inside the LS medium. Due to the long range of the annihilation gammas, they can exit the LS target and the deposited energy of the positrons can be smaller than $2 \cdot m_e c^2$.

As the energy resolution of JUNO is mostly affected by the resolution of the reconstructed radius, its bias and resolution is used as a benchmark for the performance of the presented vertex reconstruction in this chapter.

For the estimation of the presented resolutions in this chapter, the estimator for the sample standard deviation is used, which will be referred to by *RMS*.

5.4.1 Nominal resolution

The evaluation of the electron sample can be seen in the plots in Fig. 5.7. These plots show the distribution of the difference between the radius of the reconstructed vertex and the radius of the simulated vertex. The simulated vertex is defined here as the average position of energy depositions of the events weighted with the deposited energy of the Geant4 simulation step. Figure 5.7a shows the distribution against the simulated deposited energy and Fig. 5.7b shows the distribution against the simulated vertex. Here, only deposited energies inside the LS target were counted towards the total deposited energy. The average of the distribution shows the bias of the reconstruction and is shown in red for electrons. Additionally, the average of the distribution of the positron sample is shown in violet in the same figure. As positrons and electrons were simulated in a different deposited energy range, for the distributions against the radius only events in the deposited energy region $1.022\,\text{MeV} < E_{\text{dep}} < 7.0\,\text{MeV}$ are selected for better comparison between electrons and positrons. Figure 5.8 shows the same distributions for the reconstructed zenith angle θ.

5.4.2 Total reflection effects

In the resolution against the radius in Fig. 5.9b a large drop above about R^3=4000 m^3 $\Leftrightarrow$ R≈15.9 m can be observed, where the resolution drops from about 7-8 cm to below 4 cm. This drop is stronger for electrons than for positrons, which can be explained by the sharper spatial energy deposition of electrons. The energy dependencies of the resolution separated in both regions are shown in Fig. 5.9c. One can see in Fig. 5.9a that the low resolution of positrons below about 1 MeV is caused by events near the acrylic sphere, which deposited large fractions of their energies outside of the LS target due to the long range of the annihilation gammas. In Fig. 5.9c one can see, that these events show no significant abnormal behavior. This large drop of resolution can be explained by the effects of total reflection.

The major effect of the total reflection is the creation of a dark region as it can be seen in the charge expectation map in Fig. 5.4. PMT's in this dark region have a low probability to receive a PMT hit from scintillation light as it can not reach the PMT directly, but only

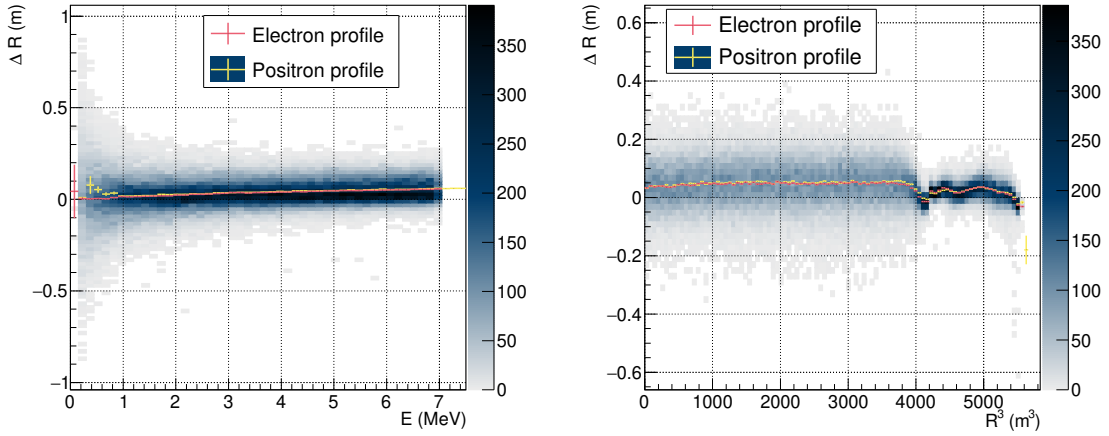

(a) (b)

Figure 5.7: Distribution of the difference ΔR of the reconstructed radius to the simulated radius. Figure 5.7a shows the distribution in dependence of the deposited energy and Fig. 5.7b shows the distribution in dependence of the simulated radius. The distribution is shown in blue, while the red data points show the bias of the reconstructed radius of the electron sample and the yellow data points show the bias of the reconstructed radius of the positron sample. Both analyzed samples have simulated kinetic energies from 0 to 7 MeV. To have comparable samples, Fig. 5.7b shows only deposited energies between 1 MeV and 7 MeV.

due to scattering or re-emission. Moreover, other PMT's have higher probabilities to measure scintillation light which was totally reflected on the acrylic sphere. These effects create a characteristic ring structure on the measured hit pattern on the PMT array. This ring structure is illustrated in Fig. 5.10a. Figure 5.10a shows the summation of the PMT hit patterns from a simulation of 100 electrons with 5 MeV kinetic energy and a initial vertex of $(x, y, z) = (16.32\,\text{m}, 0, 0)$. The PMT hit pattern is shown as a distribution in dependence of the azimuth angle difference ($\Delta\phi$) and the zenith angle difference ($\Delta\theta$) of the hit PMT to the simulated vertex. Here, the PMT hit pattern is created from the simulated hits and not from the reconstructed hits. It can be clearly seen, that the highest amount of PMT hits is at the center of the shown distribution at the lowest distance of the PMT's to the simulated vertices. The amount of hits decreases rapidly to more distant PMT's and then increases again due to the discussed effects of total reflection.

Another effect of total reflection are additional peaks in the hit time distribution, which is shown against the distance to the PMT in Fig. 5.10b. At distances around 15,000 mm one can see also in this plot the dark zone, where the amount of hits is rather low. At larger distances above 30,000 mm one can see distinct additional peaks in the PMT hit time distribution, which are caused by the total reflected photons, which could not be measured as PMT hits in the dark zone. The time of these additional peaks depends also on the distance of the light emission vertex to the PMT and therefore provides additional information on the light emission vertex. Due to the weighting of signal hits and DCR hits shown from Eq. 5.13, the

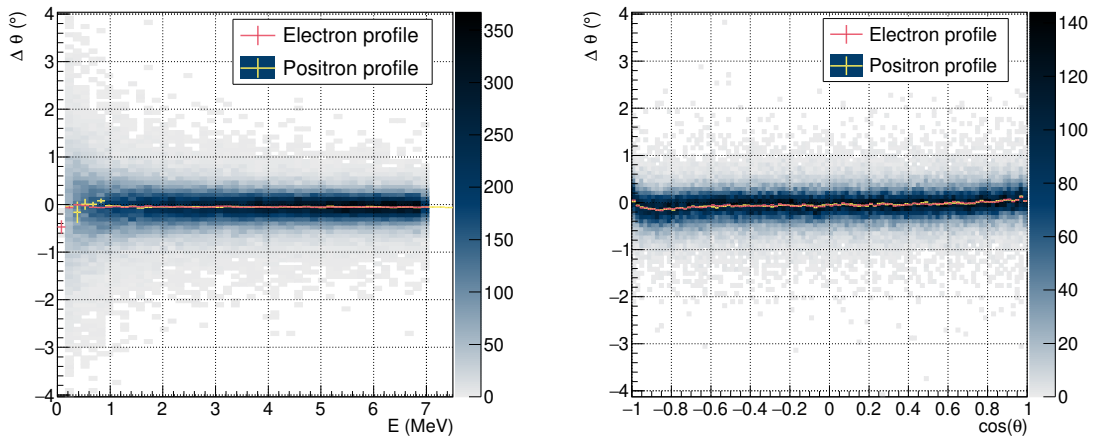

(a) (b)

Figure 5.8: Distribution of the difference $\Delta\theta$ of the reconstructed zenith angle to the simulated zenith angle. The distribution is shown in blue, while the red curve shows the average deviation for electrons and the yellow curve shows the average deviation for positrons. Figure 5.8a shows the distribution in dependence of the deposited energy and Fig. 5.8b shows the distribution in dependence of the simulated zenith angle. Both analyzed samples have simulated kinetic energies from 0 to 7 MeV. To have comparable samples, Fig. 5.8b shows only deposited energies between 1 MeV and 7 MeV.

PMT hit time contribution from the signal is suppressed in the likelihood function in the dark region.

5.4.3 Respective contribution of the charge and time information

To understand the contributions to the performance of the vertex reconstruction, the full log-likelihood function (5.16) was divided into a charge log-likelihood function

$$\ell'_{\text{charge}}(\vec{X}, q_{s,\text{tot}}|\vec{q}) = \ell_{\text{charge}}(\vec{X}, q_{s,\text{tot}}|\vec{q}) + \text{pull}_{\text{charge}}(q_{s,\text{tot}}|q_{\text{tot}}) \tag{5.21}$$

and a time log-likelihood function

$$\ell'_{\text{time}}(\vec{X}, T_0, q_{s,\text{tot}}|\vec{t}, q_{\text{tot}}) = \ell_{\text{time}}(\vec{X}, T_0, q_{s,\text{tot}}|\vec{t}) + \text{pull}_{\text{charge}}(q_{s,\text{tot}}|q_{\text{tot}}). \tag{5.22}$$

Figure 5.11 shows the results of the reconstructions under the use of these log-likelihood functions for the electron sample. The top plots, Fig. 5.11a and Fig. 5.11b, show the resolution of the reconstructed radius against the simulated deposited energy and the bottom plots, Fig. 5.11c and Fig. 5.11d, show these properties against the reconstructed radius.

One can see, that the time reconstruction is largely biased compared to the charge reconstruction, especially at high energies. This hints for an inaccurate description of the time probability shown in Fig. 5.2. One simplification is the missing merging of hits. If multiple

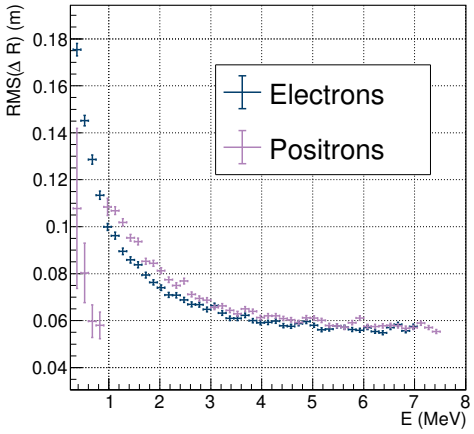

(a)

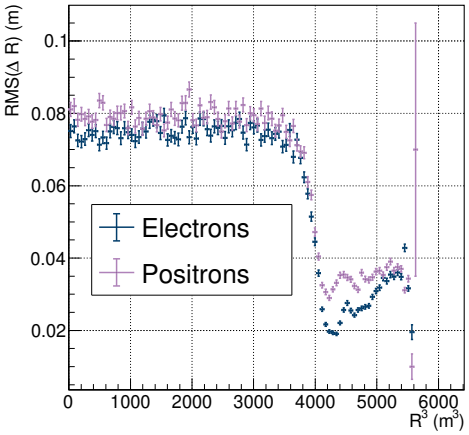

(b)

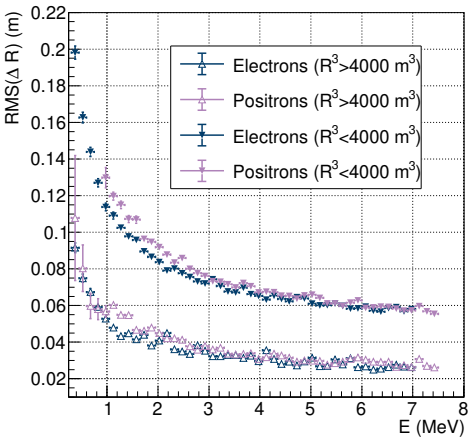

(c)

Figure 5.9: Resolution of the reconstructed radius against the deposited energy (Fig. 5.9a) and the simulated radius (Fig. 5.9b). The resolution is calculated as the sample standard deviation from the distributions shown in Fig. 5.7 for electrons. For the resolution against the radius, events between 1 MeV and 7 MeV were selected to allow the comparison of electrons and positrons. As a the spread drops largely outside of $R^3 < 4000\,m^3$, the resolution against the energy is shown separately for both regions in Fig. 5.9c.

photons arrive at the PMT at about the same time, they can release multiple p.e. at the photo cathode, which lead to a higher measured charge in the PMT. As the probability to have such high-charge measurements increases with the photon flux on the photo cathode, such hits have a sharper time profile than hits measured with a charge of a single p.e. The PMT's, which are close to the light emission vertex, are expected to have more high-charge

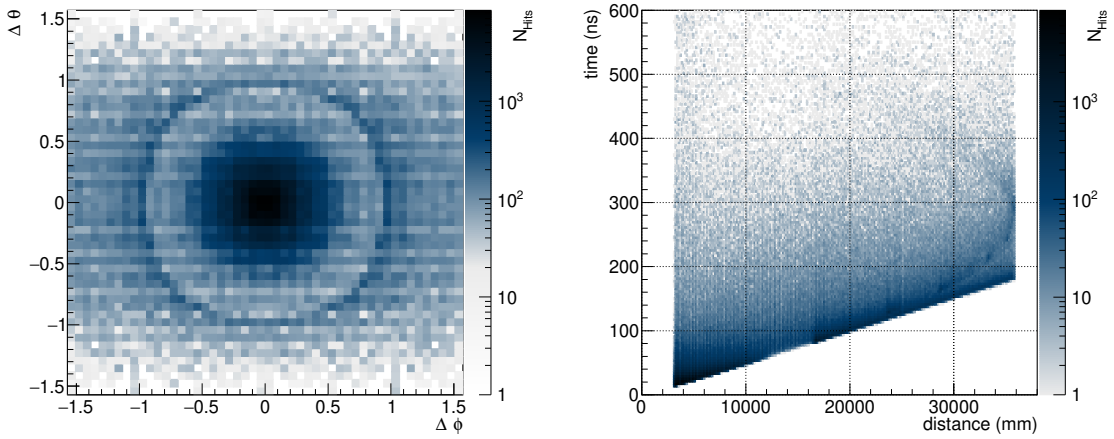

(a) (b)

Figure 5.10: Spatial and time distribution of PMT hits of an example simulation of electrons in the total reflection volume. These histograms were created under the use of the JUNO simulation in the DetSim stage of 100 electrons with 5 MeV at a starting position of $(x, y, z) = (16.32\,\mathrm{m}, 0, 0)$. Figure 5.10a shows the spatial distribution of PMT hits on the PMT array in the difference of the azimuth angle difference ($\Delta\phi$) and the zenith angle difference ($\Delta\theta$) from the PMT to the simulated vertex. Figure 5.10b shows the PMT hit time distribution in dependence of the distance of the PMT to the simulated vertex. The total reflection effect as described in the text is well-visible in both figures.

hits, than PMT's which are farther. As these PMT's are in the direction of the light emission vertex, a positive bias on the reconstructed radius is caused by this effect, which is expected to increase with the simulated radius and the deposited energy.

Another effect, which is described inaccurately in the time fit, is the total reflection on the acrylic sphere. This can be seen in the comparison of the signal time probability map in Fig. 5.2 and the hit time distribution of an example electron simulation in Fig. 5.10b. In Fig. 5.10b, it can be seen that the PMT's in the dark zone have a slightly different time profile than the PMT's outside of the dark zone, as they can not be reached directly by the light. These reflected photons are measured partly later in segments of the *arch*-like structure at high distances and times visible in the hit time distribution in Fig. 5.10b. This *arch* is segmented as the total reflection only occurs for a certain range of angles. The position of the segments on the arch and the position of the dark zone depend on the radius of the light emission point. However, in Fig. 5.2, the arch is not segmented but continuous and the special treatment of the dark zone is missing as it was created as an average over all simulated vertices. A more accurate description of these effects would reduce the bias and improve the resolution of the vertex reconstruction.

Around $R_{\mathrm{TotRef}} \approx 4000\mathrm{m}^3$ and at the edge of the scintillator target, the bias largely reduces in the time fit. As the grid search is not allowed to leave the LS target during the minimization, all events are reconstructed inside the LS target, which reduces the bias and introduces a slightly

negative bias at the edge of the LS target. At R_{TotRef} the total reflection only happens on a thin ring on the acrylic sphere. This creates sharp arch segments of total reflected hits, while there are no total reflected hits at slightly smaller radii. The non-smooth transition from the volume without total reflection to the volume with total reflection gives the reconstruction very precise information on the light emission vertex.

The resolution of the time reconstruction averaged over the simulated radii is better than the charge reconstruction for the whole considered energy range. The main utilized information of the time reconstruction is the position of the emission peak at different distances to the respective PMT. With increasing energies, the occupancy of the PMT array also increases. Without including the sharpening of the hit time probability for high charges in the reconstruction, the time reconstruction can not use more information and its resolution saturates. However, the charge reconstruction can use the additional information by the additional photons, as the measured charge still increases and reduces the relative statistical fluctuations in the measured spatial charge pattern on the PMT array.

It can be seen, that the charge reconstruction has a very bad resolution at small simulated radii and energies. The charge reconstruction finds the light emission vertex mainly by identifying an accumulation of charges as well as the total reflection ring in the spatial charge pattern on the PMT's. These features become more pronounced at high simulated energies and radii and vanish at low simulated energies and radii, where they are hidden behind the statistical fluctuations.

At radii larger than R_{TotRef} the charge reconstruction outperforms the time reconstruction due to the explained ring structure feature in the spatial charge pattern.

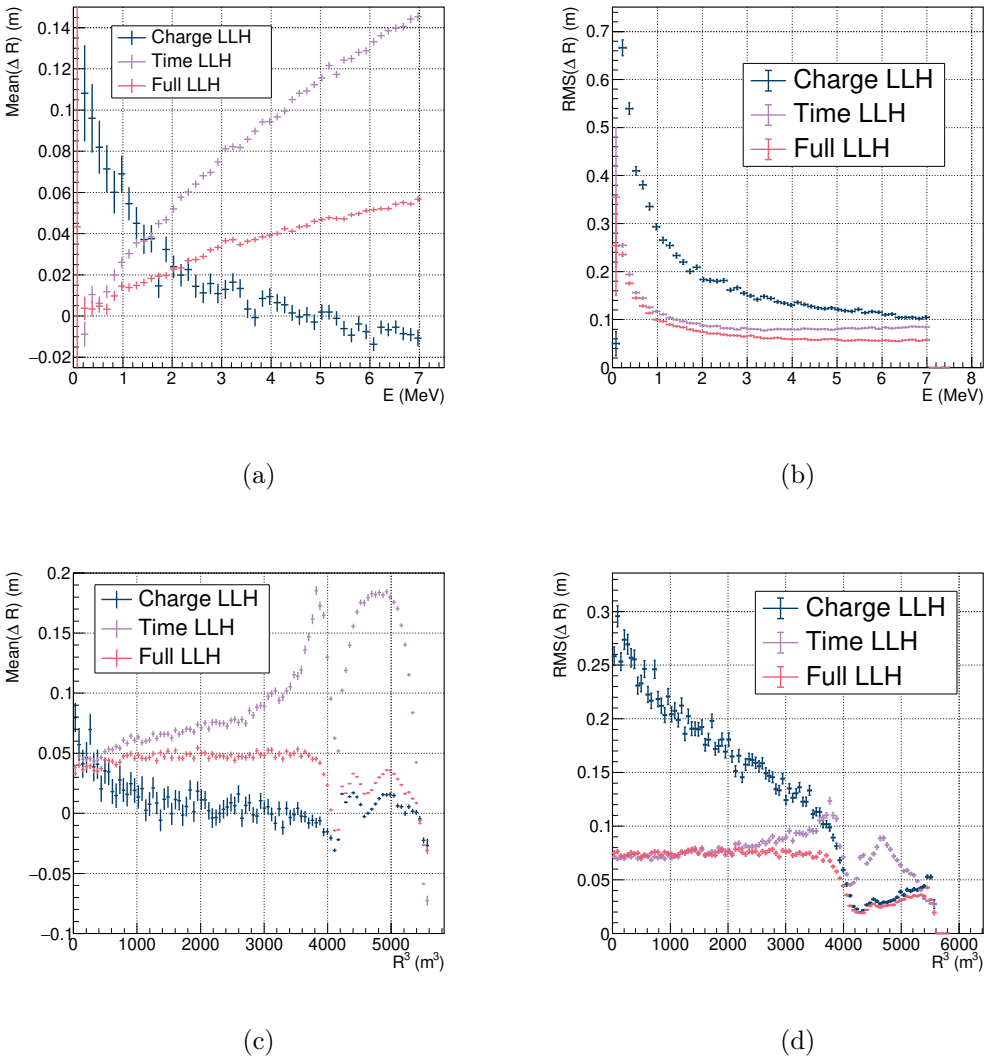

Figure 5.11: Comparison of bias (left) and resolution (right) of the reconstruction using the charge log-likelihood function (Eq 5.21, blue) and the time log-likelihood function (Eq. 5.22, violet) in dependence of the deposited energy (top) and simulated radius (bottom).

5.5 Applications of the vertex reconstruction algorithm

5.5.1 Effect on the energy resolution of JUNO

Non-uniformity effect on the energy resolution

In JUNO, the energy of an event is estimated by the amount of detected light in the detector. As the spectral shape of the prompt events of reactor electron anti-neutrinos is used to determine the MO in the JUNO experiment, an excellent energy resolution is one of the most challenging and crucial requirements for the MO measurement.

The detected amount of light in dependence of the light emission vertex was shown in the expected light non-uniformity map in Fig. 3.10a. To reconstruct the energy of the event, a precise knowledge of the light emission vertex is needed to correct for the light non-uniformity effect. Any uncertainty on the light emission point leads to an additional uncertainty on the reconstructed energy, which is proportional to the local gradient of the non-uniformity map. As it can be seen in Fig. 3.10a, this gradient is especially large in the total reflection region above $R_{\mathrm{TotRef}} \approx 4000\,\mathrm{m}^3$, which leads to the requirement of a very good vertex reconstruction resolution. This section investigates the effect on the energy resolution of the presented vertex reconstruction. In the following $NU(R,\theta)$ denotes the light non-uniformity function extracted by interpolation from Fig. 3.10a. As the light non-linearity is not in the focus of this section, the amount of light and so the visible energy are assumed to be linear with the true deposited energy, such that

$$E_{\mathrm{vis}} \propto E_{\mathrm{true}} \cdot NU(R,\theta). \tag{5.23}$$

Figure 5.12 shows the expected contribution to the energy resolution of an untreated non-uniformity effect. Here, the ratio of visible to true energy is calculated by $E_{\mathrm{vis}}/E_{\mathrm{true}} = NU(R,\theta)/NU(0,\theta)$ for about 100,000 randomly distributed vertices inside the fiducial volume of $R_{\mathrm{FV}} < 17\,\mathrm{m}$. One can see, that the width of the distribution is on the order of 5%. Statistical fluctuations of the amount of detected photons for a single vertex and energy are not taken into account here. As a total energy resolution, including these statistical fluctuations and other effects, is required to be smaller than 3%, the non-uniformity effect needs to be corrected.

The default vertex reconstruction algorithm of JUNO for comparison

To compare the results and show the performance of the presented vertex reconstruction, it is compared to the current default vertex reconstruction algorithm of the JUNO experiment [139, 160]. Also this reconstruction algorithm uses a likelihood function to estimate the vertex of light emission. For this, it corrects the time-of-flight of each first PMT hit and compares its time to charge-dependent pre-calculated probability densities, which were found under the use of a gamma simulation in the JUNO software. There is one probability density function for each measured charge from 1 p.e. to 5 p.e. and each LPMT type. A global uniform DCR time distribution using the average DCR is added to these probability densities. The effective refractive indices of the different materials, which are used to calculated the time-of-flight correction, were optimized to yield a minimal reconstruction bias. Therefore, it can be seen as similar to the presented reconstruction, although there are differences. The main difference is, that the presented reconstruction uses not only hit times, but also charges, which gives it especially an advantage in the total reflection volume. Another difference is the time smearing by the PMT TTS. While the presented reconstruction uses a rather conservative smearing of $\sigma_{\mathrm{Dyn}} = 3.629\,\mathrm{ns}$ and $\sigma_{\mathrm{MCP}} = 6.132\,\mathrm{ns}$, the default JUNO reconstruction uses the expected PMT TTS values. Values of $\sigma_{\mathrm{Dyn}} = 1.15\,\mathrm{ns}$ and $\sigma_{\mathrm{MCP}} = 7.71\,\mathrm{ns}$ are used. For the evaluation of the DCR impact in the default JUNO reconstruction a constant DCR of 30 kHz per PMT was used, while the presented reconstruction uses a measured DCR distribution for all PMT's shown in Fig. 5.5. The average DCR of this measured distribution is with about 38 kHz per PMT slightly higher than the fixed one of the default JUNO reconstruction. Another difference is, that in the presented reconstruction not only first hits, but all hits were selected. Due to the different assumptions on the PMT timing and DCR, one can only roughly compare

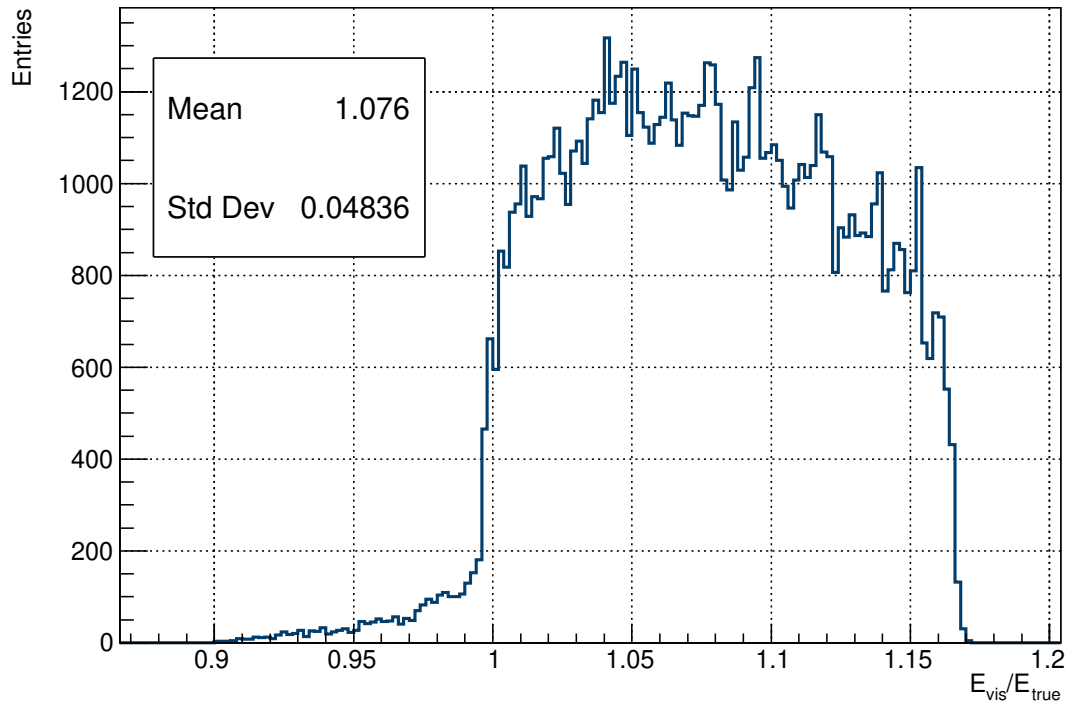

Figure 5.12: The energy smearing if no non-uniformity correction is applied. It was created by taking random distributed vertices inside the fiducial volume of $R_{\mathrm{FV}} < 17\,\mathrm{m}$ and calculating the energy shift according to Eq. 5.23.

both reconstruction algorithms.

The performance of the default JUNO vertex reconstruction is shown in Fig. 5.13[1]. Its resolution is reported by its authors to be nearly constant in all three Cartesian coordinates over the full LS target volume.

While the overall resolution of the default JUNO reconstruction is similar to the presented reconstruction, it is more precise at $R < 4000\,\mathrm{m}^3$ and less precise at $R > 4000\,\mathrm{m}^3$ than the presented reconstruction as one can see in the comparison with Fig. 5.9.

Results on the correction of the light non-uniformity effects

As in Sec. 5.5.1 statistical fluctuations of the amount of photons for a single energy and vertex, as well as light non-linearity effects, are not considered here. To calculate solely the contribution of the non-uniformity effect to the energy resolution, the positron sample from Fig. 5.9 is used. This positron sample is uniformly distributed in the LS target with a uniform kinetic energy distribution from 0 to 7 MeV. To correct the visible energy from Eq. 5.23 for the non-uniformity effect, it is divided by the non-uniformity function at the reconstructed

[1] Unpublished preliminary work by Ziyuan Li. See [139] and [160] for published reports on old versions this algorithm.

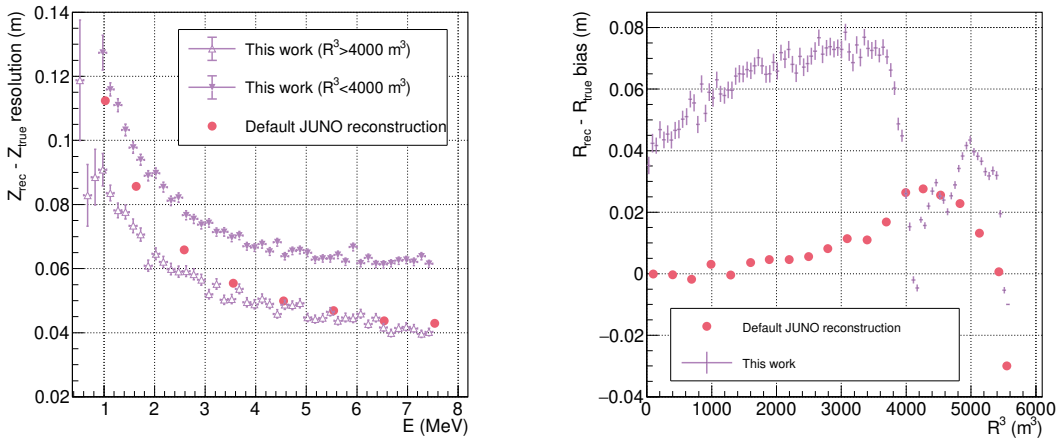

(a) (b)

Figure 5.13: Resolution (Fig. 5.13a) and bias (Fig. 5.13b) of the default JUNO vertex reconstruction algorithm. The resolution is reported to be nearly constant over the full LS target volume. The bias for this reconstruction was found to be energy dependent. The shown bias was evaluated for positrons with 3 MeV momentum. The plots represent unpublished preliminary work from Ziyuan Li.

vertex, giving the reconstructed energy definition for this evaluation:

$$E_{\text{rec}} := \frac{NU(R_{\text{True}}, \theta_{\text{True}})}{NU(R_{\text{Rec}}, \theta_{\text{Rec}})} \cdot E_{\text{true}}. \tag{5.24}$$

Due to the inaccuracy and the limited precision of the reconstructed vertex, this reconstructed energy is expected to form a distribution with a width. This width, estimated by the sample standard deviation estimator, is used here to estimate the contribution of the non-uniformity to the energy resolution.

While for the evaluation of the presented reconstruction the actual reconstructed vertex could be taken, for the default JUNO reconstruction the reconstructed vertex was simulated in a toy simulation. For that, the expected vertex was calculated by adding the bias from Fig. 5.13b to the true simulated vertex. For the smearing, a Gaussian distribution around this biased vertex was assumed for each Cartesian coordinate with the energy-dependent width from Fig. 5.13a. In both reconstructions, the presented reconstruction and the default JUNO reconstruction, the bias was not corrected.

Figure 5.14 shows these resolution in dependence of the energy and the simulated radius. In Fig. 5.14a only events inside the fiducial volume of $R_{\text{FV}} < 17\,\text{m}$ were selected. Both reconstructions show similar results in the region without total reflection. As expected, the default JUNO reconstruction shows a slightly better performance here due to the better vertex resolution and bias in this region. With a photon statistic of about 1300 p.e./MeV in this region and the corresponding relative energy resolution of about $\sigma_E/E \approx 1/\sqrt{1300 \cdot E\,[MeV]} \approx 2.8\%/\sqrt{E\,[\text{MeV}]}$, this additional resolution of less than 0.2% adds only little to the energy

resolution. However, it can be clearly seen, that both reconstructions lead to far worse energy resolutions in the total reflection area due to the high gradient in the light non-uniformity in this region. Due to the very good vertex resolution, the presented reconstruction performs much better in this region. At the maximum around $R^3 = 4200\,\mathrm{m}^3$, and energies between 7 MeV and 8 MeV, energy resolutions of about 0.95% for the default JUNO reconstruction and 0.45% for the presented vertex algorithm were found. With the expected energy resolution from photon statistics of about $\sigma_E/E \approx 1/\sqrt{1450 \cdot 7.5\,\mathrm{MeV}} \approx 1\%$ in this region, the default JUNO reconstruction introduces a similar resolution due to the imprecisions of the event vertex.

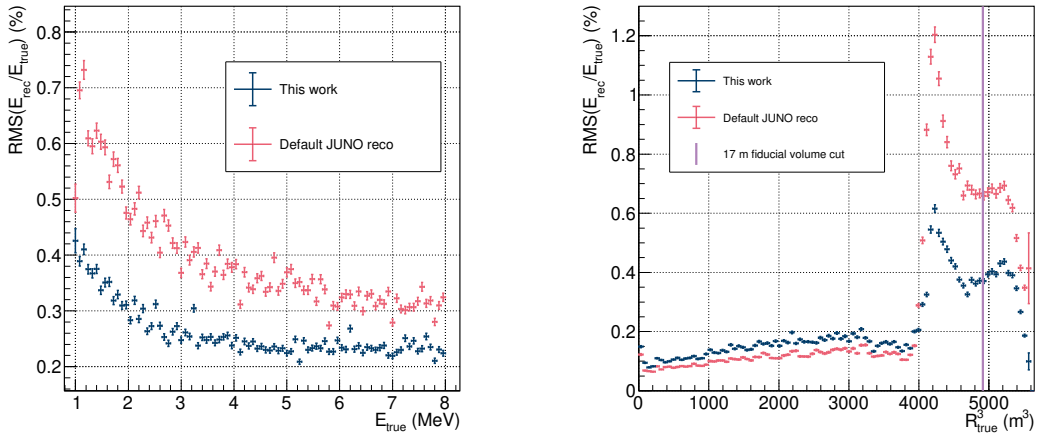

(a) (b)

Figure 5.14: The contribution of the vertex reconstruction performance to the energy resolution. Fig. 5.14a shows the averaged resolution inside the fiducial volume and Fig. 5.14b shows the resolution in dependence of the radius averaged over the shown energies. The large improvement of the presented vertex reconstruction at the total reflection volume is can be clearly seen.

Even with the presented reconstruction and its large improvement in the total reflection volume, the energy smearing introduced by the vertex reconstruction remains large in the total reflection volume. Therefore, if both regions are treated separately in the MO analysis, the sensitivity of JUNO to the MO might improve.

For the presented vertex reconstruction, the bias is similarly large as the resolution. If the bias can be corrected using the calibration data, the results of this section are expected to improve.

5.5.2 IBD directionality in JUNO

An IBD event consists of a prompt positron signal and a delayed neutron signal, which are measured as separate triggered events. In the IBD reaction, the neutron is always emitted in the forward hemisphere of the initial electron anti-neutrino direction [84]. Moreover, in

JUNO, the neutrons are dominantly captured on free protons after a thermal movement of about $\tau \approx 200\,\mu$s with the release of a single gamma in an arbitrary direction. As the accessible information from the vertex reconstruction is the averaged energy deposition information with some uncertainty, the vertex from the neutron capture event is widely smeared and does not need to be reconstructed in the forward direction of the IBD interaction vertex. However, the average displacement of the vertex from the delayed neutron capture event to the vertex from the prompt positron event allows to measure the direction of an incoming electron anti-neutrino flux. Due to the described smearing effects, this method does not work on a single event basis, but requires large event statistics. The feasibility of this method was shown by the CHOOZ experiment [161] and later by the Double Chooz experiment [144] using their collected IBD data from reactor anti-neutrinos. Within a cone of 18°, the CHOOZ experiment was able to reconstruct the average direction of the two nuclear reactors with small event statistics of only about 2500 IBD events, while the reactors have a distance of about 8° from the view of the detector. The directional resolution of an IBD flux of an experiment is expected to improve with the resolution of the vertex reconstruction.

The directionality measurement of IBD events has the potential to be used in several applications. JUNO uses two different power plants with different reactor but similar reactor types. The spectral shape of the reactor electron anti-neutrinos from the Taishan NPP will be monitored by the TAO detector. As such a reference detector is not planned for the Yangjiang NPP, the reactor electron anti-neutrino spectrum from these different reactor cores need to be calculated from reactor core simulations using the measurement from the TAO detector. Due to the high rate of electron anti-neutrinos, directionality could help in identifying the relative contributions from the different NPP's to reduce the systematic uncertainty on the reactor electron anti-neutrino spectrum. Moreover, from the view of the JUNO detector, both NPP's are in the direction of the ocean. Due to the thinner oceanic crust, the geo-neutrino contribution from the oceanic direction is expected to be smaller than from the continental direction. Moreover, while the crust contribution is horizontal, the mantle contribution to the geo-neutrino signal is more vertical. The displacement of the delayed event to the prompt event for other kind of backgrounds is expected to be nearly uniformly distributed. A directionality measurement might reduce the background impact and improve the geo-neutrino measurement in a combined analysis with the spectral analysis of the IBD spectrum.

As being part of the SNEWS system, the JUNO experiment is expected to give out an early warning in the case of an galactic SN burst. This early warning is then sent out to other experiments of the multi-messenger community to make them aware of the SN burst, such that these experiments can adjust for the SN burst measurement. However, telescopes are usually constrained to a certain field-of-view which requires the information of the SN burst direction. The Super-Kamiokande experiment is expected to find the direction of a SN in the galactic center within a cone of 5° opening angle [162]. Due to the IBD channel of the SN burst measurement, the JUNO experiment might be able to constrain the direction of the SN burst using the described technique.

This section presents the possible directional resolution of the IBD flux in the reactor electron anti-neutrino energy range.

Here, the vertex of the prompt event is denoted by $\vec{X}_{\text{prompt}}$ and the vertex of the delayed event of the delayed event is denoted by $\vec{X}_{\text{delayed}}$. This defines the displacement vector for

each event

$$\vec{X}_{\text{d-p}} \coloneqq \vec{X}_{\text{delayed}} - \vec{X}_{\text{prompt}}. \tag{5.25}$$

The direction of the electron anti-neutrino flux is then estimated by taking the direction of the averaged direction vector:

$$\vec{X}_{\text{dir}} = \sum_{\text{all events}} \frac{\vec{X}_{\text{d-p}}}{|\vec{X}_{\text{d-p}}|}. \tag{5.26}$$

To estimate the resolution of the directionality in JUNO under the usage of the presented vertex reconstruction algorithm, 100,000 IBD events following the reactor electron anti-neutrino spectrum without oscillations were simulation using the JUNO simulation software. These IBD events were simulated with an initial electron anti-neutrino direction of $\phi = -1.28976\,\text{rad}$ and $\theta = 1.12296\,\text{rad}$. The positron and neutron direction were calculated following [84]. In the JUNO simulation software in the DetSim stage, an IBD event, consisting of a positron and a neutron, is stored as a single event structure. In the ElecSim stage these events are then splitted into two events due to the time delay and the separated positive trigger signal. The correspondence of the events after the ElecSim stage to the events in the DetSim stage of the JUNO software is not implemented in this version of the software. As a few of these events were lost in the ElecSim stage, this correspondence could not be restored by the event order after the ElecSim stage. To address this issue, the prompt events and delayed events were simulated separately at DetSim stage, such that all IBD interaction vertices are aligned in the detector center. The directionality of the electron anti-neutrino flux was then estimated using Eq. 5.26 with random positron-neutron pairs from these samples. In total 99,103 positron-neutron pairs were evaluated. This method introduces large uncertainties in the resolution of the directionality, since the vertex resolution in the detector center is assumed to be representative for the whole detector. As it can be seen in Sec. 5.4, the performance of the vertex reconstruction is not uniform in the detector making this assumption very approximate. Especially the large improvement in vertex resolution in the total reflection volume is not taken into account in this estimation.

Figure 5.15 shows the full evaluation of the simulated IBD sample with all 99,103 events. It shows the distribution of all displacement directions from Eq. 5.25 evaluated with the true simulated vertices and the reconstructed vertices. The simulated vertex here is again the average vertex of all energy depositions of an event in the LS weighted with the respective deposited energies. In Fig. 5.15, the reconstructed flux directions are marked with red dots, while the true flux direction is marked with a green star. The red ellipses are representing the estimated 1-σ region around the reconstructed vertex.

To estimate the uncertainty on the reconstructed direction, the simulated sample of IBD events was divided into 19 sub-samples with 5000 events each. Afterwards for each sub-sample the direction was reconstructed. The uncertainty for the respective sub-sample size was then estimated by the sample standard deviation of the angle between the true flux direction and the reconstructed flux direction, assuming this distribution to be centered around the true electron anti-neutrino direction $\vec{\phi}_{\bar{\nu}_e}$:

$$\sigma_{\text{Dir}} = \sqrt{\frac{1}{N-1}\sum_{i}^{N} \sphericalangle\left(\vec{X}_{\text{dir},i}, \vec{\phi}_{\bar{\nu}_e}\right)^2}, \tag{5.27}$$

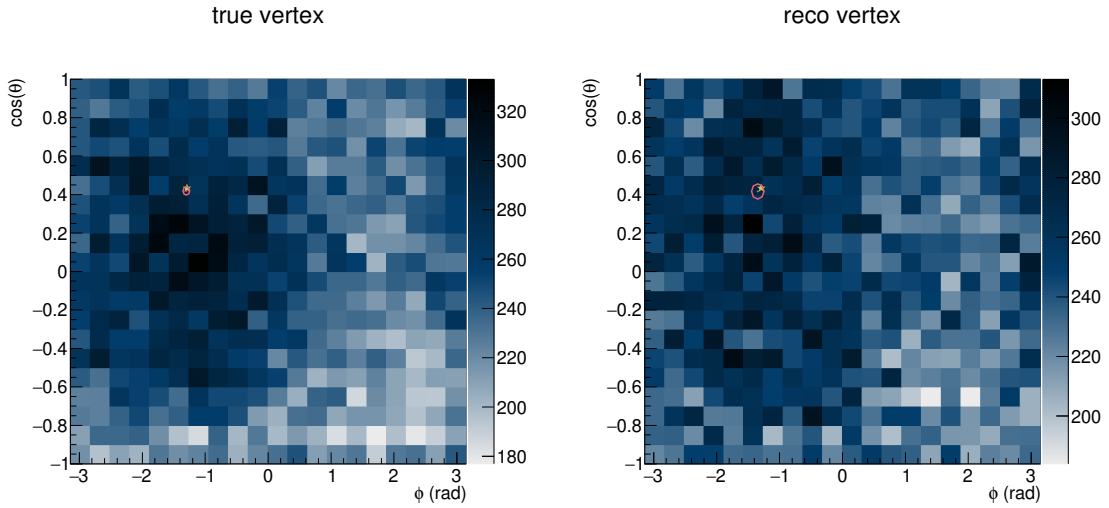

(a) (b)

Figure 5.15: The directionality reconstruction with 99.103 IBD events. The left side (Fig. 5.15a) shows the reconstruction of the direction using the simulated vertices and the right side (Fig. 5.15b) uses the reconstructed vertices. Both histograms show the distribution of obtained displacement directions between delayed and prompt event from Eq. 5.25. The direction of the electron anti-neutrino flux is marked with a green star, while the respective reconstructed direction from Eq. 5.26 is marked with a red dot. The 1-σ region from Eq. 5.29 or Eq. 5.30, respectively, is marked with a red ellipse.

with $N = 19$ being the amount of sub-samples. The uncertainty on the resolution is estimated with the standard error:

$$\mathrm{SE}(\sigma_{\mathrm{Dir}}) = \frac{\sigma_{\mathrm{Dir}}}{\sqrt{2 \cdot N - 2}} \tag{5.28}$$

A dependence of the directionality resolution on the number of events of $\sigma_{\mathrm{Dir}} = a/\sqrt{N}$ is assumed. The directionality resolution under the use of the reconstructed vertices can be estimated with

$$\sigma_{\mathrm{Dir,Rec}} = \frac{(25.1 \pm 4.2)^\circ}{\sqrt{N_{\mathrm{events}}/5000}}. \tag{5.29}$$

With the usage of the simulated vertices instead of the reconstructed vertices, one can estimate a lower limit for the resolution with this method of

$$\sigma_{\mathrm{Dir,Sim}} = \frac{(13.6 \pm 2.3)^\circ}{\sqrt{N_{\mathrm{events}}/5000}}. \tag{5.30}$$

Double Chooz defines its uncertainty on the reconstructed direction as the half-aperture of the cone around the true direction, which contains 68% of all reconstructed directions for each sample. Using this definition, Double Chooz estimates its directional resolution to be less than 10° for about 8000 IBD events [163]. If this definition of uncertainty can be assumed to be comparable, Double Chooz has a much better resolution on the flux direction. Using the results from this work, one would obtain a resolution of $(10.7 \pm 1.8)^\circ$ at 8000 IBD events with

the use of the simulated vertices, neglecting the smearing of the vertex reconstruction. The directionality resolution with the use of the reconstructed vertices is worse by about a factor of 2 in this work. An advantage of Double Chooz is here the capture of neutrons on Gadolinium for the delayed event of the IBD detection. Gadolinium has a much higher cross section for the capture of neutrons than Hydrogen. This minimizes the thermal movement of the neutrons before the capture and allows a better preservation of the directionality information.

Chapter 6

Reduction of the ^{14}C-Background

As shown before in Sec. 3.6.1, due to the large volume of the JUNO detector and the implied high amount of Carbon atoms in the LS, the pile-up background caused by ^{14}C decays, is one of the major backgrounds in JUNO. Due to the low endpoint energy of ^{14}C decays, they do not cause a trigger and therefore do not contribute to the event rate unlike other backgrounds. The JUNO experiment determines the MO from the structure of the fast oscillations in the prompt spectrum of the IBD measurement as shown in Fig. 3.11. To separate the oscillation maxima, an unprecedented precision on the spectral shape for reactor neutrino experiments is needed. Under the occurrence of ^{14}C decays in the detector, pile-up events are formed. Pile-up events are here defined as triggered events, which contain PMT hits from different energy depositions in the detector. Especially pile-up events, which contain PMT hits, caused by an initial positron from the IBD reaction, and PMT hits, caused by a ^{14}C decay are in the focus of this chapter. The piled-up event spectrum can be calculated by convoluting the prompt spectrum with the ^{14}C spectrum. This smears out the energy of the prompt event and worsens the effective energy resolution.

Figure 6.1 shows the stacked distributions of PMT hit times of a pile-up event in a DAQ window. It shows the PMT hits caused by a positron with a deposited energy of 2.1 MeV at (x,y,z)=(0.23 m, 3.43 m, 2.42 m) in violet and the hits caused by a ^{14}C decay with a deposited energy of 76 keV at (x,y,z)=(-3.31 m, 15.13 m, -1.12 m) in red. Additionally, the PMT hits caused by dark counts are shown in orange. The positron and the ^{14}C decay are both simulated with the JUNO simulation software. In the histogram, the reconstructed hits from the PMT pulses are shown. In this event, 2265 PMT hits are caused by the positron, while the ^{14}C decay caused 108 PMT hits and 825 PMT hits are dark counts. In this typical example, the number of PMT hits without dark counts, which is the main information used to reconstruct an initial reactor electron anti-neutrino, would be biased by about 5%, if the ^{14}C decay could not be identified.

Due to its large size and the requirement of a precise and accurate reconstructed reactor electron anti-neutrino energy, the JUNO experiment is expected to be strongly impacted by ^{14}C pile-up. As shown in Eq. 3.2 and Eq. 3.13, the pile-up rate in JUNO assuming the requirement of a $^{14}C/^{12}C$ ratio of 10^{-17} is about 5%. This chapter introduces methods which can tag pile-up events to reduce their impact on the MO measurement. These are a simple and fast clusterization algorithm, which is performed before other reconstruction algorithms,

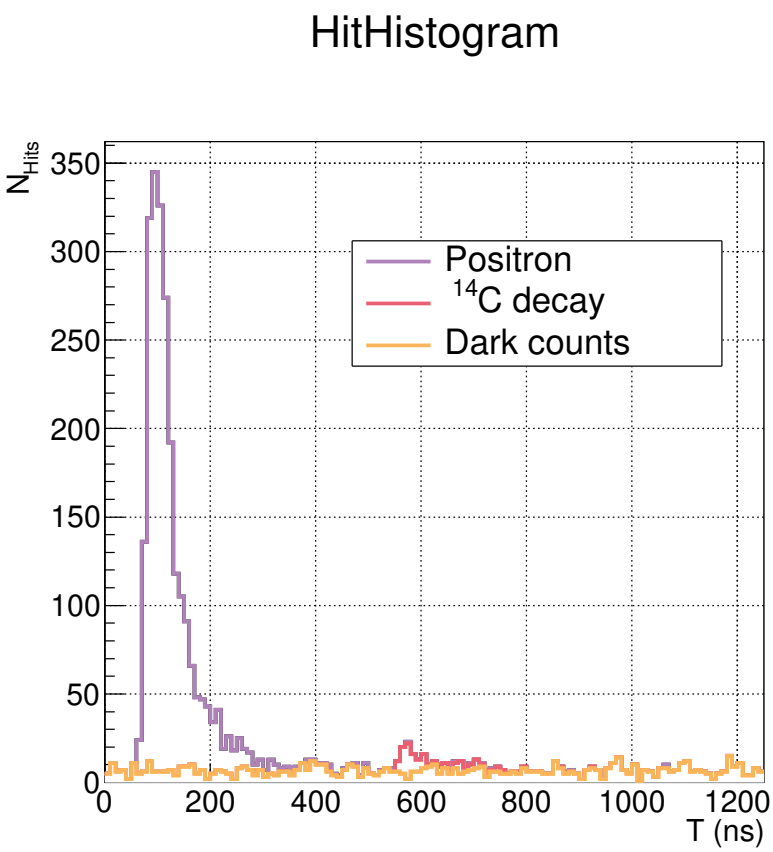

Figure 6.1: Example PMT hit time distribution of the full DAQ window of a pile-up event with PMT hits caused by a positron (violet), a ^{14}C decay (red), and dark counts (orange).

and a likelihood test under the use of the vertex reconstruction presented in Chapter 5. As the clusterization algorithm can not separate different energy depositions, which overlap in the PMT hit time distribution, the likelihood test can be used complementary to find such pile-up events.

6.1 Clusterization

If a positive trigger decision is stated by the DAQ system of JUNO, all PMT hits around this trigger decision in the defined DAQ time window of 1250 ns are stored as a single DAQ event. This DAQ window is preliminary chosen to conservatively contain all PMT hits from a triggered event in a large energy range. As the LS time profile has a long tail, the DAQ window is chosen asymmetrically from -100 ns before the trigger time until 1150 ns after the trigger time. The clusterization algorithm has the purpose to find the time region, called *cluster*, in the DAQ window, which contains the PMT hits from a single energy deposition. This cluster can be then used by other reconstruction algorithms to constrain their hit selection to reduce the influence of background PMT hits. While these background PMT hits

are typically dark counts, these could also be caused by another energy deposition in the LS in pile-up events. These pile-up events can be identified by the clusterization algorithm by the identification of multiple clusters in one DAQ window. Therefore, the clusterization algorithm is performed after the PMT pulses are reconstructed and before other reconstruction algorithms are performed.

This section introduces a clusterization algorithm. Due to the high rate of ^{14}C decays, the majority of pile-up events are formed with ^{14}C decays. Therefore, this section focuses the on the ability to identify ^{14}C decays in pile-up events with IBD positrons. The parameters of the clusterization algorithm are optimized on the improvement on the MO sensitivity of JUNO with the identification of pile-up events of the prompt events from the IBD spectrum with ^{14}C decays.

6.1.1 Algorithm

To identify a cluster in the hit time distribution, the hit time distribution is first smoothed using a sliding window. In this sliding window with the width of T_{win} the number of all PMT hits around a central time t_c in the interval $-T_{\text{win}}/2 < t_c < T_{\text{win}}/2$ are counted in order to average out statistical fluctuations yielding the summed value $s(t_c)$. The central time t_c is moved in steps of 1 ns from the start of the DAQ window to the end of the DAQ window and the corresponding hit counts s_i are saved for each step i with the time t_i^c.

During these iterations, a cluster is found by an excess of the s_i over the expected amount of dark counts. If the amount of counted hits exceeds a threshold value N_T, a cluster is formed. Therefore, this threshold is called here the *trigger threshold*. It is calculated using the algorithm parameter z_T, which can be understood as the Poissonian equivalent to a deviation by $z_T \cdot \sigma$ from the mean of a Gaussian distribution. From z_T the cumulative probability $P_G(z_T)$ of a normal distribution is calculated in the interval of $(-\infty, z_T)$:

$$P_G(z) \coloneqq \int_{-\infty}^{z} \frac{1}{\sqrt{2\pi}} e^{-\frac{1}{2}x^2}. \tag{6.1}$$

To find the threshold number of hits $N_T(z_T)$, the smallest possible number of hits is taken with the Poissonian cumulative probability equal to or larger than $P_G(z_T)$:

$$N_T(z_T) = \min(\mathcal{N}(z_T)) \quad \text{with} \quad \mathcal{N}(z) = \{n \in \mathbb{N} : \sum_{k=0}^{n} \frac{(\lambda_{\text{DCR,win}})^k}{k!} e^{-k} \geq P_G(z)\}, \tag{6.2}$$

with the expected amount of dark counts in the sliding window $\lambda_{\text{DCR,win}}$. The first bin which satisfies this condition will be called *trigger bin* in the following with its center at the time T_T.

While the excess over this threshold defines the existence of a cluster, another threshold is used to define the borders of the cluster. This threshold N_B is called here the *baseline threshold* and is calculated in the same way as the trigger threshold with the parameter z_B:

$$N_B(z_B) = \min(\mathcal{N}(z_B)). \tag{6.3}$$

The start time of the cluster T_s is found by the time bin smaller than N_B closest to the trigger bin with a smaller time than T_T. The end time of the cluster T_e is found in the same way

by the time of the first bin smaller than N_B with a larger time than T_T. A cluster is forced to not exceed the start time and the end time of the DAQ window, such that $T_s \geq 0$ and $T_e \leq 1250\,\text{ns}$ for the given DAQ window time of 1250 ns with the start at 0 ns.

After one cluster is successfully found and constrained, the algorithm continues to search for the next cluster by searching for an excess of s_i over N_T. This search is performed in the remaining bins after the end time of the first cluster. The search for more clusters is continued until the end of the DAQ window is reached. For a senseful clusterization, the trigger threshold parameter z_T should be always larger than the baseline threshold parameter z_B.

Using this algorithm, it is not possible to find an overlap of multiple different clusters. As the same condition on the number of hits is used for the start condition and the end condition, the bin which was found to be the end time of the first cluster has an less PMT hits than N_B. If a second cluster would be found, the earliest start time of it would be the end time of the first cluster as it also requires to have less hits than N_B.

Figure 6.2 shows the summed PMT hit time distribution of the simulated event shown in 6.1. In Sec. 6.1.4, the optimization procedure of the clusterization parameters will be described. For the illustrative purposes of Fig. 6.2, the optimized parameters of $z_T = 5.0$, $z_B = 0.7$, and $T_{\text{win}} = 50\,\text{ns}$ are used. With the applied DCR distribution, an amount of 33.93 dark counts is expected to fall within this window. In Figure 6.2a, the summed hit time distribution of the full DAQ window is shown. The trigger threshold of $N_T = 67$ is shown is marked in green and the baseline threshold $N_B = 38$ is shown in red. Moreover, the identified clusters are marked with blue-bordered boxes. These boxes start at the identified cluster start times of 39 ns and 531 ns and end at the identified cluster end times of 434 ns and 737 ns. Figure 6.2b shows a zoom of Fig. 6.2a in the region of the identified clusters. One can see, that both clusters are constrained at the points where the summed PMT hit time distribution falls below the baseline threshold N_B. In the comparison with Fig. 6.1 one can see, that both energy depositions from the positron and from the ^{14}C decay could be identified.

6.1.2 Simulation of pile-up events

For the simulation of pile-up events, the JUNO simulation was used. Here, the impact of pile-up of positron events from IBD reactions of reactor electron anti-neutrinos with ^{14}C decays is in the focus. Therefore, a positron simulation with 200,000 events with kinetic energies from 0 to 11 MeV, uniformly distributed in the JUNO detector, was created. The electrons emitted in ^{14}C decays were also simulated under the use of the JUNO detector. They follow the theoretical predicted β-decay spectrum as implemented in the radioactive decay mode of the Geant4-software [135, 136] with the decay energy of $Q = 156.475\,\text{MeV}$. To create a pile-up event from both simulations, the PMT hits from a random simulated ^{14}C decay were shifted by a random time and added to the PMT hits from a positron. In this adding of hits, the merging of hits which would occur in the readout electronics is neglected. For each pile-up event the true number of energy depositions in the DAQ window is evaluated by the amount of energy depositions which caused at least a single PMT hit inside the DAQ window. If a high time shift was drawn, it is likely, that no PMT hits from the ^{14}C decay fall inside the DAQ window. Such an event is treated as a pure positron event, while the events with PMT hits from two sources are tagged as pile-up events. Additionally to the PMT hits from energy depositions in the LS, like in Chapter 5, dark counts were added individually for each PMT

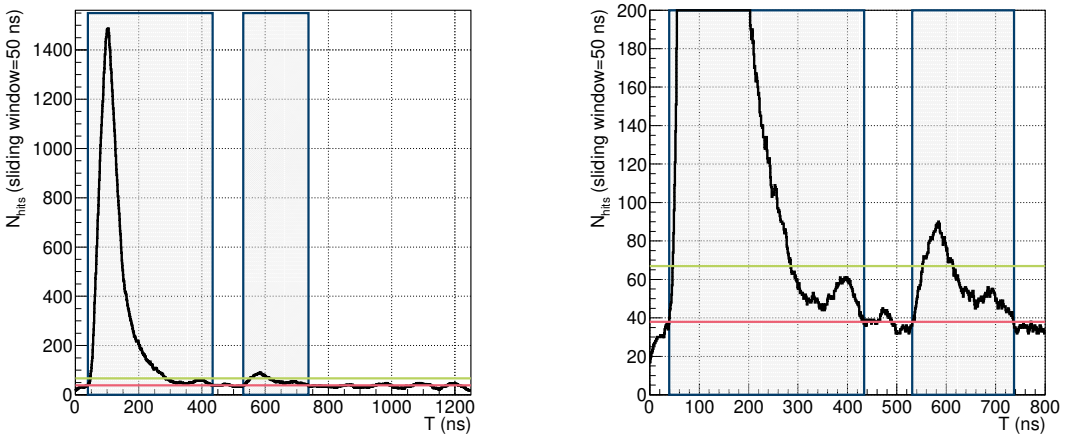

(a) (b)

Figure 6.2: A clusterized summed PMT hit time distribution for the demonstration of the clusterization algorithm. The trigger threshold of $N_T = 67$ hits, corresponding to $z_T = 5.0$, is shown in green and the baseline threshold $N_B = 38$, corresponding to $z_B = 0.7$, is shown in green. Moreover, the identified clusters using these thresholds are shown with blue-bordered boxes.

following a Poissonian distribution with the expectation value for each PMT following the measured DCR distribution in Fig. 5.5.

6.1.3 Performance on removing ^{14}C pile-up events

To estimate the performance of the clusterization algorithm regarding the identification of ^{14}C pile up events in the prompt spectrum, it was evaluated in a grid of clusterization parameters. The trigger threshold parameter z_T is varied here from 3 to 7 in steps of 0.5, the baseline threshold parameter z_B is varied from -1.5 to 1.3 in steps of 0.2, and the sliding window length is varied from 30 ns to 70 ns. For each point on this grid the full positron simulation was evaluated. Like described in Sec. 6.1.2, a pile-up event was created from each positron with one ^{14}C decay with a random shift from 0 to 1400 ns, while only hits inside the DAQ window from 0 to 1250 ns are considered. As the random shift can be higher than the end of the DAQ window, a large fraction of events is expected to contain only hits from the positron and DCR. These events are used to get a better understanding on the forming of clusters from dark counts in absence of signal hits in pure positron events.

For each set of clusterization parameters, several efficiencies were evaluated. To understand the misidentification of clusters, the efficiency to reconstruct a pure positron event as a single cluster event is evaluated. For the identification of pile-up events, the efficiency to identify a pile-up event as an event with two clusters evaluated. Under the use of a window length of 50 ns, a cluster trigger threshold of $z_T = 5.0$ and a baseline threshold of $z_B = 0.7$, the efficiency to reconstruct a pure positron event as a single cluster event was evaluated to be

99.78% and the efficiency to reconstruct a pile-up event as a two-cluster event was evaluated to be 23.62% for positrons between 5 MeV and 6 MeV deposited energy. These are the optimized parameters from the optimization, which will be introduced in Sec. 6.1.4. As the evaluated efficiencies depend on the energy of the positron, the efficiencies were evaluated separately for each positron energy interval of 1 MeV from 1 MeV to 11 MeV.

Figure 6.3 shows the evaluated efficiencies for all evaluated clusterization parameters on the grid. Here, the term *signal efficiency* describes the efficiency to reconstruct a pure positron event as a single cluster event. The term *background efficiency* describes the efficiency to reconstruct a pile-up event, consisting of PMT hits from one positron and one ^{14}C decay, as a two cluster event. For this figure, the trigger threshold and the baseline threshold were divided into different sets according to their conservativeness. The green points show the evaluations with a high trigger threshold in the evaluated range of $z_T \geq 5.5$ and and low baseline threshold of $z_B \leq -0.7$. The violet points show clusterization parameters in the range of the evaluated parameters of $4.5 \leq z_T \leq 5.0$ and $-0.5 \leq z_B \leq 0.5$ and the red points show evaluations with a low trigger threshold of $z_T \leq 4.0$ and high baseline threshold of $z_B \geq 0.7$. One can see, that for a conservative set of clusterization parameters a signal efficiency of 100% can be reached on the cost of identifying less ^{14}C decays. This is reached via the usage of a high trigger threshold and a low baseline threshold. The high trigger threshold minimizes the amount of misidentified clusters and the low baseline threshold ensures, that an event is not split into two clusters by PMT hit fluctuations in the long tail of the LS time profile in the PMT hit time distribution. If the clusterization parameters are chosen to be less conservative, the higher amount of misidentified clusters causes the signal efficiency to drop, but the background efficiency to increase. A lower trigger threshold allows the detection of ^{14}C decays with a lower β energy. Moreover a higher background threshold causes the clusters to be shorter. This allows a larger window for the search of multiple clusters in the event, but also cause more misidentified clusters from fluctuations of the amount of PMT hits in the tail of high energy events.

For a better understanding the performance of the clusterization, the background efficiency was evaluated against the time difference of the positron contribution and the ^{14}C decay contribution as well as the β energy of the ^{14}C decay. Both evaluations are shown in Fig. 6.4. Also here, the evaluation for the optimized parameters of $z_T = 5.0$, $z_B = 0.7$, and $T_{\text{win}} = 50$ ns for an energy range from 2 MeV to 3 MeV is shown. The plot in Fig. 6.4a shows the ratio of pile-up events which were identified as two clusters to all pile-up events in blue, while the ratio of pile-up events where only one cluster or more than two clusters were identified to all pile-up events is shown in blue. The shown efficiency uncertainties of the ratio of k successes divided by n total entries are evaluated by

$$\sigma\left(\frac{k}{n}\right) = \sqrt{\frac{(k+1)(k+2)}{(n+2)(n+3)} - \frac{(k+1)^2}{(n+2)^2}}, \tag{6.4}$$

from [164]. The label $T_{14C} - T_{e+}$ was calculated by the difference of the first PMT hit time from the ^{14}C decay to the first hit time of the positron. One can clearly see, that for low time differences both contributions in the PMT hit time distribution overlap and can not be identified as separate clusters. For time differences larger than about 400 ns, one can see that first ^{14}C clusters can be identified. The maximum efficiency is reached for time differences between about 600 ns to about 1000 ns, where about 45% of the ^{14}C decays can be identified as

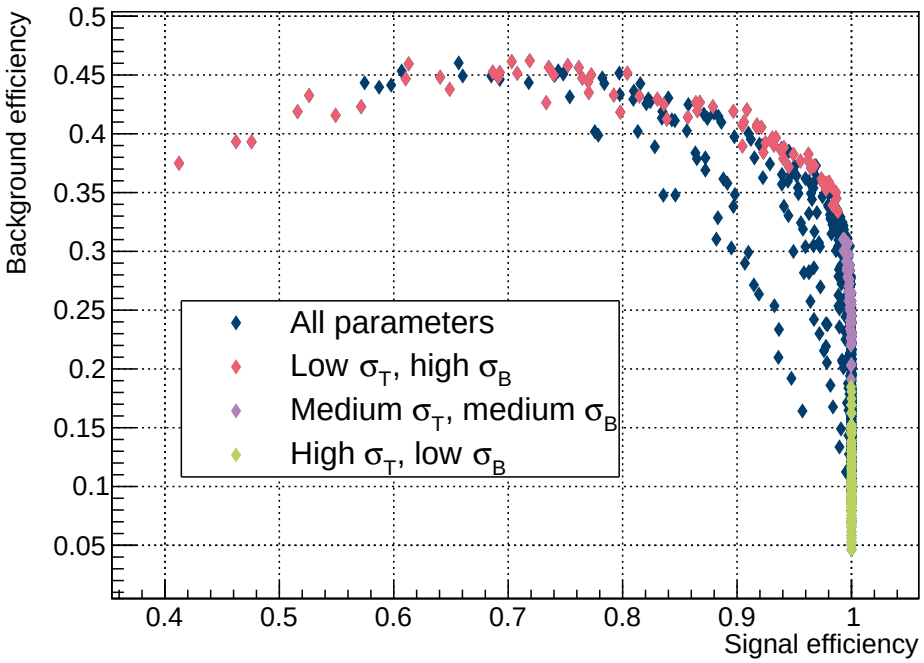

Figure 6.3: The efficiency to reconstruct a pure positron event as one cluster (signal efficiency) against the efficiency to reconstruct a pile-up event with one positron and one ^{14}C decay as a two-cluster event (background efficiency). Three groups of evaluated points are highlighted, whose exact definition can be found in the text. One can see from the highlighted points, that a high trigger threshold with a low baseline threshold yields a high signal efficiency with a low background efficiency, while a lower trigger threshold with a higher baseline threshold can reach higher background efficiencies on the cost of a lower signal efficiency.

clusters. For larger time differences above 1000 ns the efficiency drops again as large fractions of the PMT hits from the ^{14} decay move outside the DAQ window.

In Figure 6.4b, the ratio is shown of the spectrum of ^{14}C decays which were found in two-cluster events in blue to the total ^{14}C β-spectrum. Additionally, the complementary ratio of the spectrum of ^{14}C decays, which were not tagged to the full ^{14}C β-spectrum. This efficiency is parameterized with an empirical function based on the Fermi-Dirac distribution:

$$\epsilon(E_{14C}) = \frac{a}{\exp\left(\frac{E_{14C}-E_F}{E_T}\right)+1} + b. \tag{6.5}$$

This function is supposed to describe the transition of the efficiency from low β energies, where the ^{14}C decay can not be found to high ^{14}C energies, where some ^{14}C decays are found. The parameter a describes the difference of the value of the curve at low β energies and high energies and the parameter b describes the value at high β energies. The transition between these plateaus is parametrized by E_F, which is the middle point of the transition and

E_T, which describes the width of the transition. For the given curve, the parameter values were fitted to be $a = 0.575 \pm 0.013$, $b = 0.428 \pm 0.012$, $E_F = (0.0498 \pm 0.0008)\,\mathrm{MeV}$, and $E_T = 0.0075 \pm 0.0005\,\mathrm{MeV}$.

Figure 6.4c shows the time difference dependence of the ^{14}C tagging efficiency for β energies of ^{14}C decays larger than 0.08 MeV. One can see, that for sufficiently large time difference and β energies from the ^{14}C decay, the ^{14}C decay can be reliably found.

6.1.4 Optimization of the clusterization parameters on the MO sensitivity of JUNO

For the optimization of the clusterization algorithm two effects need to be balanced: These are the potential to find clusters from low energy events, such as from ^{14}C decays against the false identification of DCR over-fluctuations as clusters. This is done by optimizing it on the sensitivity of the MO of JUNO under the assumption of a conservative rejection strategy. If an event is identified by the clusterization algorithm as pile-up event, it is rejected as whole, as it is assumed in this strategy, that all PMT hits from the full DAQ window are needed to minimize the bias of the energy reconstruction. This is also done to ensure a conservative set of clusterization parameters, without the selection of a high rate of clusters, caused by DCR over-fluctuations. Such misidentified clusters from DCR over-fluctuations would directly reduce the total event statistic of JUNO and therefore reduce the sensitivity to measure the MO. Besides that, a high efficiency of identifying ^{14}C decays would improve the sensitivity as the reconstructed IBD energy spectrum becomes more precise. The MO sensitivity is evaluated using the GNA software [20].

GNA framework for estimating the JUNO MO sensitivity

The *Global Neutrino Analysis* (GNA) software is developed by JINR, Dubna to provide a tool to conveniently estimate sensitivities and analyze the data from neutrino experiments [20, 21]. For this, it is able to form and minimize χ^2-functions for given experiment models and estimate the sensitivities of a given experiment model under the use of an *Asimov* data-set [165].

The version of GNA used in this thesis uses a simplified model of the reactor electron anti-neutrino measurement of JUNO. For the prediction of the IBD rate due to reactor anti-neutrinos, it uses the Huber+Mueller model [48, 49] for the flux with the IBD cross section from [84]. For the reactor flux it uses the contribution from the six reactor cores at the Yangjiang NPP and also all four reactor cores of the Taishan NPP with their GPS distances to the detector. Additionally, the reactor electron anti-neutrinos from the far Daya Bay NPP, as well as from the Huizhou NPP are considered. For all reactors a fuel composition of 60% ^{235}U, 27% ^{239}Pu, 7% ^{238}U, and 6% ^{241}Pu is assumed. This estimation of the reactor electron anti-neutrino flux is nowadays outdated, as the Taishan NPP is currently expected to be realized with only two of the originally four planned reactor cores and the realization of the Huizhou NPP is postponed. Moreover, a detection efficiency of 80% is assumed. For the effect of neutrino oscillations, the full three-flavor model is used with the oscillation parameters from [166]. For the toggling of the mass hierarchy for the sensitivity estimation in GNA, the parameter Δm^2_{ee} is introduced, which was originally used to describe two flavor oscillations.

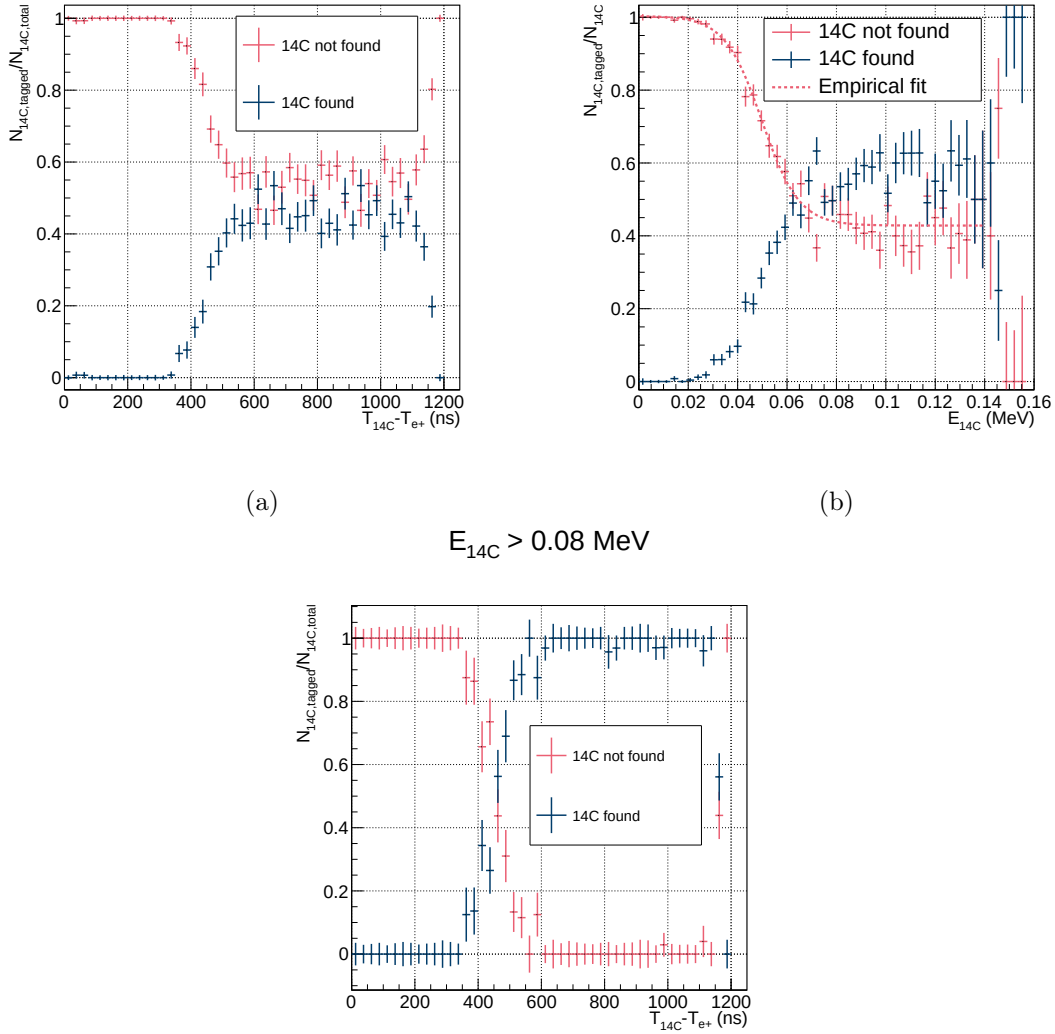

Figure 6.4: The efficiency of the clusterization algorithm to find a ^{14}C decay in dependence of the time difference between the ^{14}C decay and the positron (Fig. 6.4a) and the efficiency against the energy of the ^{14}C decay (Fig. 6.4b). The time difference is here the difference between the first PMT hits from the respective contribution in the PMT hit time distribution extracted from the simulation output. Figure 6.4c shows the efficiency against the time difference for a sub-sample with ^{14}C decay energies larger than 0.08 MeV.

It is defined in GNA by the following relations:

$$|\Delta m^2_{32}| = \Delta m^2_{ee} + \eta \cdot (\sin^2\theta_{12} - 1) \cdot \Delta m^2_{12} \tag{6.6}$$

$$|\Delta m^2_{31}| = \Delta m^2_{ee} + \eta \cdot \sin^2\theta_{12} \cdot \Delta m^2_{12}, \tag{6.7}$$

with $\eta = 1$ for NO and $\eta = -1$ for IO. If the MO is changed to the other possibility, this

Δm^2_{ee} is kept constant and Δm^2_{32} and Δm^2_{31} are calculated accordingly.

On the calculated reactor electron anti-neutrino spectrum, the energy resolution of JUNO is applied. For the energy resolution the so called *a-b-c-model* is implemented [11]:

$$\frac{\sigma_E}{E} = \sqrt{\left(\frac{a}{\sqrt{E}}\right)^2 + b^2 + \left(\frac{c}{E}\right)^2}, \tag{6.8}$$

with the default values of $a = 3\%\sqrt{\text{MeV}}$, $b = 0$, and $c = 0$.

Being the largest background, the geo-neutrino background is added in GNA.

Optionally, a smearing caused by the pile-up of ^{14}C decays can be added in GNA [167], which will be described in the next section. This smearing is applied before the spectrum is smeared by the energy resolution effect.

For the estimation of the MO sensitivity of JUNO, an Asimov data-set for the JUNO model of a certain MO is constructed. For this data-set, two χ^2 functions are created for each MO possibility, respectively. These χ^2 functions are then minimized with Δm^2_{ee} as minimization parameter and the difference, called $\Delta\chi^2_{\text{MO}}$, is used to estimate the sensitivity to the MO quantitatively, like it is described in Sec. 3.6.1 and Eq. 3.12. Here, the Asimov data was created with the IO JUNO model. The creation of Asimov data with the NO JUNO model was checked for the case of no ^{14}C and no clusterization and leads to the same values of $\Delta\chi^2_{\text{MO}}$. As Asimov data with the IO inserted is used, the minimization of the corresponding χ^2 function with the IO JUNO model is expected to yield $\chi^2_{\text{min}} = 0$.

Figure 6.5 shows both, the expected JUNO spectrum for the assumption of the NO in red and for the IO in blue for the case of no energy resolution effects and with the default energy resolution of $3\%/\sqrt{E/\text{MeV}}$. Additionally, the difference of the NO spectrum and the IO spectrum is shown in violet. One can see, that the measurement of the difference between NO and IO requires a precise energy resolution, due to the small differences of the neutrino oscillation peaks.

^{14}C pile-up effect in GNA

To estimate the smearing effect of pile-up with ^{14}C decays, it is included in the JUNO model of GNA [167]. For the application of the smearing effect, the IBD prompt spectrum is partially convoluted with the ^{14}C spectrum. To reach a higher precision in the application of the smearing, each bin in the energy spectrum is divided into five uniform sub-bins for that. For the used 700 bins from 1 MeV to 10 MeV, each sub-bin has a width of about 2.6 keV. Based on the used DAQ-window length of 1250 ns and the concentration of ^{14}C, the coincidence probability for the creation of a pile-up event is calculated. For the default ^{14}C concentration of ^{14}C/^{12}C=10^{-17}, the coincidence probability is 5%, like shown in Eq 3.13. This coincidence probability is used to calculate the pile-up fraction of each sub-bin. To apply the effect of ^{14}C pile-up, this fraction of each sub-bin is moved to the next range of sub-bins according to the ^{14}C spectrum. As the energy spectrum of ^{14}C decays starts at 0, a fraction of these events is not moved, but stays in the same sub-bin. After the iteration over all sub-bins, the original bins are reformed with the new sub-bins.

Figure 6.6 shows the difference in each bin of the spectrum without the effect of ^{14}C pile-

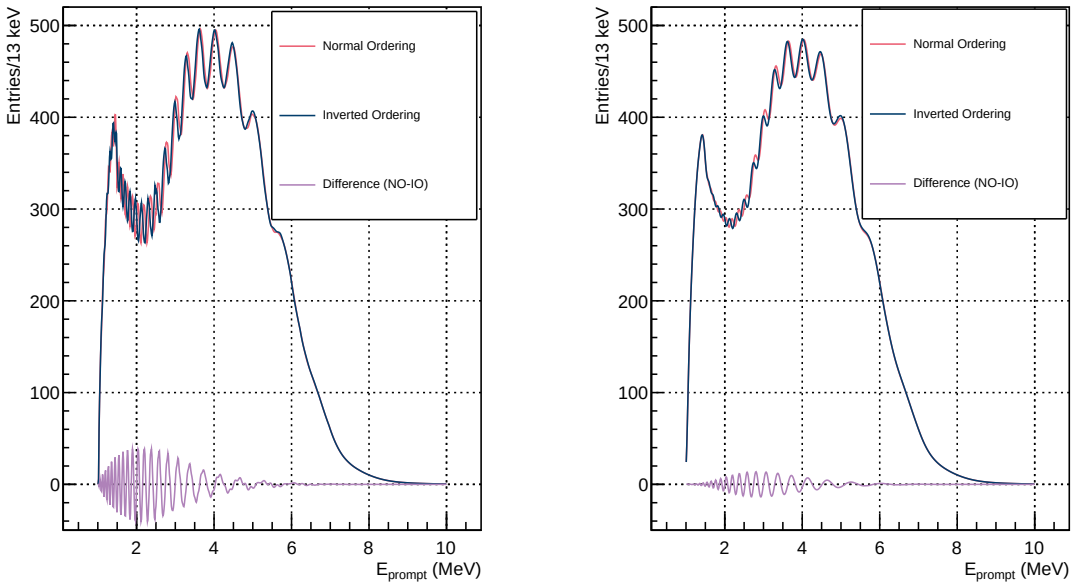

Figure 6.5: The IBD prompt spectrum as it is calculated in the GNA software. The left side shows the case of no energy uncertainties and the right side shows the case of the default energy resolution of $3\%/\sqrt{E/\mathrm{MeV}}$. On both sides, the red line shows the spectrum with the assumption of NO and the blue line shows the spectrum with the assumption of IO. The difference of the red line to the blue line is shown in both plots in violet. No statistical fluctuations are applied to the spectra. The shown spectra have 700 bins from 1 MeV to 10 MeV. The spectrum contains about 150,000 events.

up to the spectrum including this effect for a ^{14}C concentration of 10^{-17} ^{14}C atoms per ^{12}C atom. The distribution of events from a bin over a range of bins with different energies causes the smearing effect, which leads to a worse sensitivity to the MO. As an input parameter to calculate the smearing, GNA uses the ^{14}C concentration as the ^{14}C/^{12}C ratio.

Effects of clusterization on the ^{14}C pile-up effect in GNA

Under the assumption of the mentioned strategy of rejecting each event with more than one cluster, this strategy, using the clusterization algorithm, has several effects on the IBD spectrum, including ^{14}C pile-up events, like described in Sec. 6.1.3. In the implementation of the clusterization algorithm into GNA, three effects regarding the pile-up identification are implemented. One effect is, that the amount of piled-up ^{14}C decays is reduced by the identification of multiple clusters in an pile-up event, which is implemented as a decrease of the coincidence probability due to the evaluated background efficiency. As the potential of the clusterization algorithm to identify a ^{14}C decay as cluster depends on the energy of the electron of the ^{14}C decay, the effective spectrum of piled-up ^{14}C decays changes after

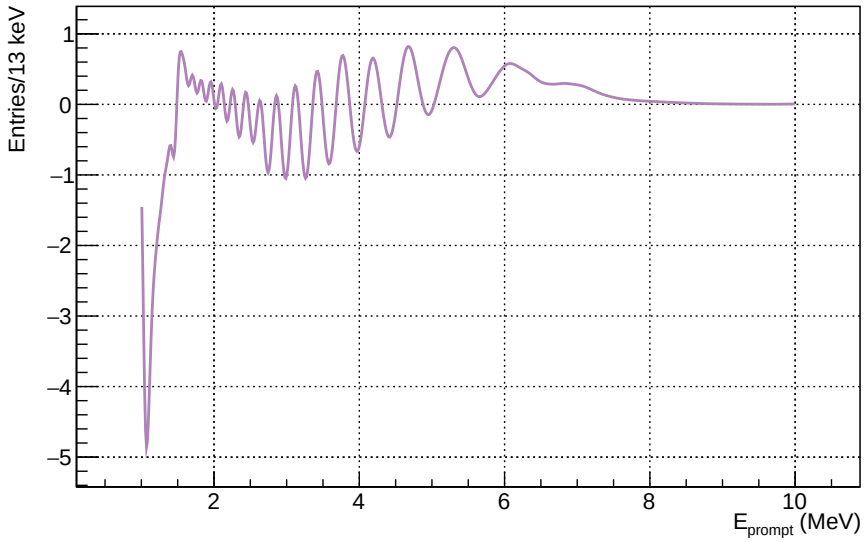

Figure 6.6: The difference of the spectrum with the pile-up effect of ^{14}C to the spectrum without the pile-up effect as implemented in the GNA software. For this figure, the JUNO model with NO with an energy resolution of $3\%/\sqrt{E/\mathrm{MeV}}$ is used. The total spectrum without the effect of ^{14}C pile-up is shown on the right side of Fig. 6.5 in red. Here, a ^{14}C concentration of 10^{-17} ^{14}C atoms per ^{12}C atom was assumed as stated in the requirements of the JUNO experiment [11].

clusterization. Here, the empirical parametrization using Eq. 6.5 is used. To calculate the effective piled-up ^{14}C spectrum, Eq. 6.5 is multiplied to the β spectrum of ^{14}C, which is re-normalized afterwards.

Another effect is the loss of IBD signal events. Especially for low values of z_T, it can often happen, that an DCR over-fluctuation is identified as another cluster, additionally to the positron cluster. As an event with multiple clusters, it is also rejected. Moreover, IBD signal events are lost due to the identification of a ^{14}C decay cluster additionally to the positron cluster. Also here, due to the conservative optimization strategy, the full event is rejected, including the positron, which reduces the statistic in the IBD spectrum.

To include these effects in GNA, look-up tables were created, which contain the signal efficiency, the efficiency to tag pile-up events, and the parameters of Eq. 6.5 for each of the grid points presented in Sec. 6.1.3, separated in positron energy intervals of 1 MeV each from 1 MeV to 11 MeV. To estimate a parameter on these maps between two energy values, the parameter values of the values of the adjacent energies are interpolated linearly.

Optimization results and estimated improvement on the MO measurement

To optimize the clusterization parameters, the sensitivity of JUNO with the simple JUNO model in the GNA software is evaluated for all points on the grid of parameters, presented in Sec. 6.1.3.

The sliding window duration T_{win} needs to be optimized to be sufficiently long enough to avoid statistical DCR fluctuations. If it is too long, the increased amount of dark counts in the window reduces the significance of the PMT hits from the ^{14}C decay. If it is too short, only parts of the PMT hits from the ^{14}C decay are inside the sliding window at each position, which also reduces the statistical significance of the ^{14}C decay. One would expect the optimized sliding window duration to be about the same size as the peak duration in the ^{14}C decay PMT hit time distribution. Here, the sliding window which provides the maximal sensitivity was found to be 50 ns. Moreover, if the same events would be used for the scan, one would not expect more than one maximum in this plot. If a ^{14}C decay would be found with a high value of z_T it would be also found with a lower value of z_T in the exact same event. The same applies for the misidentification of DCR clusters. However, one can see slight variations in the scan. These stem from the way, the analyzed events are created. While the PMT hits from the positron and the ^{14}C decay are read from a file, and also the used time shift values between the positron and the ^{14}C decay are the same, the contribution by the DCR was randomly assigned for each analyzed event. This causes the positron PMT hits and the ^{14}C decay PMT hits to be the same in each evaluation for each bin of Fig 6.7, but the DCR PMT hits to fluctuate. Due to these fluctuations the amount of misidentified DCR clusters can vary for each iteration, as well as the amount of identified ^{14}C decays, as a low energetic ^{14}C decay can only be found with a time-coincident underlying DCR over-fluctuation.

The two-dimensional grid of z_T and z_B for $T_{\text{win}} = 50$ ns is shown in Fig. 6.7. Here, the evaluated $\Delta\chi^2_{\text{MO}}$ value is shown against the clusterization parameters z_T and z_B. For reference, the value of $\Delta\chi^2_{\text{MO}}$ without the effect of ^{14}C pile-up was calculated to be 11.54 and the value with ^{14}C pile-up, but without clusterization, was calculated to be 10.83. In the overlayed bin content numbers of Fig 6.7b one can identify a region at about $z_T \approx 5.0$ and $z_B \approx 1.0$ with the highest $\Delta\chi^2_{\text{MO}}$ values of $\Delta\chi^2_{\text{MO}} \approx 11.00$. Due to the aforementioned uncertainties in this map and the simplicity of the evaluated JUNO model, these rounded values of $\Delta\chi^2_{\text{MO}} = 11.00$ in the scan are assumed to show no significant difference to each other. As a low value of z_B corresponds to a longer, more conservative cluster length, here the value of $z_T = 5.0$ and $z_B = 0.7$ is chosen as the optimized value, which yields $\Delta\chi^2_{\text{MO}} = 11.00$, an improvement of 0.17 to the case without clusterization. Around the maximal region, one can observe an asymmetric behavior of the $\Delta\chi^2_{\text{MO}}$ value. For small values of z_T, a high amount of misidentified clusters are found. These lower the overall statistics of the IBD spectrum as multiple cluster events are rejected and cause the $\Delta\chi^2_{\text{MO}}$ to drop drastically. This effect is stronger for large values of z_B, as the cluster of positron PMT hits is shorter and partially truncated. Fluctuations in the tail of the positron PMT hit time distribution are here the major cause of additional clusters. For large values of z_T, the probability misidentification of clusters, which cause the rejection of pure positron events, drops significantly. Increasing values of z_T cause an increasing energy threshold for the identification of ^{14}C decays, which causes a drop in the efficiency to find low energetic ^{14}C clusters. Also here, low values of z_B cause the cluster duration of positron PMT hits to be longer, which does not allow the tagging of ^{14}C decays which are too close in time. Similar maps for different sliding window durations T_{win} can be found in Appendix C.

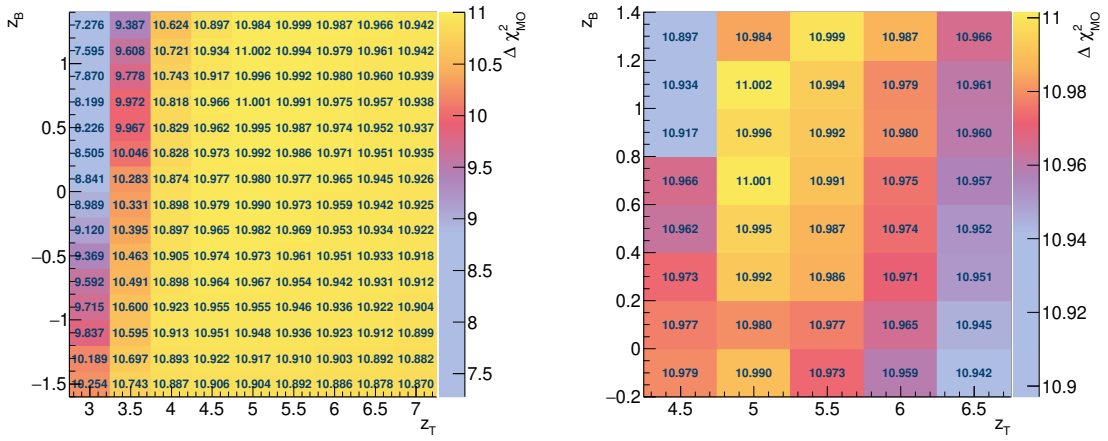

Figure 6.7: Scan of the MO sensitivity of JUNO quantified as $\Delta\chi^2_{\mathrm{MO}}$ for varying clusterization parameters z_T and z_B. Here, a sliding window duration T_{win} of 50 ns was chosen as it contains the maximal $\Delta\chi^2_{\mathrm{MO}}$ value. Fig. 6.7a shows the full scan of the threshold parameters, while Fig. 6.7b shows the region with the maximal $\Delta\chi^2_{\mathrm{MO}}$ values.

In this optimization of the clusterization parameters, the concentration of ^{14}C in the detector of 10^{-17} ^{14}C atoms per ^{12}C atom was assumed, as it is the stated requirement of the JUNO experiment in [11]. The amount of ^{14}C in the LS depends solely on the age of the petroleum, which is used in the LS production and can not be reduced with the planned purification methods, described in Sec. 3.2.1. The value of the concentration of ^{14}C in the LS was not precisely measured so far. Therefore it is interesting to estimate the impact of the ^{14}C for different concentrations of ^{14}C in the LS. Figure 6.8 shows the impact of the ^{14}C pile-up on the MO sensitivity of JUNO for the given JUNO model. Here, the required ^{14}C concentration of $^{14}\mathrm{C}/^{12}\mathrm{C}{=}10^{-17}$ is shown as a dashed line. For the estimation of the sensitivity, different curves for different assumptions are shown. The violet line shows the assumption of no ^{14}C in the LS and can be seen as the upper limit for the improvement of the methods for the reduction of the ^{14}C pile-up effect. The red line shows the effect of ^{14}C pile-up without clusterization, while the green and the blue line show the evaluation of the ^{14}C pile-up effect including clusterization with different assumptions. The green line uses the conservative strategy which was also used to optimize the clusterization parameters. Here, an event, in which two or more clusters are identified, is rejected. For high concentrations of ^{14}C in the LS, Fig. 6.8 can only be seen approximate. In the evaluation of the impact of clusterization, only pile-up events with a single ^{14}C decay were considered. For an increasing ^{14}C concentration this assumption looses its validity. However, also for low concentrations, the sensitivity estimations here can only be seen approximate as the used JUNO model lacks complexity. The results on the sensitivity need to be validated under the use of a comprehensive JUNO model with recent assumptions.

The rejection strategy of this analysis was chosen to ensure a conservative set of clusterization parameters. This clusterization should be able to detect low-energetic energy depositions, such

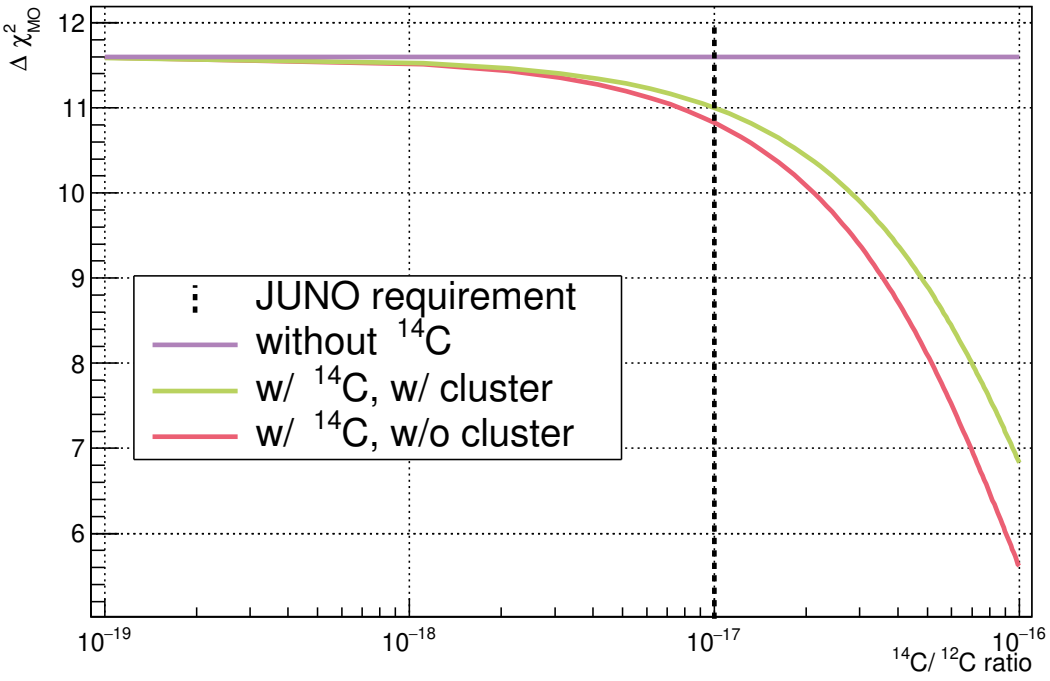

Figure 6.8: Estimation of the impact of ^{14}C pile-up on the MO sensitivity of JUNO for different ^{14}C concentrations.

as ^{14}C decays, while it avoids a high rate of clusters from DCR over-fluctuations. As shown in Sec. 6.1.3 the clusterization algorithm does not find a ^{14}C decay, if it is either overlapped with another energy deposition or it has a low energy, which causes too less PMT hits to increase over the trigger threshold of the clusterization algorithm. If the PMT hits from a positron of the IBD prompt spectrum inside a cluster are sufficient to reconstruct the energy with the required precision and accuracy, the MO sensitivity can be further improved by analyzing all reconstructed clusters instead of full events. This would increase the IBD statistics again, as the positron events are not rejected in the case of a second cluster. Moreover, the ^{14}C decays which occur timely separated, but with too low β energy to be detected by the clusterization algorithm, would be also removed in such a case, leaving the energy bias from ^{14}C pile-up in overlapping energy depositions.

6.2 Likelihood test using the vertex reconstruction

In Chapter 5, a method was presented, which finds the best estimate for the position of the light emission, the amount of signal charge, and the global event time under the assumption of a detector response model formulated in a likelihood function. This likelihood function includes the time distribution of the PMT hits as well as the charge distribution of the PMT hits in dependence of the event vertex on the PMT array. The likelihood function is constructed with the assumption, that the event contains only a single energy deposition at a single point-like

vertex in the detector. In the case of a ^{14}C pile-up event, this assumption does not hold as PMT hits are added by the ^{14}C decay at times and PMT positions, which are independent of the positron energy deposition. These additional PMT hits are expected to cause a tension to the positron PMT hits, which results in higher minimized values of the likelihood function. The discrimination using the values of a likelihood function is typically called *likelihood test*.

As the likelihood function is expected to have also different values for different energies and vertices of pure positron events, this effect needs to be corrected, before it can be used to discriminate ^{14}C pile-up events. For that, the vertex reconstruction was performed on a positron sample with energies from 0 to 11 MeV, uniformly distributed in the detector, mixed with ^{14}C decays as introduced in Sec. 6.1.2. As not only PMT hits from ^{14}C decays are expected to have a strong contribution to the minimized likelihood function, but also late dark counts, the positron sample was clustered using the optimized parameters of $z_T = 5.0$, $z_B = 0.7$, and $T_{\text{win}} = 50\,\text{ns}$. Only PMT hits inside the cluster were considered, which reduces the contribution of late dark count hits. The full sample, containing about 150,000 events, was divided into about 85,000 pure positron events, which contained only PMT hits from the positron and dark counts in the analyzed cluster and a mixed sample with about 65,000 events, which contained also additionally at least one PMT hit from the ^{14}C decay in the analyzed cluster. From the pure clusterized positron sample, maps for the expected likelihood value were created separately for the charge likelihood function (Eq. 5.10) and the time likelihood function (Eq. 5.15). These maps contain the average likelihood value divided by the number of hits in the cluster, as well as the spread of it calculated by the sample standard deviation, in dependence of the vertex reconstruction outputs of the reconstructed radius R_{rec} and the reconstructed total signal charge $q_{s,\text{tot}}$ as introduced in Chapter 5. The maps for the charge likelihood function are shown in Fig. 6.9, while the maps for the time likelihood function are shown in Fig. 6.10.

For the evaluation of the likelihood increase of pile-up events, both pile-up events and events without pile-up were clustered and their likelihood function minimized. The evaluated minimized time and charge likelihood value was then corrected using the value from Fig. 6.9 or Fig. 6.10, respectively:

$$\ell_{\text{corr}} = \frac{\ell - \langle \ell \rangle \left(R^3, q_{s,\text{tot}}\right)}{\sigma(\ell)(R^3, q_{s,\text{tot}})} \tag{6.9}$$

Using these corrected likelihood values, a discriminator can be formulated to reject pile-up events. Here, the 2D-distance of the corrected charge likelihood values and corrected time likelihood values from the center of the distribution from the pure positron sample is used. Due to the subtraction of the mean value from each point, the distribution of corrected likelihood values is centered around 0. One obtains for the discriminator:

$$\Delta L^2 = \ell^2_{\text{charge.corr}} + \ell^2_{\text{time,corr}} \tag{6.10}$$

Figure 6.11 shows the rejection potential of this discriminator. Here, the full sample In the Figures. 6.11a and 6.11b, the one-dimensional distributions of the corrected charge likelihood values and the corrected time likelihood values are shown. Figure 6.11c shows the two-dimensional distribution of the corrected likelihood values. One can see for the pure positron sample, that the values of the corrected charge likelihood and time likelihood are slightly correlated. This correlation stems from the weighting of PMT hits in the time likelihood in

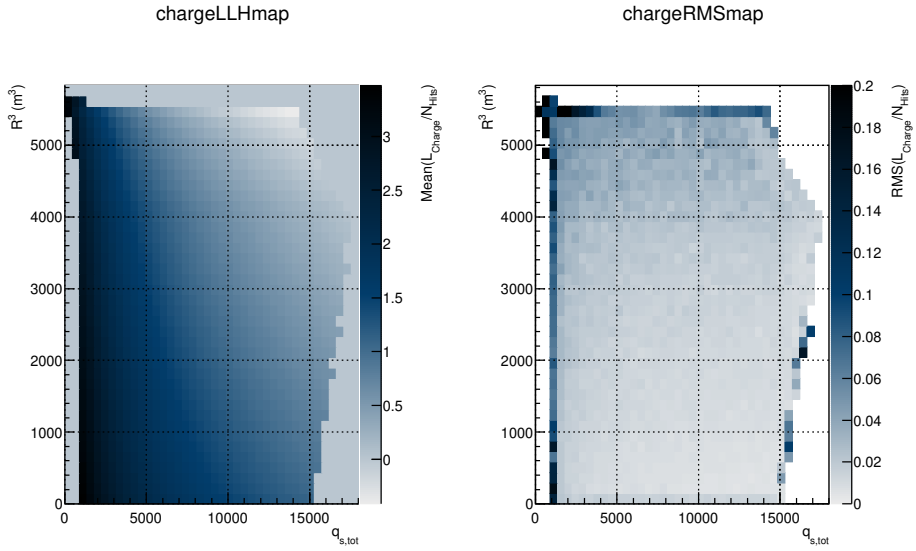

Figure 6.9: Average values (left) and spread (right) of the charge likelihood function divided by the number of PMT hits in the analyzed cluster against the reconstruction outputs of the reconstructed cubed radius R^3 and the reconstructed signal charge $q_{s,\mathrm{tot}}$. Here, about 85,000 clusterized positron events with kinetic energies from 0 to 11 MeV are used for the creation of the maps.

Eq. 5.13. In this equation, the PMT hit time distribution is weighted with the PMT hit time distributions from the signal and DCR to the respective fraction of expected PMT hits. This fitting of the charge fractions in the time likelihood function introduces a correlation between the charge likelihood value and the time likelihood value, which is impeding the discrimination of pile-up events here. Equation 6.10 calculates the difference of each point to the center of the blue distribution in Fig. 6.11c. One can see, that a large fraction of pile-up events is showing a large distance to the center of the blue distribution due to their large values of ℓ_{Charge} and ℓ_{Time}. This leads to the discrimination strategy of rejecting events with ΔL^2 greater than a cut value. The results of this discrimination are shown in Fig. 6.11d. Using this value, one can reach $(99.89 \pm 0.01)\%$ signal purity (blue curve) while rejecting $(13.74 \pm 0.14)\%$ of pile-up events (red curve) using a cut value of $\Delta L^2 = 20$.

In this section, only pile-up events were considered, which could not be separated by the clusterization algorithm, as they overlap in the PMT hit time distribution. Using only the hits inside the cluster for the later analysis, $(51.91 \pm 0.18)\%$ of the ^{14}C decays are already rejected, as they occur outside the positron cluster. In combination with the likelihood test, in total $(58.52 \pm 0.17)\%$ of all ^{14}C decays can be rejected with the cut value of $\Delta L^2 = 20$, while $(99.89 \pm 0.01)\%$ of the positron events can be kept.

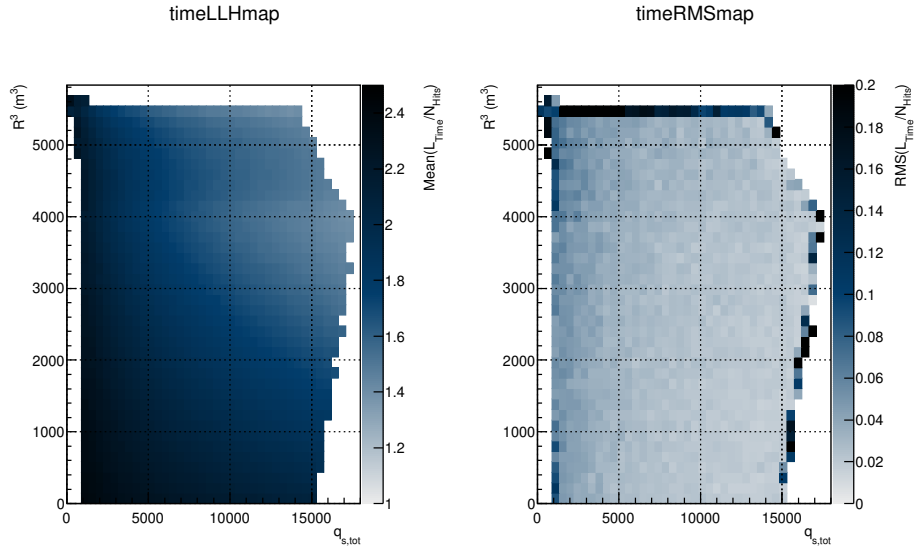

Figure 6.10: Average values (left) and spread (right) of the time likelihood function divided by the number of PMT hits in the analyzed cluster against the reconstruction outputs of the reconstructed cubed radius R^3 and the reconstructed signal charge $q_{s,\mathrm{tot}}$. Here, about 85,000 clusterized positron events with kinetic energies from 0 to 11 MeV are used for the creation of the maps.

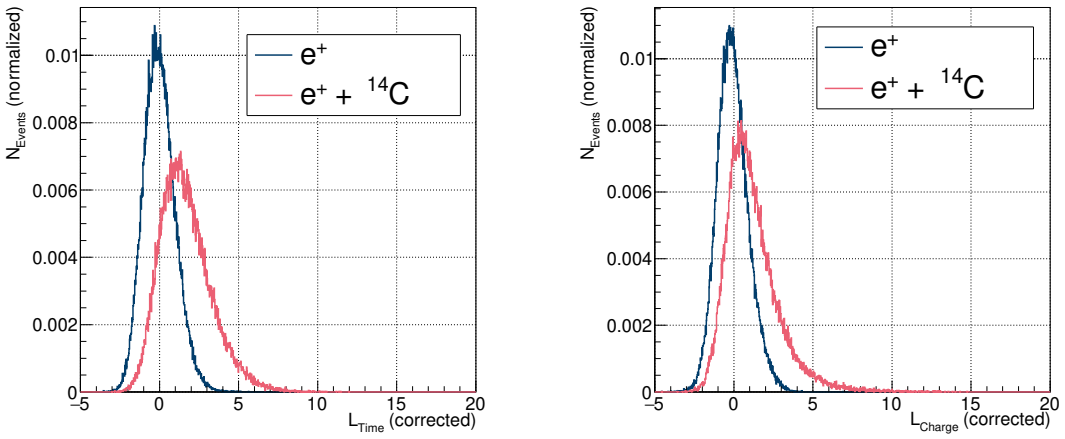

(a)

(b)

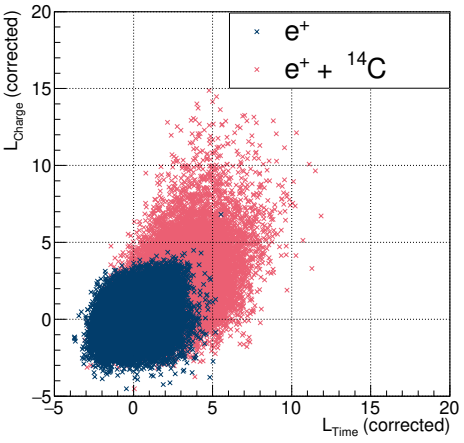

(c)

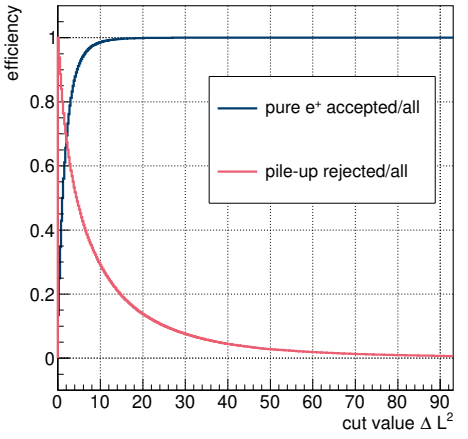

(d)

Figure 6.11: The rejection potential of the likelihood test of the vertex reconstruction. One can see in the top figures, Fig. 6.11a and Fig. 6.11b, the one-dimensional distributions of the average- and spread-corrected likelihood values of the charge part and the time part of the likelihood function used in the vertex reconstruction. The pure positrons (signal) are shown in blue, while pile-up events (background) are shown in red. The respective two-dimensional distribution can be seen in Fig. 6.11c. Using the discriminator of Eq. 6.10, one can reach the rejection potential shown on Fig. 6.11d. Here, the fraction of accepted signal is shown in blue, while the rejected background is shown in red.

Chapter 7

Conclusion and Outlook

For its main goal, the measurement of the Neutrino Mass Ordering with reactor electron anti-neutrinos, the JUNO experiment requires an unprecedented energy resolution of 3% at 1 MeV and a sub-percent accuracy on the energy scale [11]. Besides an appropriate detector design, a meticulous data analysis is needed to ensure that the JUNO experiment can meet these requirements. In this thesis, three analyses are presented to aid the knowledge on the energy of the measured positrons from Inverse Beta Decays of reactor electron anti-neutrinos.

As the accurate knowledge of the non-linearity is crucial for JUNO, it is of imminent importance to develop a good model for the light non-linearity of positrons. In Chapter 4, a non-linearity model for the kinetic energy loss into ionization energy of electrons and positrons, based on the empirical formula of Birks [123], was presented. As gammas deposit their energy in the form of secondary electrons in the detector, an algorithm was introduced to calculate the precise secondary electron spectrum of initial gammas. The algorithm was validated under the use of the JUNO simulation software, which uses the Geant4 software. It could be shown, that for the purpose of calculating the secondary electron spectrum, it offers large computational advantages to the Geant4 software. This algorithm was used here to convert the simple electron non-linearity model to the non-linearity model of gammas. To obtain the non-linearity of positrons, it was assumed, that each positrons annihilates at rest with an electron into two gammas after depositing its total kinetic energy as ionization energy. This assumption was tested against a comprehensive simulation under the use of the Geant4 software, which showed sub-percent differences in the light non-linearity for the considered Cherenkov light model and quenching constant $k_B = 0.01\,\mathrm{cm}^2/\mathrm{MeV}/\mathrm{g}$. Higher order effects, such as the in-flight annihilation electron-positron annihilation or the forming of ortho-positronium with its decay into three gammas should be included therefore in future studies to minimize the model uncertainty on the energy scale. Nevertheless, for the sensitivity studies of JUNO, the deviations are in a acceptable range to obtain a reasonable effect on the energy spectrum. As the gamma non-linearity and the positron non-linearity in this model share the same parameters, this model can be used to determine the positron non-linearity from the gamma calibration sources of the future calibration programme of JUNO. The results from this chapter are submitted as an article for publication and the pre-print of the article can be found at [151]. The source code of the algorithm for the calculation of the secondary electron spectrum is planned to be published online for free use [168].

Due to the dependence of the amount of detected light on the light emission vertex, a high uncertainty on this vertex introduces a large uncertainty on the detected amount of light, which directly affects the energy resolution in JUNO. As part of this thesis in Chapter 5, an analysis was presented, which estimates this light emission point to provide an appropriate correction for this light non-uniformity effect. It combines the informations from the PMT hit times and PMT hit charges in a likelihood estimation. To estimate the probabilities of the measured PMT hit times and PMT hit charges, the JUNO simulation software was used to create precise prediction maps of the detection volume under the use of the detector symmetries. It is shown, that the light emission vertex can be reconstructed especially precise in the regions of the detector, where the effect of the total reflection on the acrylic sphere occurs. As major effect for the gain in precision, the topology of the charge distribution on the PMT array was identified. In these regions the reconstruction reaches for positrons without kinetic energy a precision of about 6 cm, while outside these regions a precision of about 13 cm is reached. As the gradient of the light non-uniformity is especially large in such regions, it is shown that the reconstruction method from this thesis results in better results in a better energy resolution than the reconstruction presented in [139, 160] with a uniform resolution. With the displacement of the vertex of the neutron capture to the vertex of the positron signal from Inverse Beta Decay reactions, it was shown by the CHOOZ and the Double Chooz experiments, that it is possible to reconstruct the direction of an electron anti-neutrino flux [144, 161, 163]. It could be shown, that the reconstruction of the electron anti-neutrino flux direction is also possible in JUNO, although with larger uncertainties. For the vertex reconstruction performance in the detector center, a resolution of $(25.1 \pm 4.2)^\circ$ under the use of 5000 Inverse Beta Decay positron-neutron coincidences for a single source direction was estimated. The vertex reconstruction has potential to be further improved. Especially the smearing of the PMT hit times was done in an approximate way, as the measured properties of the PMT's and their readout electronics were not ready to be included in this thesis. Moreover, for high charge measurements of PMT hits, a smaller uncertainty is expected. An different, appropriate treatment of such high charge PMT hits was not implemented for this thesis, but could potentially improve the reconstruction. The charge information for the reconstruction in this thesis was calculated from a sum of all PMT hits for each PMT for each event. For the reconstruction with the charge information, the total summed charge for the entire event was used. The reconstruction can be further improved by using the time-dependent charge evolution on each PMT, instead of the summed total charge.

Another bias of the visible energy in JUNO stems from the large total rate of ^{14}C decays. These ^{14}C decays can timely coincide with signal events in the same readout window. The additional PMT hits cause a bias in the measured visible energy. In Chapter 6, two different ways of identifying these ^{14}C decays are presented, which can be used complementary. The first algorithm is a clusterization algorithm with the general purpose of identifying multiple energy depositions in a single readout window. This algorithm uses one threshold parameter to identify an energy deposition, another parameter to define its duration, and a sliding window with its length as a parameter to minimize statistical fluctuations. These parameters were optimized to find ^{14}C decays with a low misidentification of PMT dark counts, maximizing the sensitivity of a simple JUNO model to the Neutrino Mass Ordering. For this optimization, each event in which a ^{14}C decay was found, was rejected as a whole. For the nominal ^{14}C concentration of 10^{-17} ^{14}C atoms per ^{12}C atom, an improvement of the $\Delta\chi^2_{\mathrm{MO}}$ of 0.17 from $\Delta\chi^2_{\mathrm{MO}} = 10.83$ with no ^{14}C treatment to $\Delta\chi^2_{\mathrm{MO}} = 11.00$ with the optimized clusterization was

reached. Besides being able to be used to identify ^{14}C decays, the clusterization algorithm can be seen as a general tool to constrain the readout window to the signal region. This reduces the amount of dark counts in the PMT hit selection of other reconstruction algorithms and allows a separate reconstruction of different energy deposition. The presented clusterization algorithm works in a simple way without stringent assumptions on the signal shape. With such assumptions, the potential of the clusterization algorithm to separate different energy depositions in the same readout window might be improved. The presented version of the clusterization algorithm shows no efficiency for different energy depositions, which overlap in the PMT hit time distribution. To identify these events, the likelihood function of the presented vertex reconstruction was used. It could be shown, that 13.74% of these overlapping energy depositions could be identified as such, with a misidentification rate of 0.11%. Also this likelihood test shows potential to be improved with the aforementioned improvements of the vertex reconstruction. Under the use of this likelihood test, the sensitivity of JUNO to the Neutrino Mass Ordering can be further improved. This improvement needs to be evaluated and optimized in sensitivity studies under the use of a recent JUNO model.

It was shown, that the pile-up of PMT hits from IBD positrons and ^{14}C decay has a large impact on the sensitivity of JUNO to the Neutrino Mass Ordering, which should be addressed in future sensitivity studies. It is expected, that the JUNO experiment takes a crucial role in the global plans of the determination of the Neutrino Mass Ordering as currently the only planned and funded experiment, which aims to determine the Neutrino Mass Ordering with the use of vacuum oscillations. The prospects of many other experiments measuring either beam neutrinos [12, 13] or atmospheric neutrinos [14–17] aim to determine the Neutrino Mass Ordering with the measurement of the matter effects on neutrino oscillations. In the global analysis of neutrino oscillation parameters using past data in [62], the Inverted Neutrino Mass Ordering is excluded with a $\Delta\chi^2 = 10.4$, which hints towards the other possibility, the Normal Neutrino Mass Ordering. For this important measurement, crucial systematic uncertainties of the JUNO experiment are caused by the energy resolution and the uncertainty on the energy scale. The results from this thesis can be used by the JUNO experiment to reduce these systematic uncertainties.

Appendix A

JUNO Geant4 Simulation: Physics List

The JUNO Geant4 Simulation [18], which was used in this work, uses Geant4 in the version 9.4 [135, 136]. Due to the ongoing development in the JUNO collaboration, the used software does not represent the final simulation software used by the JUNO experiment. For the simulation of electromagentic processes, the following physics list was used:

Electron:

- G4eMultipleScattering
- G4LowEnergyIonisation
- G4LowEnergyBremsstrahlung

Gamma:

- G4LowEnergyRayleigh
- G4LowEnergyPhotoElectric
- G4LowEnergyCompton
- G4LowEnergyGammaConversion

Positron:

- G4eMultipleScattering
- G4eIonisation
- G4eBremsstrahlung
- G4PositroniumFormation

Appendix B

Secondary electron spectra for different generations

In Sec. 4.2.2, the algorithm for the calculating from the secondary electron spectrum from an initial gamma was validated with comparing it to the output from the Geant4 simulation from the JUNO software. Figure 4.5 shows the validation for the total secondary electron spectrum from 0.511 MeV gammas. In this chapter of the appendix, this validation is shown in greater detail for the different generations of secondary electrons. A generation of a secondary electron is defined by the order of generation by the initial gamma. The generations are shown, up to generation 24. On average, a gamma produces 17.107 ± 0.004 secondary electrons. Also here, the initial gamma has an energy of 0.511 MeV. One can clearly see, that the algorithm, which was implemented as part of this thesis yields results, which are very close to the results from the output from the JUNO Geant4 software. In the later generations, a second peak in the electron energy can be observed. This second peak is caused by the electrons, which are produced by the photoelectric absorption of the gammas.

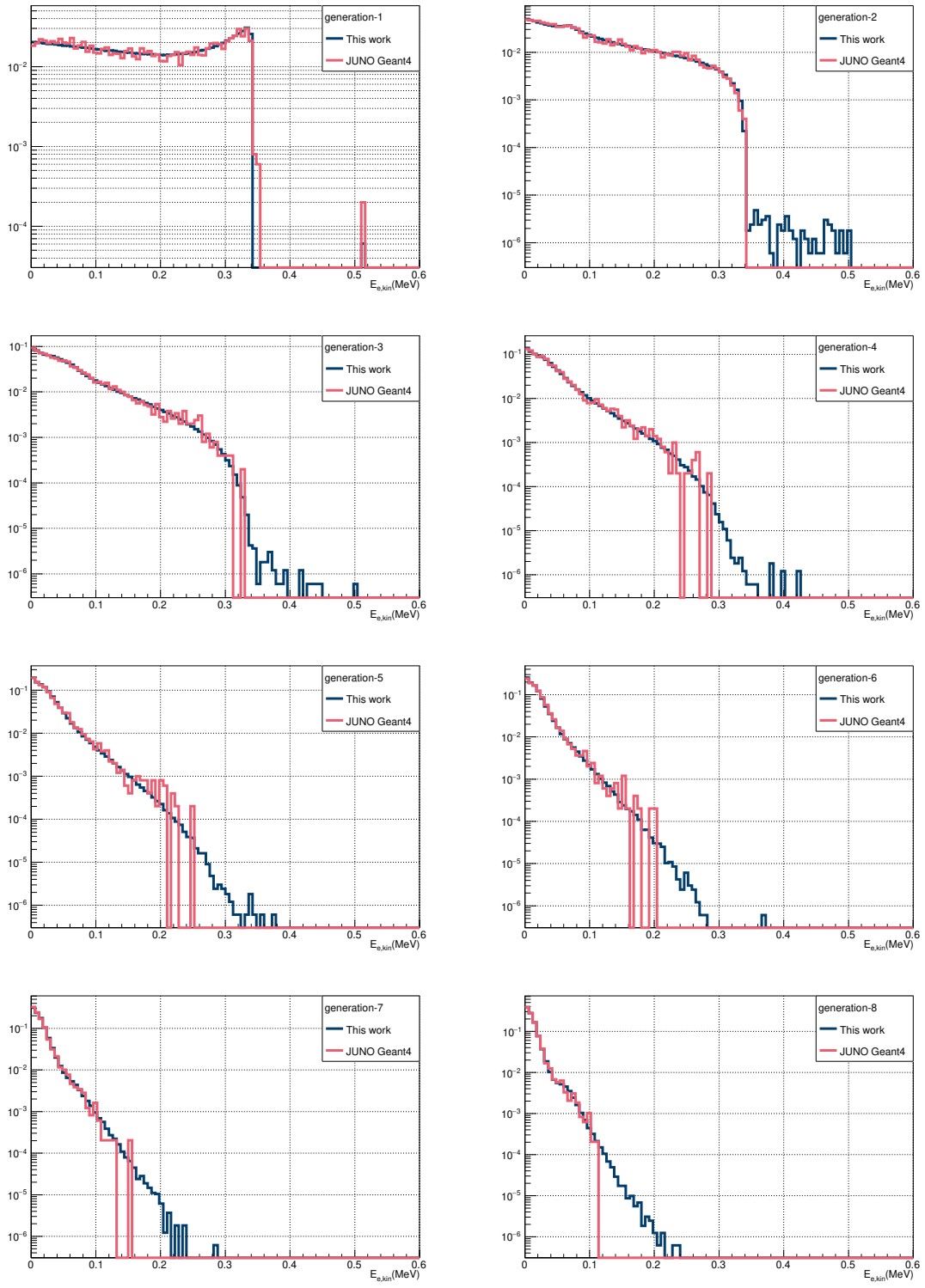

Figure B.1: Secondary electron spectrum seperated for different generations from generation 1 to generation 8.

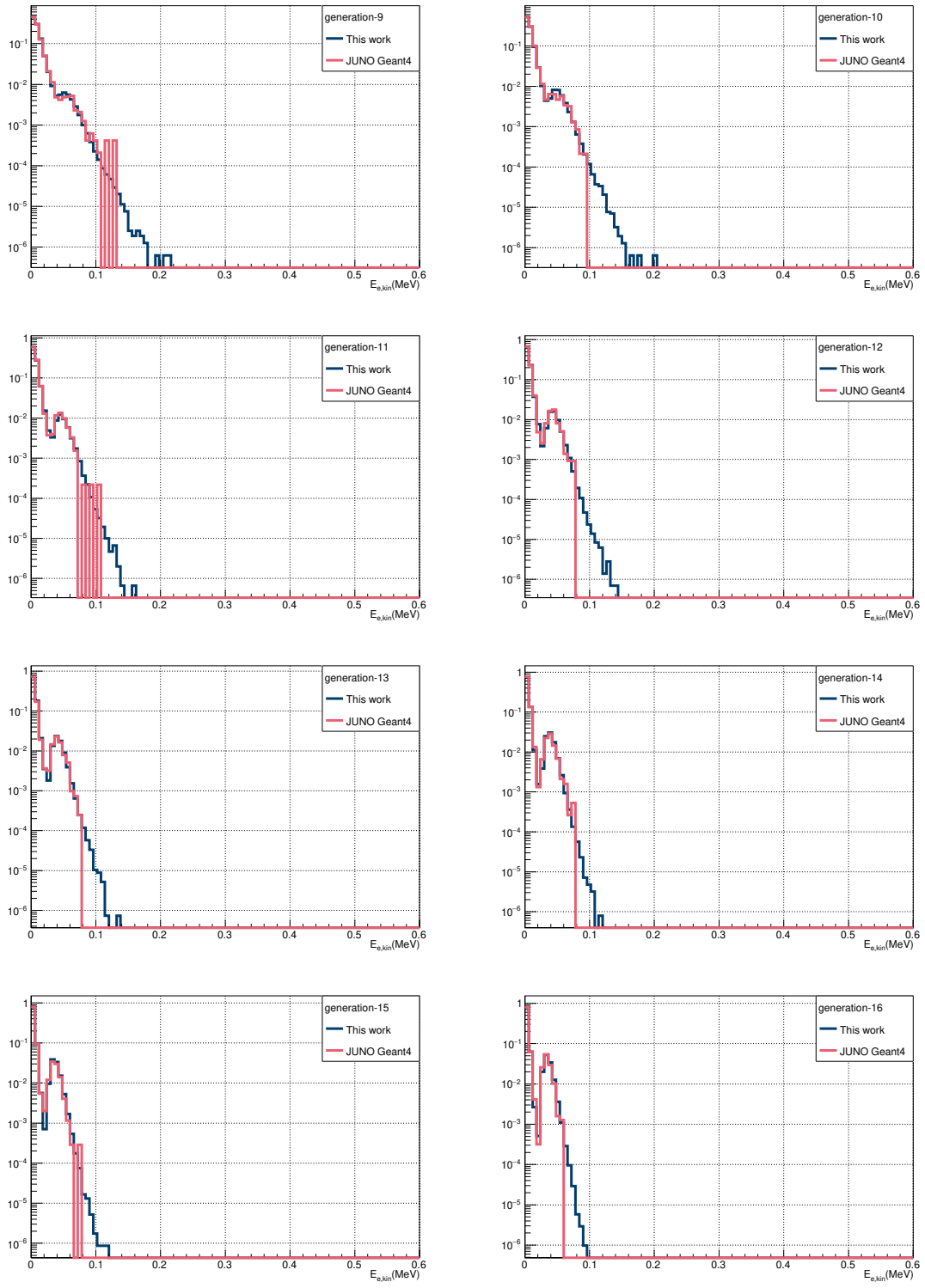

Figure B.2: Secondary electron spectrum seperated for different generations from generation 9 to generation 16.

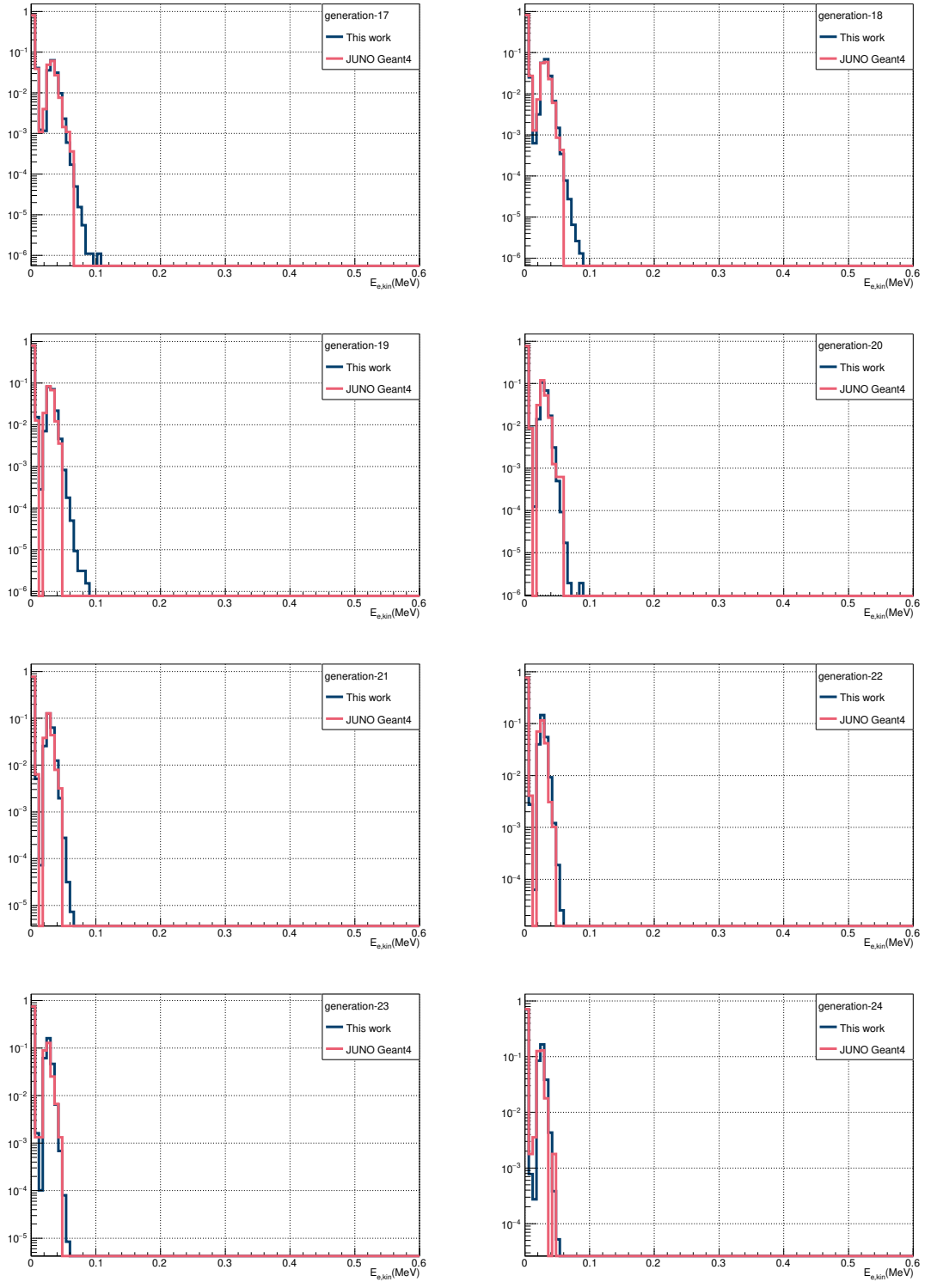

Figure B.3: Secondary electron spectrum seperated for different generations from generation 17 to generation 24.

Appendix C

Clusterization optimization scans

The clusterization parameters are optimized on the maximal sensitivity on the MO like shown in 6.1.4. For that, the MO sensitivity is evaluated on a grid of clusterization parameters. The trigger threshold parameter σ_T was varied from 3.0 to 7.0 with a step of 0.5, the baseline threshold parameter σ_B was varied from -1.5 to 1.3 with a step of 0.2, and the sliding window T_{win} was varied from 30 ns to 70 ns with a step of 10 ns. As only the evaluation of $T_{win} = 50\,ns$ was shown in Sec. 6.1.4, here all evaluations are shown.

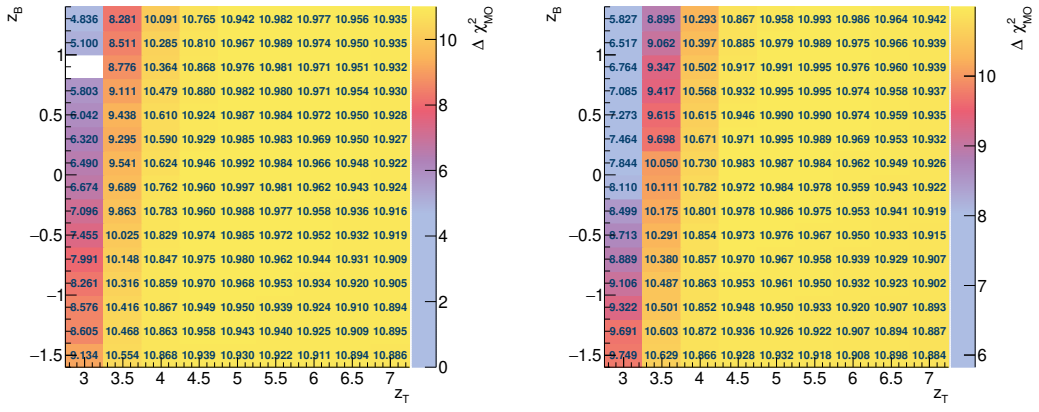

(a) Evaluation for $T_{\text{win}} = 30$ ns.

(b) Evaluation for $T_{\text{win}} = 40$ ns.

Figure C.1: Optimization scans for the clusterization parameters.

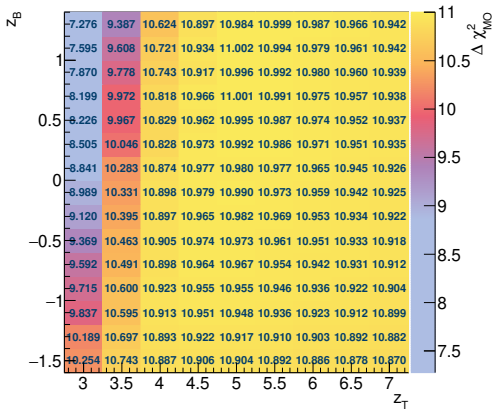

(a) Evaluation for $T_{\text{win}} = 50\,\text{ns}$.

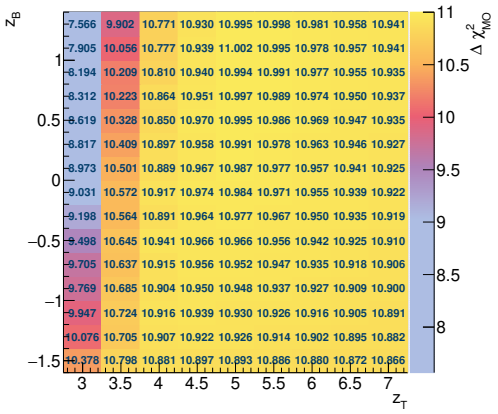

(b) Evaluation for $T_{\text{win}} = 60\,\text{ns}$.

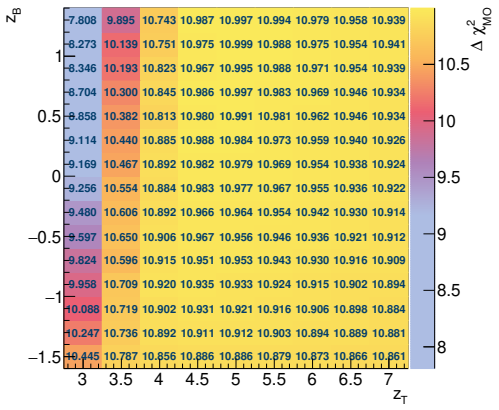

(c) Evaluation for $T_{\text{win}} = 70\,\text{ns}$.

Figure C.2: Optimization scans for the clusterization parameters.

List of Figures

List of Tables

Bibliography

[1] W. Pauli. *Offener Brief an die Gruppe der Radioaktiven.* Dec. 1930 (cited on pages 1, 7).

[2] C. L. Cowan et al. "Detection of the Free Neutrino: a Confirmation". In: *Science* 124.3212 (1956), pp. 103–104. DOI: 10.1126/science.124.3212.103 (cited on pages 1, 7, 12).

[3] Bruce T. Cleveland et al. "Measurement of the Solar Electron Neutrino Flux with the Homestake Chlorine Detector". In: *The Astrophysical Journal* 496.1 (Mar. 1998), pp. 505–526. DOI: 10.1086/305343 (cited on pages 1, 7).

[4] John N. Bahcall. "Solar models: An Historical overview". In: *AAPPS Bull.* 12.4 (2002). [Int. J. Mod. Phys.A18,3761(2003)], pp. 12–19. DOI: 10.1016/S0920-5632(03)01306-9 (cited on pages 1, 7).

[5] John N. Bahcall and Raymond Davis. "Solar Neutrinos: A Scientific Puzzle". In: *Science* 191.4224 (1976), pp. 264–267. DOI: 10.1126/science.191.4224.264 (cited on pages 1, 7).

[6] Samoil M. Bilenky. "Bruno Pontecorvo and Neutrino Oscillations". In: *Adv. High Energy Phys.* 2013 (2013), p. 873236. DOI: 10.1155/2013/873236 (cited on pages 1, 7).

[7] Q. R. Ahmad et al. "Measurement of the Rate of $\nu_e + d \rightarrow p + p + e^-$ Interactions Produced by ^8B Solar Neutrinos at the Sudbury Neutrino Observatory". In: *Phys. Rev. Lett.* 87 (7 July 2001), p. 071301. DOI: 10.1103/PhysRevLett.87.071301 (cited on pages 1, 7).

[8] Nick Jelley, Arthur B. McDonald, and R.G. Hamish Robertson. "The Sudbury Neutrino Observatory". In: *Annual Review of Nuclear and Particle Science* 59.1 (2009), pp. 431–465. DOI: 10.1146/annurev.nucl.55.090704.151550 (cited on pages 1, 7, 14).

[9] Y. Ashie et al. "Evidence for an Oscillatory Signature in Atmospheric Neutrino Oscillations". In: *Phys. Rev. Lett.* 93 (10 Sept. 2004), p. 101801. DOI: 10.1103/PhysRevLett.93.101801 (cited on pages 1, 7, 14).

[10] Nobel Foundation. *The Nobel Prize in Physics.* 2015. URL: https://www.nobelprize.org/prizes/physics/2015/ (cited on pages 1, 7).

[11] Fengpeng An et al. "Neutrino Physics with JUNO". In: *J. Phys.* G43.3 (2016), p. 030401. DOI: 10.1088/0954-3899/43/3/030401 (cited on pages 1, 18, 21, 23, 26, 32, 34, 36, 42, 43, 45, 46, 49, 53, 66, 69, 71, 106, 108, 110, 117).

[12] M. A. Acero et al. "First Measurement of Neutrino Oscillation Parameters using Neutrinos and Antineutrinos by NOvA". In: *Phys. Rev. Lett.* 123.15 (2019), p. 151803. DOI: 10.1103/PhysRevLett.123.151803 (cited on pages 1, 14, 17, 119).

[13] R. Acciarri et al. "Long-Baseline Neutrino Facility (LBNF) and Deep Underground Neutrino Experiment (DUNE)". In: (2015) (cited on pages 1, 17, 119).

[14] Shakeel Ahmed et al. "Physics Potential of the ICAL detector at the India-based Neutrino Observatory (INO)". In: *Pramana* 88.5 (2017), p. 79. DOI: 10.1007/s12043-017-1373-4 (cited on pages 1, 17, 119).

[15] M. G. Aartsen et al. "Letter of Intent: The Precision IceCube Next Generation Upgrade (PINGU)". In: (2014) (cited on pages 1, 17, 119).

[16] Veronique Van Elewyck. "ORCA: measuring the neutrino mass hierarchy with atmospheric neutrinos in the Mediterranean". In: *J. Phys. Conf. Ser.* 598.1 (2015), p. 012033. DOI: 10.1088/1742-6596/598/1/012033 (cited on pages 1, 17, 119).

[17] K. Abe et al. "A Long Baseline Neutrino Oscillation Experiment Using J-PARC Neutrino Beam and Hyper-Kamiokande". In: Dec. 2014 (cited on pages 1, 17, 119).

[18] J. H. Zou et al. "SNiPER: an offline software framework for non-collider physics experiments". In: *Journal of Physics: Conference Series* 664.7 (Dec. 2015), p. 072053. DOI: 10.1088/1742-6596/664/7/072053 (cited on pages 3, 40, 121).

[19] Tao Lin et al. "The Application of SNiPER to the JUNO Simulation". In: *Journal of Physics: Conference Series* 898 (Oct. 2017), p. 042029. DOI: 10.1088/1742-6596/898/4/042029 (cited on pages 3, 40).

[20] Anna Fatkina et al. "GNA: new framework for statistical data analysis". In: *23rd International Conference on Computing in High Energy and Nuclear Physics (CHEP 2018) Sofia, Bulgaria, July 9-13, 2018*. 2019 (cited on pages 3, 43, 104).

[21] *GNA home page*. URL: https://astronu.jinr.ru/wiki/index.php/GNA (visited on 10/28/2018) (cited on pages 3, 104).

[22] M. Tanabashi et al. "Review of Particle Physics". In: *Phys. Rev. D* 98 (3 Aug. 2018), p. 030001. DOI: 10.1103/PhysRevD.98.030001 (cited on pages 7, 8, 13, 32, 34, 43, 54, 55, 57).

[23] M. G. Aartsen et al. "Measurement of the multi-TeV neutrino interaction cross-section with IceCube using Earth absorption". In: *Nature* 551.7682 (2017), pp. 596–600. DOI: 10.1038/nature24459 (cited on page 7).

[24] M. Agostini et al. "Comprehensive measurement of pp-chain solar neutrinos". In: *Nature* 562.7728 (2018), pp. 505–510. DOI: 10.1038/s41586-018-0624-y (cited on pages 7, 25, 36).

[25] M. Agostini et al. "Comprehensive geoneutrino analysis with Borexino". In: *Phys. Rev.* D101.1 (2020), p. 012009. DOI: 10.1103/PhysRevD.101.012009 (cited on pages 7, 11, 47).

[26] Boris Kayser. "Neutrino Oscillation Physics". In: *Proceedings, 2011 European School of High-Energy Physics (ESHEP 2011): Cheile Gradistei, Romania, September 7-20, 2011*. [,1(2012)]. 2014, pp. 107–117. DOI: 10.5170/CERN-2014-003.107 (cited on page 9).

[27] Carlo Giunti. "Coherence and Wave Packets in Neutrino Oscillations". In: *Foundations of Physics Letters* 17.2 (2004), pp. 103–124. DOI: 10.1023/B:FOPL.0000019651.53280.31 (cited on page 10).

[28] E. Kh Akhmedov and A. Yu Smirnov. "Paradoxes of neutrino oscillations". In: *Physics of Atomic Nuclei* 72.8 (2009), pp. 1363–1381. DOI: 10.1134/S1063778809080122 (cited on page 10).

[29] Daya Bay Collaboration. "Study of the wave packet treatment of neutrino oscillation at Daya Bay". In: *The European Physical Journal C* 77.9 (2017), p. 606. DOI: 10.1140/epjc/s10052-017-4970-y (cited on page 10).

[30] Yat-Long Chan et al. "Wave-packet treatment of reactor neutrino oscillation experiments and its implications on determining the neutrino mass hierarchy". In: *Eur. Phys. J.* C76.6 (2016), p. 310. DOI: 10.1140/epjc/s10052-016-4143-4 (cited on page 10).

[31] L. Wolfenstein. "Neutrino Oscillations in Matter". In: *Phys. Rev. D* 17 (1978), pp. 2369–2374. DOI: 10.1103/PhysRevD.17.2369 (cited on page 10).

[32] S.P. Mikheyev and A.Yu. Smirnov. "Resonance Amplification of Oscillations in Matter and Spectroscopy of Solar Neutrinos". In: *Sov. J. Nucl. Phys.* 42 (1985), pp. 913–917 (cited on page 10).

[33] Brent Follin et al. "First Detection of the Acoustic Oscillation Phase Shift Expected from the Cosmic Neutrino Background". In: *Phys. Rev. Lett.* 115.9 (2015), p. 091301. DOI: 10.1103/PhysRevLett.115.091301 (cited on page 11).

[34] John N. Bahcall. "Solar models: An Historical overview". In: *AAPPS Bull.* 12.4 (2002). [Nucl. Phys. Proc. Suppl.118,77(2003); Int. J. Mod. Phys.A18,3761(2003)], pp. 12–19. DOI: 10.1016/S0920-5632(03)01306-9 (cited on page 11).

[35] Alain Bellerive. "Review of solar neutrino experiments". In: *Int. J. Mod. Phys.* A19 (2004), pp. 1167–1179. DOI: 10.1142/S0217751X04019093 (cited on page 11).

[36] Lawrence M. Krauss, Sheldon L. Glashow, and David N. Schramm. "Antineutrino astronomy and geophysics". In: *Nature* 310.5974 (1984), pp. 191–198. DOI: 10.1038/310191a0 (cited on page 11).

[37] H. A. Bethe. "Supernova mechanisms". In: *Rev. Mod. Phys.* 62 (4 Oct. 1990), pp. 801–866. DOI: 10.1103/RevModPhys.62.801 (cited on page 11).

[38] G. Pagliaroli et al. "Neutrinos from Supernovae as a Trigger for Gravitational Wave Search". In: *Phys. Rev. Lett.* 103 (3 July 2009), p. 031102. DOI: 10.1103/PhysRevLett.103.031102 (cited on page 11).

[39] Irene Tamborra et al. "High-resolution supernova neutrino spectra represented by a simple fit". In: *Phys. Rev.* D86 (2012), p. 125031. DOI: 10.1103/PhysRevD.86.125031 (cited on page 11).

[40] Pietro Antonioli et al. "SNEWS: The Supernova Early Warning System". In: *New J. Phys.* 6 (2004), p. 114. DOI: 10.1088/1367-2630/6/1/114 (cited on pages 12, 47).

[41] R.M. Bionta et al. "Observation of a Neutrino Burst in Coincidence with Supernova SN 1987a in the Large Magellanic Cloud". In: *Phys. Rev. Lett.* 58 (1987), p. 1494. DOI: 10.1103/PhysRevLett.58.1494 (cited on page 12).

[42] K. Hirata et al. "Observation of a Neutrino Burst from the Supernova SN 1987a". In: *Phys. Rev. Lett.* 58 (1987), pp. 1490–1493. DOI: 10.1103/PhysRevLett.58.1490 (cited on page 12).

[43] E.N. Alekseev et al. "Detection of the Neutrino Signal From SN1987A in the LMC Using the Inr Baksan Underground Scintillation Telescope". In: *Phys. Lett. B* 205 (1988), pp. 209–214. DOI: 10.1016/0370-2693(88)91651-6 (cited on page 12).

[44] John F. Beacom. "The Diffuse Supernova Neutrino Background". In: *Ann. Rev. Nucl. Part. Sci.* 60 (2010), pp. 439–462. DOI: 10.1146/annurev.nucl.010909.083331 (cited on page 12).

[45] Alankrita Priya and Cecilia Lunardini. "Diffuse neutrinos from luminous and dark supernovae: prospects for upcoming detectors at the $O(10)$ kt scale". In: *JCAP* 1711 (2017), p. 031. DOI: 10.1088/1475-7516/2017/11/031 (cited on page 12).

[46] M. Aker et al. "Improved Upper Limit on the Neutrino Mass from a Direct Kinematic Method by KATRIN". In: *Phys. Rev. Lett.* 123.22 (2019), p. 221802. DOI: 10.1103/PhysRevLett.123.221802 (cited on pages 12, 15).

[47] G. Bellini et al. "SOX: Short distance neutrino Oscillations with BoreXino". In: *JHEP* 08 (2013), p. 038. DOI: 10.1007/JHEP08(2013)038 (cited on page 12).

[48] Patrick Huber. "Determination of antineutrino spectra from nuclear reactors". In: *Phys. Rev. C* 84 (2 Aug. 2011), p. 024617. DOI: 10.1103/PhysRevC.84.024617 (cited on pages 12, 19, 104).

[49] Th. A. Mueller et al. "Improved predictions of reactor antineutrino spectra". In: *Phys. Rev. C* 83 (5 May 2011), p. 054615. DOI: 10.1103/PhysRevC.83.054615 (cited on pages 12, 19, 104).

[50] G. Mention et al. "The Reactor Antineutrino Anomaly". In: *Phys. Rev.* D83 (2011), p. 073006. DOI: 10.1103/PhysRevD.83.073006 (cited on pages 12, 19).

[51] Patrick Huber. "Reactor antineutrino fluxes - Status and challenges". In: *Nucl. Phys.* B908 (July 2016), pp. 268–278. DOI: 10.1016/j.nuclphysb.2016.04.012 (cited on pages 12, 19).

[52] Christian Buck et al. "Investigating the Spectral Anomaly with Different Reactor Antineutrino Experiments". In: *Phys. Lett.* B765 (2017), pp. 159–162. DOI: 10.1016/j.physletb.2016.11.062 (cited on pages 12, 19).

[53] J. H. Choi et al. "Observation of Energy and Baseline Dependent Reactor Antineutrino Disappearance in the RENO Experiment". In: *Phys. Rev. Lett.* 116.21 (2016), p. 211801. DOI: 10.1103/PhysRevLett.116.211801 (cited on page 12).

[54] Vedran Brdar, Patrick Huber, and Joachim Kopp. "Antineutrino monitoring of spent nuclear fuel". In: *Phys. Rev. Applied* 8.5 (2017), p. 054050. DOI: 10.1103/PhysRevApplied.8.054050 (cited on page 13).

[55] Ubaldo Dore, Pier Loverre, and Lucio Ludovici. "History of accelerator neutrino beams". In: *The European Physical Journal H* 44.4 (2019), pp. 271–305. DOI: 10.1140/epjh/e2019-90032-x (cited on page 13).

[56] Takaaki Kajita. "Atmospheric neutrinos and discovery of neutrino oscillations". In: *Proceedings of the Japan Academy. Series B, Physical and biological sciences* 86.4 (2010). JST.JSTAGE/pjab/86.303[PII], pp. 303–321. DOI: 10.2183/pjab.86.303 (cited on page 13).

[57] C. Rott, A. Taketa, and D. Bose. "Spectrometry of the Earth using Neutrino Oscillations". In: *Scientific Reports* 5.1 (2015), p. 15225. DOI: 10.1038/srep15225 (cited on page 13).

[58] R. Abbasi et al. "Measurement of the Anisotropy of Cosmic Ray Arrival Directions with IceCube". In: *Astrophys. J.* 718 (2010), p. L194. DOI: 10.1088/2041-8205/718/2/L194 (cited on page 13).

[59] M.G. Aartsen et al. "Evidence for High-Energy Extraterrestrial Neutrinos at the IceCube Detector". In: *Science* 342 (2013), p. 1242856. DOI: 10.1126/science.1242856 (cited on page 13).

[60] M. G. Aartsen et al. "Observation of High-Energy Astrophysical Neutrinos in Three Years of IceCube Data". In: *Phys. Rev. Lett.* 113 (2014), p. 101101. DOI: 10.1103/PhysRevLett.113.101101 (cited on page 13).

[61] S. Adrian-Martinez et al. "Letter of intent for KM3NeT 2.0". In: *J. Phys. G* 43.8 (2016), p. 084001. DOI: 10.1088/0954-3899/43/8/084001 (cited on page 13).

[62] Ivan Esteban et al. "Global analysis of three-flavour neutrino oscillations: synergies and tensions in the determination of th23, dCP, and the mass ordering". In: *Journal of High Energy Physics* 2019.1 (2019), p. 106. DOI: 10.1007/JHEP01(2019)106 (cited on pages 14, 15, 17, 18, 46, 119).

[63] S. Abe et al. "Precision Measurement of Neutrino Oscillation Parameters with KamLAND". In: *Phys. Rev. Lett.* 100 (2008), p. 221803. DOI: 10.1103/PhysRevLett.100.221803 (cited on pages 14, 25).

[64] K. Abe et al. "Measurements of neutrino oscillation in appearance and disappearance channels by the T2K experiment with 6.6×10^{20} protons on target". In: *Phys. Rev.* D91.7 (2015), p. 072010. DOI: 10.1103/PhysRevD.91.072010 (cited on page 14).

[65] P. Adamson et al. "Measurement of Neutrino and Antineutrino Oscillations Using Beam and Atmospheric Data in MINOS". In: *Phys. Rev. Lett.* 110.25 (2013), p. 251801. DOI: 10.1103/PhysRevLett.110.251801 (cited on page 14).

[66] P. Adamson et al. "Electron neutrino and antineutrino appearance in the full MINOS data sample". In: *Phys. Rev. Lett.* 110.17 (2013), p. 171801. DOI: 10.1103/PhysRevLett.110.171801 (cited on page 14).

[67] D. Adey et al. "Measurement of the Electron Antineutrino Oscillation with 1958 Days of Operation at Daya Bay". In: *Phys. Rev. Lett.* 121.24 (2018), p. 241805. DOI: 10.1103/PhysRevLett.121.241805 (cited on pages 15, 31, 35).

[68] Y. Abe et al. "Improved measurements of the neutrino mixing angle θ_{13} with the Double Chooz detector". In: *JHEP* 10 (2014). [Erratum: JHEP02,074(2015)], p. 086. DOI: 10.1007/JHEP02(2015)074,10.1007/JHEP10(2014)086 (cited on pages 15, 31, 35, 67).

[69] G. Bak et al. "Measurement of Reactor Antineutrino Oscillation Amplitude and Frequency at RENO". In: *Phys. Rev. Lett.* 121.20 (2018), p. 201801. DOI: 10.1103/PhysRevLett.121.201801 (cited on pages 15, 31, 35).

[70] Ch. Kraus et al. "Final results from phase II of the Mainz neutrino mass search in tritium beta decay". In: *Eur. Phys. J.* C40 (2005), pp. 447–468. DOI: 10.1140/epjc/s2005-02139-7 (cited on page 15).

[71] V. N. Aseev et al. "An upper limit on electron antineutrino mass from Troitsk experiment". In: *Phys. Rev.* D84 (2011), p. 112003. DOI: 10.1103/PhysRevD.84.112003 (cited on page 15).

[72] Ali Ashtari Esfahani et al. "Determining the neutrino mass with cyclotron radiation emission spectroscopy-Project 8". In: *J. Phys.* G44.5 (2017), p. 054004. DOI: 10.1088/1361-6471/aa5b4f (cited on page 15).

[73] A. Nucciotti et al. "Status of the HOLMES Experiment to Directly Measure the Neutrino Mass". In: *J. Low. Temp. Phys.* 193.5-6 (2018), pp. 1137–1145. DOI: 10.1007/s10909-018-2025-x (cited on page 15).

[74] Christian Weinheimer and Kai Zuber. "Neutrino Masses". In: *Annalen Phys.* 525.8-9 (2013), pp. 565–575. DOI: 10.1002/andp.201300063 (cited on page 15).

[75] A. Gando et al. "Search for Majorana Neutrinos near the Inverted Mass Hierarchy Region with KamLAND-Zen". In: *Phys. Rev. Lett.* 117.8 (2016). [Addendum: Phys.Rev.Lett. 117, 109903 (2016)], p. 082503. DOI: 10.1103/PhysRevLett.117.082503 (cited on page 15).

[76] P. A. R. Ade et al. "Planck 2015 results. XIII. Cosmological parameters". In: *Astron. Astrophys.* 594 (2016), A13. DOI: 10.1051/0004-6361/201525830 (cited on page 15).

[77] Michelle J. Dolinski, Alan W. P. Poon, and Werner Rodejohann. "Neutrinoless Double-Beta Decay: Status and Prospects". In: *Ann. Rev. Nucl. Part. Sci.* 69 (2019), pp. 219–251. DOI: 10.1146/annurev-nucl-101918-023407 (cited on page 16).

[78] Jun Cao et al. "Towards the meV limit of the effective neutrino mass in neutrinoless double-beta decays". In: *Chin. Phys.* C44.3 (2020), p. 031001. DOI: 10.1088/1674-1137/44/3/031001 (cited on page 16).

[79] Steven R. Elliott. "Double Beta Decay". In: *J. Phys. Conf. Ser.* 381 (2012), p. 012003. DOI: 10.1088/1742-6596/381/1/012003 (cited on page 16).

[80] F.P. An et al. "Observation of electron-antineutrino disappearance at Daya Bay". In: *Phys. Rev. Lett.* 108 (2012), p. 171803. DOI: 10.1103/PhysRevLett.108.171803 (cited on page 17).

[81] K. Abe et al. "Constraint on the matter–antimatter symmetry-violating phase in neutrino oscillations". In: *Nature* 580.7803 (Apr. 2020), pp. 339–344. DOI: 10.1038/s41586-020-2177-0 (cited on page 17).

[82] Boris Kayser and Gino Segre. "Leptogenesis at the Electroweak Scale". In: *Phys. Lett.* B704 (2011), pp. 570–573. DOI: 10.1016/j.physletb.2011.09.022 (cited on page 17).

[83] Soo-Bong Kim. "New results from RENO and prospects with RENO-50". In: *Nucl. Part. Phys. Proc.* 265-266 (2015), pp. 93–98. DOI: 10.1016/j.nuclphysbps.2015.06.024 (cited on page 18).

[84] P. Vogel and John F. Beacom. "Angular distribution of neutron inverse beta decay, anti-neutrino(e) + p —> e+ + n". In: *Phys. Rev. D* 60 (1999), p. 053003. DOI: 10.1103/PhysRevD.60.053003 (cited on pages 19, 37, 91, 93, 104).

[85] S. Schael et al. "Precision electroweak measurements on the Z resonance". In: *Phys. Rept.* 427 (2006), pp. 257–454. DOI: 10.1016/j.physrep.2005.12.006 (cited on page 19).

[86] Sebastian Böser et al. "Status of Light Sterile Neutrino Searches". In: *Prog. Part. Nucl. Phys.* 111 (2020), p. 103736. DOI: 10.1016/j.ppnp.2019.103736 (cited on pages 19, 20).

[87] Dmitry V. Naumov. "The Sterile Neutrino: A short introduction". In: *EPJ Web Conf.* 207 (2019), p. 04004. DOI: 10.1051/epjconf/201920704004 (cited on page 19).

[88] A. Aguilar-Arevalo et al. "Evidence for neutrino oscillations from the observation of $\bar{\nu}_e$ appearance in a $\bar{\nu}_\mu$ beam". In: *Phys. Rev.* D64 (2001), p. 112007. DOI: 10.1103/PhysRevD.64.112007 (cited on page 20).

[89] A. A. Aguilar-Arevalo et al. "Significant Excess of ElectronLike Events in the MiniBooNE Short-Baseline Neutrino Experiment". In: *Phys. Rev. Lett.* 121.22 (2018), p. 221801. DOI: 10.1103/PhysRevLett.121.221801 (cited on page 20).

[90] Carlo Giunti and Marco Laveder. "Statistical Significance of the Gallium Anomaly". In: *Phys. Rev.* C83 (2011), p. 065504. DOI: 10.1103/PhysRevC.83.065504 (cited on page 20).

[91] C. Giunti et al. "Update of Short-Baseline Electron Neutrino and Antineutrino Disappearance". In: *Phys. Rev.* D86 (2012), p. 113014. DOI: 10.1103/PhysRevD.86.113014 (cited on page 20).

[92] J. N. Abdurashitov et al. "Measurement of the solar neutrino capture rate with gallium metal. III: Results for the 2002–2007 data-taking period". In: *Phys. Rev.* C80 (2009), p. 015807. DOI: 10.1103/PhysRevC.80.015807 (cited on page 20).

[93] Philipp Kampmann. *Status and Physics of the JUNO experiment*. Aug. 2019. URL: https://yadi.sk/i/MaJPlzv8wTSp7w (visited on 04/05/2020) (cited on page 21).

[94] Cedric Cerna. "The Jiangmen Underground Neutrino Observatory (JUNO)". In: *Nuclear Instruments and Methods in Physics Research Section A: Accelerators, Spectrometers, Detectors and Associated Equipment* 958 (2020), p. 162183 (cited on page 21).

[95] Google. *Google maps*. May 2020. URL: https://www.google.de/maps/ (cited on page 22).

[96] World Nuclear Association (WNA). *Nuclear Power in China*. Mar. 2020. URL: http://www.world-nuclear.org/info/inf63.html (visited on 04/05/2020) (cited on pages 21, 22).

[97] Zelimir Djurcic et al. "JUNO Conceptual Design Report". In: (Aug. 2015) (cited on pages 22, 45).

[98] N. Agafonova et al. "Final results on neutrino oscillation parameters from the OPERA experiment in the CNGS beam". In: *Phys. Rev. D* 100.5 (2019), p. 051301. DOI: 10.1103/PhysRevD.100.051301 (cited on page 24).

[99] *JUNO internal wiki (password protected)*. URL: https://juno.ihep.ac.cn/mediawiki/index.php/Main_Page (visited on 04/20/2020) (cited on page 24).

[100] F.P. An et al. "The Detector System of The Daya Bay Reactor Neutrino Experiment". In: *Nucl. Instrum. Meth. A* 811 (2016), pp. 133–161. DOI: 10.1016/j.nima.2015.11.144 (cited on page 25).

[101] Joseph Lakowicz. *Principles of Fluorescence Spectroscopy*. Vol. 1. Jan. 2006 (cited on page 25).

[102] P. Lombardi et al. "Distillation and stripping pilot plants for the JUNO neutrino detector: Design, operations and reliability". In: *Nucl. Instrum. Meth. A* 925 (2019), pp. 6–17. DOI: 10.1016/j.nima.2019.01.071 (cited on page 25).

[103] G. Keefer et al. "Laboratory studies on the removal of radon-born lead from KamLAND's organic liquid scintillator". In: *Nucl. Instrum. Meth. A* 769 (2015), pp. 79–87. DOI: 10.1016/j.nima.2014.09.050 (cited on page 25).

[104] Paolo Lombardi et al. "Decay time and pulse shape discrimination of liquid scintillators based on novel solvents". In: *Nuclear Instruments and Methods in Physics Research Section A: Accelerators, Spectrometers, Detectors and Associated Equipment* 701 (2013), pp. 133–144. DOI: https://doi.org/10.1016/j.nima.2012.10.061 (cited on page 26).

[105] Gennady A. Kovaltsov, Alexander Mishev, and Ilya G. Usoskin. "A new model of cosmogenic production of radiocarbon 14C in the atmosphere". In: *Earth and Planetary Science Letters* 337-338 (2012), pp. 114–120. DOI: https://doi.org/10.1016/j.epsl.2012.05.036 (cited on page 26).

[106] Elisavet Georgiadou and Kristina Stenström. "Bomb-Pulse Dating of Human Material: Modeling the Influence of Diet". In: *Radiocarbon* 52.2 (2010), pp. 800–807. DOI: 10.1017/S0033822200045811 (cited on page 26).

[107] Francois Caron. "Life cycle and management of carbon-14 from nuclear power generation". In: *Progress in Nuclear Energy* 48 (Jan. 2006), pp. 2–36. DOI: 10.1016/j.pnucene.2005.04.002 (cited on page 26).

[108] H. GODWIN. "Half-life of Radiocarbon". In: *Nature* 195.4845 (Sept. 1962), pp. 984–984. DOI: 10.1038/195984a0 (cited on page 26).

[109] R. B. Firestone, L. P. Ekstrom, and S. Y. F. Chu. "WWW Table of Radioactive Isotopes". In: *APS Division of Nuclear Physics Meeting Abstracts*. APS Meeting Abstracts. Oct. 1999, CE.13 (cited on page 26).

[110] Hamamatsu Photonics K.K. *Photomultiplier tubes: Basics and applications*. 2007. URL: https://www.hamamatsu.com/resources/pdf/etd/PMT_handbook_v3aE.pdf (visited on 04/08/2020) (cited on page 27).

[111] Hamamatsu Photonics K.K. *Datasheet: LARGE PHOTOCATHODE AREA PHOTOMULTIPLIER TUBES*. 2019. URL: https://www.hamamatsu.com/resources/pdf/etd/LARGE_AREA_PMT_TPMH1376E.pdf (visited on 04/08/2020) (cited on page 28).

[112] Sen Qian. *The R&D, Mass Production of the 20 inch MCP-PMT for neutrino detector*. 2018. URL: https://rich2018.org/indico/event/1/contributions/16/contribution.pdf (visited on 04/08/2020) (cited on page 28).

[113] N. Anfimov. "Large photocathode 20-inch PMT testing methods for the JUNO experiment". In: *JINST* 12.06 (2017). Ed. by Lev Shekhtman, p. C06017. DOI: 10.1088/1748-0221/12/06/C06017 (cited on page 28).

[114] Haiqiong Zhang. "Performance in Mass Test of JUNO 20" PMTs". In: *International Conference on Topics in Astroparticle and Underground Physics*. 2019 (cited on pages 28, 29, 75, 78).

[115] Barbara Clerbaux. "The JUNO experiment and its electronics readout system". In: *Conference on High Energy Physics*. 2019 (cited on page 29).

[116] Miao He. "Double Calorimetry System in JUNO". In: *Proceedings of International Conference on Technology and Instrumentation in Particle Physics 2017 (TIPP2017), 2 vol.: Beijing, China, May 22-26, 2017*. 2017 (cited on page 29).

[117] HZC Photonics. *Datasheet: Photomultiplier Tubes*. 2017. URL: http://www.hzcphotonics.com/products/ProductManual.pdf (visited on 04/08/2020) (cited on page 29).

[118] Christoph Genster. "Software and hardware development for the next-generation liquid scintillator detectors JUNO and OSIRIS". PhD thesis. RWTH Aachen U., 2019. DOI: 10.18154/RWTH-2019-11430 (cited on page 30).

[119] D.A. Dwyer and T.J. Langford. "Spectral Structure of Electron Antineutrinos from Nuclear Reactors". In: *Phys. Rev. Lett.* 114.1 (2015), p. 012502. DOI: 10.1103/PhysRevLett.114.012502 (cited on page 31).

[120] Jun Cao. *Reactor neutrino anomalies*. Aug. 2019. URL: https://yadi.sk/i/VoK-Vte8Jpm-8g (visited on 05/13/2020) (cited on page 31).

[121] David V. Forero, Rebekah Hawkins, and Patrick Huber. "The benefits of a near detector for JUNO". In: (2017) (cited on page 31).

[122] JUNO collaboration. "TAO Conceptual Design Report". in preparation, preprint at arXiv:2005.08745. 2020 (cited on pages 31, 35).

[123] J. B. Birks. "Scintillations from Organic Crystals: Specific Fluorescence and Relative Response to Different Radiations". In: *Proc. Phys. Soc.* A64 (1951), pp. 874–877. DOI: 10.1088/0370-1298/64/10/303 (cited on pages 32, 53, 117).

[124] I. Frank and Ig. Tamm. "Coherent Visible Radiation of Fast Electrons Passing Through Matter". In: *Selected Papers*. Ed. by Boris M. Bolotovskii, Victor Ya. Frenkel, and Rudolf Peierls. Berlin, Heidelberg: Springer Berlin Heidelberg, 1991, pp. 29–35. DOI: 10.1007/978-3-642-74626-0_2 (cited on pages 33, 55).

[125] Wanda Beriguete et al. "Production of a gadolinium-loaded liquid scintillator for the Daya Bay reactor neutrino experiment". In: *Nuclear Instruments and Methods in Physics Research Section A: Accelerators, Spectrometers, Detectors and Associated Equipment* 763 (2014), pp. 82–88. DOI: https://doi.org/10.1016/j.nima.2014.05.119 (cited on pages 33, 55).

[126] Davide Franco, G. Consolati, and D. Trezzi. "Positronium signature in organic liquid scintillators for neutrino experiments". In: *Physical Review C* 83 (Nov. 2010). DOI: 10.1103/PhysRevC.83.015504 (cited on pages 33, 63).

[127] Ache Hans J. *Positronium and Muonium Chemistry*. Advances in Chemistry 175. Washington, DC: American Chemical Society, 1979 (cited on pages 33, 63).

[128] Y. Abe et al. "Ortho-positronium observation in the Double Chooz Experiment". In: *JHEP* 10 (2014), p. 032. DOI: 10.1007/JHEP10(2014)032 (cited on page 33).

[129] M.J. Berger et al. *XCOM: Photon Cross Sections Database*. https://www.nist.gov/pml/xcom-photon-cross-sections-database. Accessed: 2019-07-02. DOI: 10.18434/T48G6X (cited on pages 34, 58).

[130] J Kopecky. *Atlas of Neutron Capture Cross Sections (NGATLAS)*. Tech. rep. International Atomic Energy Agency, 1999 (cited on page 34).

[131] Juha Peltoniemi. *The Ultimate Neutrino Page*. 2003. URL: http://cupp.oulu.fi/neutrino/index.html (visited on 05/14/2020) (cited on pages 36, 37).

[132] Lianghong Wei et al. "Improving the Energy Resolution of the Reactor Antineutrino Energy Reconstruction with Positron Direction". In: (May 2020) (cited on page 36).

[133] Qingmin Zhang. "The JUNO calibration system". In: *39th International Conference on High Energy Physics*. 2018 (cited on pages 38, 39).

[134] D. Adey et al. "A high precision calibration of the nonlinear energy response at Daya Bay". In: *Nucl. Instrum. Meth. A* 940 (2019), pp. 230–242. DOI: 10.1016/j.nima.2019.06.031 (cited on pages 38, 39, 53, 66).

[135] S. Agostinelli et al. "Geant4 - a simulation toolkit". In: *Nuclear Instruments and Methods in Physics Research Section A: Accelerators, Spectrometers, Detectors and Associated Equipment* 506.3 (2003), pp. 250–303. DOI: https://doi.org/10.1016/S0168-9002(03)01368-8 (cited on pages 40, 41, 59, 100, 121).

[136] Geant4 collaboration. *Geant4: User Documentation*. https://geant4.web.cern.ch/support/. Accessed: 2020-05-12 (cited on pages 40, 59, 100, 121).

[137] Rene Brun and Fons Rademakers. "ROOT - An object oriented data analysis framework". In: *Nuclear Instruments and Methods in Physics Research Section A: Accelerators, Spectrometers, Detectors and Associated Equipment* 389.1 (1997). New Computing Techniques in Physics Research V, pp. 81–86. DOI: https://doi.org/10.1016/S0168-9002(97)00048-X (cited on pages 40, 55, 61, 78).

[138] H.Q. Zhang et al. "Comparison on PMT Waveform Reconstructions with JUNO Prototype". In: *JINST* 14.08 (2019), T08002. DOI: 10.1088/1748-0221/14/08/T08002 (cited on page 42).

[139] Qin Liu et al. "A vertex reconstruction algorithm in the central detector of JUNO". In: *JINST* 13.09 (2018), T09005. DOI: 10.1088/1748-0221/13/09/T09005 (cited on pages 42, 79, 80, 88, 89, 118).

[140] M.G. Aartsen et al. "Combined sensitivity to the neutrino mass ordering with JUNO, the IceCube Upgrade, and PINGU". In: *Phys. Rev. D* 101.3 (2020), p. 032006. DOI: 10.1103/PhysRevD.101.032006 (cited on page 44).

[141] Henning Rebber. "Event discrimination with Topological 3D Reconstruction at MeV Energies in the JUNO experiment". PhD thesis. Hamburg University, 2019 (cited on page 45).

[142] A. Gando et al. "Reactor On-Off Antineutrino Measurement with KamLAND". In: *Phys. Rev. D* 88.3 (2013), p. 033001. DOI: 10.1103/PhysRevD.88.033001 (cited on page 47).

[143] Ruohan Gao et al. "JULOC: A local 3-D high-resolution crustal model in South China for forecasting geoneutrino measurements at JUNO". In: *Physics of the Earth and Planetary Interiors* 299 (2020), p. 106409. DOI: https://doi.org/10.1016/j.pepi.2019.106409 (cited on page 47).

[144] Erica Caden. "Studying Neutrino Directionality with Double Chooz". In: (Aug. 2012) (cited on pages 47, 92, 118).

[145] Virginia Trimble. "Existence and Nature of Dark Matter in the Universe". In: *Ann. Rev. Astron. Astrophys.* 25 (1987), pp. 425–472. DOI: 10.1146/annurev.aa.25.090187.002233 (cited on page 48).

[146] K. Abe et al. "Search for proton decay via $p \to e^+\pi^0$ and $p \to \mu^+\pi^0$ in 0.31 megatonÂ·years exposure of the Super-Kamiokande water Cherenkov detector". In: *Phys. Rev. D* 95.1 (2017), p. 012004. DOI: 10.1103/PhysRevD.95.012004 (cited on page 48).

[147] C Aberle et al. "Light output of Double Chooz scintillators for low energy electrons". In: *Journal of Instrumentation* 6.11 (Nov. 2011), P11006–P11006. DOI: 10.1088/1748-0221/6/11/p11006 (cited on page 53).

[148] S. Yoshida et al. "Light output response of KamLAND liquid scintillator for protons and 12C nuclei". In: *Nuclear Instruments and Methods in Physics Research Section A: Accelerators, Spectrometers, Detectors and Associated Equipment* 622.3 (2010), pp. 574–582. DOI: https://doi.org/10.1016/j.nima.2010.07.087 (cited on page 53).

[149] B. von Krosigk et al. "Measurement of α-particle quenching in LAB based scintillator in independent small-scale experiments". In: *Eur. Phys. J. C* 76.3 (2016), p. 109. DOI: 10.1140/epjc/s10052-016-3959-2 (cited on page 53).

[150] Yaping Cheng. "GNA fitter and Detector response impact on MH sensitivity study". In: *XXVIII International Conference on Neutrino Physics and Astrophysics*. 2018 (cited on page 54).

[151] Philipp Kampmann, Yaping Cheng, and Livia Ludhova. "A semi-analytical energy response model for low-energy events in JUNO". In: (June 2020). arXiv:2006.03461 (cited on pages 54, 117).

[152] M.J. Berger et al. *Stopping-Power and Range Tables for Electrons, Protons, and Helium Ions*. https://physics.nist.gov/PhysRefData/Star/Text/method.html. Accessed: 2019-04-16. DOI: 10.18434/T4NC7P (cited on page 55).

[153] R. M. Sternheimer. "The Density Effect for the Ionization Loss in Various Materials". In: *Phys. Rev.* 88 (4 Nov. 1952), pp. 851–859. DOI: 10.1103/PhysRev.88.851 (cited on page 55).

[154] M. Agostini et al. "Simultaneous precision spectroscopy of *pp*, ^{7}Be, and *pep* solar neutrinos with Borexino Phase-II". In: *Phys. Rev. D* 100 (8 Oct. 2019), p. 082004. DOI: 10.1103/PhysRevD.100.082004 (cited on page 56).

[155] O. Klein and Y. Nishina. "Über die Streuung von Strahlung durch freie Elektronen nach der neuen relativistischen Quantendynamik von Dirac". In: *Zeitschrift für Physik* 52.11 (Nov. 1929), pp. 853–868. DOI: 10.1007/BF01366453 (cited on page 58).

[156] M. Agostini et al. "First Simultaneous Precision Spectroscopy of *pp*, ^{7}Be, and *pep* Solar Neutrinos with Borexino Phase-II". In: *Phys. Rev. D* 100.8 (2019), p. 082004. DOI: 10.1103/PhysRevD.100.082004 (cited on page 67).

[157] G Alimonti et al. "Light propagation in a large volume liquid scintillator". In: *Nuclear Instruments and Methods in Physics Research Section A: Accelerators, Spectrometers, Detectors and Associated Equipment* 440.2 (2000), pp. 360–371. DOI: https://doi.org/10.1016/S0168-9002(99)00961-4 (cited on page 71).

[158] Yan Zhang et al. "A complete optical model for liquid-scintillator detectors". In: *Nucl. Instrum. Meth. A* 967 (2020), p. 163860. DOI: 10.1016/j.nima.2020.163860 (cited on page 78).

[159] F. James and M. Roos. "Minuit: A System for Function Minimization and Analysis of the Parameter Errors and Correlations". In: *Comput. Phys. Commun.* 10 (1975), pp. 343–367. DOI: 10.1016/0010-4655(75)90039-9 (cited on page 78).

[160] Ziyuan Li et al. *Vertex Reconstruction and Deep Learning Applications in JUNO*. Aug. 2019. URL: https://pos.sissa.it/367/194/pdf (visited on 06/25/2020) (cited on pages 88, 89, 118).

[161] M. Apollonio et al. "Determination of neutrino incoming direction in the CHOOZ experiment and supernova explosion location by scintillator detectors". In: *Phys. Rev. D* 61 (2000), p. 012001. DOI: 10.1103/PhysRevD.61.012001 (cited on pages 92, 118).

[162] John F. Beacom and P. Vogel. "Can a supernova be located by its neutrinos?" In: *Phys. Rev. D* 60 (1999), p. 033007. DOI: 10.1103/PhysRevD.60.033007 (cited on page 92).

[163] Ya. Nikitenko. "Determination of the direction to a source of antineutrinos via inverse beta decay in Double Chooz". In: *Physics of Particles and Nuclei* 47.6 (Nov. 2016), pp. 1009–1013. DOI: 10.1134/S1063779616060186 (cited on pages 94, 118).

[164] Tino Ullrich and Zhu-An Xu. "Treatment of Errors in Efficiency Calculations". In: (May 2012) (cited on page 102).

[165] Glen Cowan et al. "Asymptotic formulae for likelihood-based tests of new physics". In: *Eur. Phys. J. C* 71 (2011). [Erratum: Eur.Phys.J.C 73, 2501 (2013)], p. 1554. DOI: 10.1140/epjc/s10052-011-1554-0 (cited on page 104).

[166] C. Patrignani et al. "Review of Particle Physics". In: *Chin. Phys. C* 40.10 (2016), p. 100001. DOI: 10.1088/1674-1137/40/10/100001 (cited on page 104).

[167] Konstantin Treskov. "The impact of the carbon-14 contamination in liquid scintillator on the sensitivity to the neutrino mass hierarchy determination in the JUNO experiment with Global Neutrino Analysis framework". In: *The XXI International Scientific Conference of Young Scientists and Specialists (AYSS-2017)*. 2017 (cited on page 106).

[168] *IKP-2 Neutrino Group*. URL: http://collaborations.fz-juelich.de/ikp/neutrino/ (visited on 07/17/2020) (cited on page 117).

Acknowledgements/Danksagung

Here, I would like to take the opportunity to thank all the people who accompanied me during the studies and the work on this thesis.
First of all, I would like to thank Livia Ludhova for giving me the opportunity to work on these topics and her supervision. She helped me a lot in my understanding of neutrino detectors and the topics of this thesis in many fruitful discussions. I am thankful for all the meetings, schools and conferences in many countries, which she made possible for me.
Moreover, I want to thank the neutrino group of IKP-2 and the LAND group of III. Physikalisches Institut B for the nice working atmosphere, counsel and ideas in many occasions. Special thanks goes here to my direct office neighbors and JUNO colleagues Christoph, Alexandre, and Michaela.
Thanks goes to many people, especially from the German group, of the JUNO collaboration. It was always fun to find good places for dinner and explore (mostly Chinese) cities. I want to thank Kostya, Maxim, and Dima for all the discussions and help on the GNA framework and on the non-linearity studies and Ziyuan Li and Guihong Huang for the numerous discussions about our reconstruction algorithms.
Finally, I want to thank my family. I thank my parents Anja and Joachim for their continuous support during my studies, Jingyi for being and invaluable source of motivation, support, and tasty lunch boxes, and Mia for always greeting me with a big smile when I came home from work.

*

An dieser Stelle möchte ich die Gelegenheit nutzen, allen Personen zu danken, die mich während der Studien und der Arbeit an dieser Doktorarbeit begleitet haben.
Zuerst möchte ich Livia Ludhova danken, dass sie mir die Möglichkeit gegeben hat, an diesen Themen zu arbeiten, und für ihre Betreuung. Sie hat mir in vielen fruchtbaren Diskussionen sehr geholfen, Neutrinodetektoren und die Themen dieser Arbeit zu verstehen. Ich bin dankbar für all die Treffen, Schulen und Konferenzen in vielen Ländern, die sie mir ermöglicht hat.
Darüber hinaus möchte ich der Neutrinogruppe des IKP-2 und der LAND-Gruppe des III. Physikalischen Institut B für die angenehme Arbeitsatmosphäre, Rat und Ideen bei vielen Gelegenheiten danken. Mein besonderer Dank gilt an dieser Stelle meinen direkten Büronachbarn und JUNO-Kollegen Christoph, Alexandre und Michaela.
Dank geht an viele Personen, insbesondere aus der deutschen Gruppe, der JUNO-Kollaboration. Es hat immer Spaß gemacht, gute Orte zum Abendessen zu finden und (meist chinesische) Städte zu erkunden. Ich möchte Kostya, Maxim und Dima für all die Diskussionen und Hilfe zum GNA-Framework und zu den Nichtlinearitätsstudien sowie Ziyuan Li und Guihong Huang für die zahlreichen Diskussionen über unsere Rekonstruktionsalgorithmen danken.
Abschließend möchte ich meiner Familie danken. Ich danke meinen Eltern Anja und Joachim für ihre kontinuierliche Unterstützung während meines Studiums, Jingyi dafür, dass sie eine unschätzbare Quelle der Motivation, Unterstützung und leckeren Lunchpakete war, und Mia dafür, dass sie mich immer mit einem breiten Lächeln begrüßt hat, wenn ich von der Arbeit nach Hause kam.

Eidesstattliche Erklärung

Ich, Philipp Renè Kampmann,

erkläre hiermit, dass diese Dissertation und die darin dargelegten Inhalte die eigenen sind und selbstständig, als Ergebnis der eigenen originären Forschung, generiert wurden.

Hiermit erkläre ich an Eides statt

1. Diese Arbeit wurde vollständig oder größtenteils in der Phase als Doktorand dieser Fakultät und Universität angefertigt;

2. Sofern irgendein Bestandteil dieser Dissertation zuvor für einen akademischen Abschluss oder eine andere Qualifikation an dieser oder einer anderen Institution verwendet wurde, wurde dies klar angezeigt;

3. Wenn immer andere eigene- oder Veröffentlichungen Dritter herangezogen wurden, wurden diese klar benannt;

4. Wenn aus anderen eigenen- oder Veröffentlichungen Dritter zitiert wurde, wurde stets die Quelle hierfür angegeben. Diese Dissertation ist vollständig meine eigene Arbeit, mit der Ausnahme solcher Zitate;

5. Alle wesentlichen Quellen von Unterstützung wurden benannt;

6. Wenn immer ein Teil dieser Dissertation auf der Zusammenarbeit mit anderen basiert, wurde von mir klar gekennzeichnet, was von anderen und was von mir selbst erarbeitet wurde;

7. Ein Teil dieser Arbeit wurde zuvor veröffentlicht und zwar in:
    - Philipp Kampmann, Yaping Cheng, and Livia Ludhova. “A semi-analytical energy response model for low-energy events in JUNO”, June 2020, https://arxiv.org/abs/2006.03461
        - Eingereicht zur Publikation in “Journal of Instrumentation”

Datum

Unterschrift